Hybrid Direct Write Lithographic Strategies for Complex Hierarchical Structures

by

Jonathan P. Singer

M.S. in Materials Science and Engineering

University of Pennsylvania (2008)

Submitted to the Department of Materials Science and Engineering in Partial Fulfillment of the

Requirements for the Degree of

Doctor of Philosophy in Materials Science and Engineering

at the

Massachusetts Institute of Technology

May, 2013

Signature of Author _____

Department of Materials Science and Engineering
May 2, 2013

Certified by _____

Edwin L. Thomas
Morris Cohen Professor of Materials Science and Engineering
Thesis Supervisor

Accepted by_____

Gerbrand Ceder
R. P. Simmons Professor of Materials Science and Engineering
Chair, Departmental Committee on Graduate Studies

Hybrid Direct Write Lithographic Strategies for Complex Hierarchical Structures

by

Jonathan P. Singer

Submitted to the Department of Materials Science Engineering on May 23, 2013 in Partial Fulfillment of the Requirements for the Degree of Doctor of Philosophy in Materials Science and Engineering

ABSTRACT

With the number of alternative lithographic techniques for high resolution and 3D patterning rapidly increasing, there is a need to identify a set of scalable techniques which balances the ability to arbitrarily control every detail of a target pattern and to produce these complex patterns at a high rate. It is in this way that metamaterial devices put forward on a lab scale for applications such as phononics, photonics, and plasmonics can be realized in the industrial scale.

This thesis, in approaching this challenge, utilizes combinations of patterning techniques, leveraging the ability for "large" scale alternative lithographic techniques, such as interference lithography or self-assembly, to create the same nanostructured morphology over a large area combined with laser direct write. The process of drawing a single line or isolated voxel can result in a hierarchical pattern defined by the latent motif of the larger-scale technique. The net result is to shift the burden of high resolution patterning from the direct write to the large scale technique, effectively decoupling the correlation between the level of detail and the patterning speed and control. More specifically, the following combinations with laser direct writing were investigated: (1) proximity field nanopatterning for the predefinition of diffraction-order-defined 3D resonators which were applied as "stand-up" plasmonic microresonators, (2) dewetting to conduct development-free 2D patterning of isolated sub-micron lines, and, via overlap effects, nanoscale (<100 nm) gratings, (3) block copolymer self-assembly to initiate the simultaneous annealing and alignment of near-equilibrium microdomains from a metastable starting morphology, and (4) interference lithography to fabricate 3D sub-micron periodic and quasiperiodic hierarchical structures with controllable positioning and tunable fill fraction that has potential for applications to microphotonics. In conjunction with the experimental components of technique development, multiphysics finite element method simulations are used to investigate the structuring mechanism, expected device behavior, and even inverse solutions to the complex problem of arriving at specific target structures. Each of these techniques, along with coupled simulations, represent highly promising first steps towards methods of rapidly generating on-demand hierarchical 2D and 3D structures.

Thesis Supervisor: Edwin L. Thomas

Title: Morris Cohen Professor of Materials Science and Engineering

Table of Contents

Table of Figures

Acknowledgements

I would like to begin by thanking my adviser, Professor Edwin Thomas. His resistance to "me too" research and his continuous desire to find new paradigms has forced me to stay creative and always look for clever ways to tackle a challenge. I would also like to thank the members of my Thesis Committee, Professors Jeffrey Grossman and Caroline Ross, for their support and constructive suggestions towards improving my research. This acknowledgement must also be extended to my previous mentors, Frederick Pinkerton (General Motors) and the late Professor Jack Fischer (University of Pennsylvania). As one of his last graduate advisees, I would like to dedicate this thesis to his memory in honor of his long career of mentorship.

A sizable portion of this research would not have been possible without the assistance of my collaborators, both in group and out. In particular I would like to acknowledge Jae-Hwang Lee of the Thomas Group (Chapter 2), Kevin Gotrik of the Ross Group (Chapter 4), David Veysset of the Keith Nelson Group (Chapter 7.3), and Pao-Tai Lin of the Lionel Kimerling Group (Chapter 3). I would also like to thank the undergraduates who contributed to this research: Mike Gibson, Ernesto Martinez, and particularly Tyler Hamer, as his software skills were immensely helpful in the implementation of the machine code necessary to take some of these results to their next level. Part of this research required the use of Brookhaven National Labs spectroscopy facilities, and I want to thank G. Larry Carr and his staff for their assistance in executing these measurements. Finally, I would like to acknowledge the assistance of the Institute of Soldier Nanotechnologies' research scientists, Steve Kooi and William DiNatale, who kept the bread-and-butter machines I needed daily in excellent shape. I am especially grateful to Steve for sharing his know-how, which was essential for all of the laser techniques developed here. I have learned almost everything I now know about optical setups from him.

Aside from the in-lab component, this work would not be possible without the support and patience of my family. For this particular chapter of my work, the biggest recognition is due to my wife, Christine Ezzell Singer, who capably dealt with the brunt of my anxious moments. I would also like to recognize

my parents, Steven Singer and Ruth Tal-Singer, and my grandmother, Dalia Tal, who have always been the foundation of my support network. In addition, the family dogs, Misty, Mojo, and the late Nami Singer, deserve credit as stress relievers. A special thanks is reserved for my friends, both old and new, for their assistance and support. Finally, I am continually grateful to the memory of my grandfather, Aaron Tal, who has always been an inspiration for both life and science.

Financial support for this thesis was provided by the Department of Defense through the NDSEG program, the Army Research Office through ISN, and the Defense Threat Reduction Agency.

1. Introduction

1.1. *Motivation and scope of work*

Before the start of this research, (i) electron-beam (e-beam) lithography had already demonstrated the ability to pattern sub-20 nm 2D features, (ii) block copolymers (BCPs) ordered by graphoepitaxy had been utilized for pattern transfer of 20 nm metallic wires, and (iii) the Eiffel Tower had been reproduced at a height of 50 μm by 3D direct write (DW). Clearly, if I were to have any impact on the lithographic field, I would have to identify either problems in the current techniques or new capabilities that had yet to be approached. It was in this way that I adopted the central philosophy around which this thesis is focused – finding methods to generate highly complex structures with a maximal degree of control in a scalable process by *combinations* of DW and large area techniques. The drive behind this is that there is a rapidly expanding family of theoretically studied metamaterials possessing extraordinary effective properties, including plasmonic resonators, photonic and phononic crystals, and pentamode and negative-Poisson mechanical structures. Further, many of the properties promised by these materials (*e.g.* cloaking, wave steering, ultralensing, 3D optical computing, etc.) will be the most beneficial if realized in either an assembly line or somehow macroscale fabrication method. Because of this, the highly accurate fabrication tools utilized in the aforementioned demonstrations may not possess the scalability to realize the large scale fabrication of some of the impressive lab-scale devices that have already been demonstrated. By sacrificing some of the specific structural control, it becomes possible to obtain a hierarchical patterning technique that can achieve pattern multiplication of a finer-scale globally defined pattern leading to orders of magnitude increase in overall patterning speed. It is with this in mind that I conducted my research, reported here.

The remainder of this section introduces background that will be useful to frame the discussion and cover the types of equipment utilized. The remaining chapters will each introduce a different combination/modification of patterning techniques. Chapter 2 will discuss a combination of nanoimprint

lithography and DW lithography for the single-shot production of complex microstructures, including an application to stand-up split ring resonators. Chapter 3 introduces laser spike annealing and applies it to 2D focused laser spike (FLaSk) DW dewetting of thin polymer films. Chapter 4 continues 2D FLaSk of thin films and incorporates local simultaneous ordering and alignment of a metastable BCP thin film by focused laser induced cold zone annealing. Chapter 5 extends the FLaSk laser heating methodology into 3D by utilizing dye-doped polymer absorption as a heating source to initiate annealing of a prepatterned photoresist film. In this way, hierarchical micro/nanostructures are generated by a combination of interference lithography (IL) and DW lithography. Chapter 6 highlights the thesis and suggests further directions for future research on the introduced techniques. These chapters are followed by several appendixes detailing affiliated methods developed during the course of the research and will be concluded with a list of references.

1.2. *Fabrication techniques*

1.2.1. **2D Fabrication**

Conventional photopatterning processes involve the application of light to a photoactive material, either through projection of a mask pattern or through exposure by a rastering UV DW. The greatest potential for high resolution patterning comes from charged particle e- (or more recently, helium ion)[1] beam lithography. Both of these techniques (and in fact all DW techniques) face the inherent limitation of being serial processes and thus will have to overcome significant hurdles with respect to write speeds. Much like conventional DW, e-beam lithography is conducted using the focused beam of electrons to activate the crosslinking or degradation of a solid resist. E-beam, however, is currently the state of the art in terms of resolution of controllable structures, with patterning capability down to sub-10 nm features[2] and typical feature sizes in the sub-50 nm range. Furthermore, by supplying a stream of precursor gas near the electron beam, the e-beam may also be used to deposit metals, ceramics, or semiconductors on a similarly small scale[3-5] or even to induce the precipitation and growth of metallic nanoparticles out of a

metal-ion-containing resist (or any appropriate polymer) layer.[6, 7] For these reasons, e-beam is an extremely attractive tool for current and future high resolution lithographic applications; however, due to the high scattering of electrons in all media,[8] e-beam lithography faces limitations with respect to aspect ratios of structures and cannot practically be extended to 3D (though 2.5 D structures have been demonstrated[9] and materials deposition can be used to slowly build up interconnected 3D structures).[5]

1.2.2. **Layer-by-layer fabrication techniques**

Micro and nanoscale metamaterials require a different set of process capabilities to design many of the features necessary for 3D devices. It is possible to accomplish fabrication of 3D structures by the layer-by-layer stacking of multiple 2D structures.[10-13] These fabrication methods have been performed in the past for photonic devices. The layer-by-layer techniques can be divided into two approaches: subtractive and additive. In the subtractive approach, each 2D structure is defined by etching, for example, a 3D periodic silicon structure that has been produced by the iteration of 2D structural patterning sequences consisting of silicon deposition, masking, etching, sacrificial material deposition, and chemical-mechanical planarization (see Figure 1-1 a and b).[11, 12] In spite of superior structural fidelity, the multiple steps make this approach costly and time-consuming.

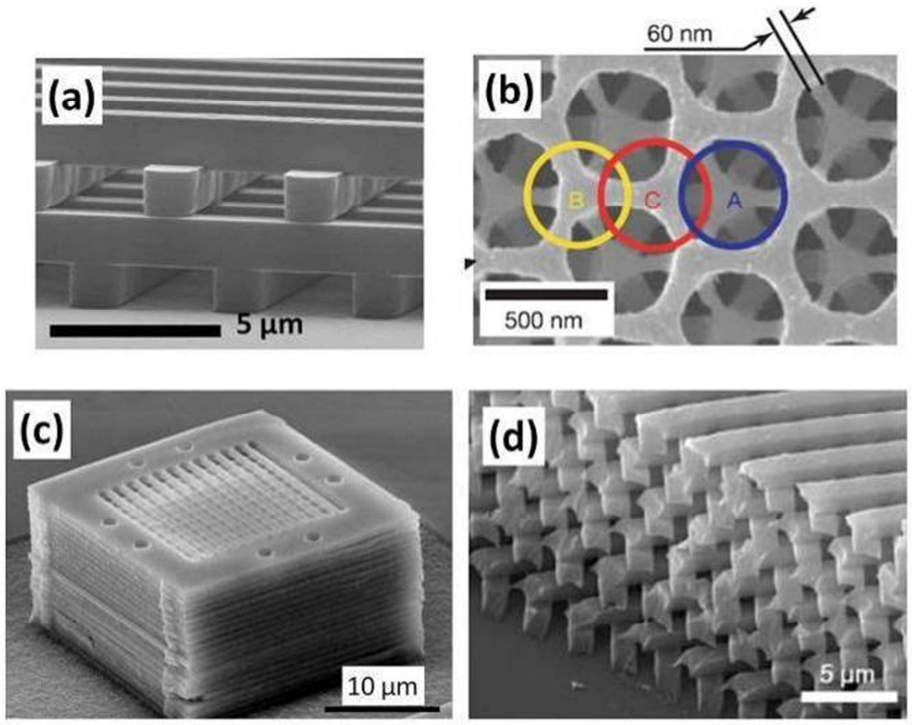

Figure 1-1: Layer-by-layer fabrication. (a),(b) Silicon photonic crystals by conventional photolithography.[11, 12] (c) Photonic crystal by stacking of 2D indium phosphide plates.[14] (d) Polymer structure by soft lithography.[13]

In contrast, in the additive approach, a pre-patterned 2D structure is simply added on top of the other 2D structure. Thereby, etching and related processes, sacrificial material deposition, and planarization can be eliminated. For example, 3D structures have been made by stacking multiple grating structures using micromanipulation.[14] In this study (Figure 1-1c), simple 2D semiconductor processing was used to make individual 2D semiconductor structures that were positioned using a micromanipulator in stacks of the desired functionality. Since the free-standing 2D structure is simply a patterned thin membrane, this approach may be difficult to apply for a wide area 3D structure due to the mechanical instability. A full-additive approach without any etching process utilizing soft lithography technique was done by layer-by-layer transfer of polymer structures carried by an elastomeric substrate (Figure 1-1d).[10, 13] The soft lithographic techniques are attractive for wide sample size, low cost, and high structural fidelity.[15]

All the layer-by-layer techniques, however, have significant limitations on aspects such as features that cross multiple levels, the ability to have multiple material types in close proximity at the same height, and loss of resolution/precision due to registry and layer-to-layer mechanical integrity and stability considerations. As research into conventional lithography alternatives progresses, the variety of techniques for creating complex 3D assemblies is ever increasing, along with the variety of possible target structures and the degrees of available tunability of both the patterning process and the patterned structures.

1.2.3. **Angle exposure techniques**

Though not a particular topic of this research, one of the more successful strategies for the generation of 3D structures involves the application of conventional top down techniques with the added feature of the use of multiple angles. Among the earliest of these techniques is glancing angle deposition,[16-19] in which a seeded or bare substrate is exposed to an evaporated source at an angle near 90°. By adjusting the rotation of the substrate with respect to the source, the direction of growth can be controlled. Initially, this was restricted to angling of grains in thin films. More recently, it has been expanded to generation of high aspect ratio helices with nanoscale diameters and pitches.[17, 18]

Another set of angled techniques features exposure through a 2D physical mask. In angled etching,[20-22] a metallic mask patterned by conventional 2D lithographic techniques is utilized as a barrier for a reactive ion etch. In this way angled holes can be directed through a semiconductor to form a 3D pattern potentially containing line defects.[20] An analogous soft lithographic technique that has been applied to mechanical metamaterials is self-propagating polymer waveguides.[23-25] Here, a physical mask is placed on top of a liquid polymer photoresist which is exposed to angled collimated UV light. The resist is selected to exhibit a significant increase in index upon crosslinking such that the propagation of the exposing light is waveguided through the resist, including through intersections (or nodes) of two waveguided beams. The net result is the highly robust fabrication of 3D polymeric truss structures down

to the micron scale which can be used as templates for generation of elastomeric or metallic filled or hollow structures by coating or double inversion.[23-25]

1.2.4. **Interference lithography**

The phenomenon behind IL is the formation of non-uniform intensity fields by the interference of two or more light sources of different directions, polarizations, amplitudes, and/or phases. At the zone of coincidence of the sources, the interference patterns will be periodic or quasiperiodic with periodicity determined by the above parameters along with the wavelength(s) of the sources. By locating the resulting inteferogram of properly tuned light sources inside of a photoresist, the interference pattern can be converted into a 1D, 2D, or 3D structure by a change in chemical functionality, (de)crosslinking, or (de)polymerization reaction of the negative(positive) tone photoresist. The two general strategies to accomplish IL are multi-beam and phase mask interference.

In multi-beam IL (MBIL),[26] patterns are generated by the interference of multiple beams of selected intensity, polarization, angle of incidence, and phase, usually generated by a splitting and then recombination of a coherent source such that the consideration of phase may be controlled purely by the path lengths of the multiple beams (Figure 1-2a). The greatest attraction of this approach is that it has a solvable inverse problem; with a target structure in mind, it is possible to determine the necessary beam parameters to achieve a structure approaching the target by solving a Fourier expansion of the desired intensity distribution.[27] The more terms (plane-wave sources) included in the expansion, the more accurately the target structure will be described. For the most basic structures, each source provides an additional degree of dimensionality (two beams can be used to pattern 1D gratings, three beams can be used to pattern 2D lattices, etc.). Moreover, additional beams may also be employed to give degrees of freedom such as allowing for different symmetries or tuning of various structural parameters. In this way, MBIL has been utilized to fabricate phononic,[28, 29] and mechanical structures,[30] as well as photonic structures.[31, 32] The advantage of control provided by MBIL is at the same time its biggest drawback – the

fact that every intensity distribution corresponds to a specific (non-unique) set of beam parameters means that any given MBIL pattern must have a well aligned set of optics and further is practically limited in accuracy by the number of beams that can be accurately brought to a sample as well as the loss in contrast between the high and low intensity points with number of beams (the number of beams is generally not higher than 6). In order to utilize the same setup to make a different structure, all of these optics must be changed. This is not the case with phase mask IL.

Phase mask IL (PMIL) is a much simpler technique than MBIL. In this approach, a phase mask is brought into contact,[33] imprinted into,[34, 35] or deposited on via self-assembly[36] with a solid photoresist (Figure 1-2b). The mask, a 1D or 2D pattern (possibly in multiple layers)[37] is then used to produce multiple diffracted beams from a single incident beam, which themselves in turn produce an interference pattern within the resist. Thus, the phase mask (and generating master) are the only required optics – though practically there are some considerations for the light source – for generating complex, large area 3D patterns, and have been used for the generation of structured particles[38] and photonic crystal templates.[39, 40] The drawback of this technique, however, is the opposite of that of MBIL. While simpler, the inverse problem of PMIL currently does not have an available analytic solution and thus phase masks must be designed via educated guesses motivated by symmetry and subsequent simulation. A more systematic approach to this process is simulation-based structural fitting,[41] wherein a target structure is compared to past results and the phase masks belonging to close matches are altered parametrically to arrive at an optimal fit within the space of the selected mask features. Further, results from the parametric sweep are broken down to Fourier series fits to further populate the database.

Overall, MBIL is advantageous in the capabilities of non-contact exposure and a wider range of possible structures while PMIL is valuable for its simpler optics and resistance to environmental perturbation like mechanical vibration. Regardless of which technique is used, IL faces limitations in the resolution and 3D capability of the resulting structures. In terms of resolution, IL is optically limited and further limited by the sensitivity of resists employed. While these are both rather small scale limits (EUV

IL has been demonstrated down to 11 nm),[42] use of EUV or X-ray lithographic sources demands very expensive optics and facilities. For 3D structures, resolution and potential scale are limited by the absorption of the photoresists and phase masks. Sample adsorption can be reduced by utilizing multiple instead of single photon excitation,[34] as the cross-section for multiple photon absorption is usually lower than single, a larger fraction of the excitation source will penetrate into the sample allowing for deeper patterning at the cost of larger feature size, though contrast will be increased. Use of multiphoton IL is generally only possible in PMIL due to the coherence requirement being difficult to accomplish with a short pulse. More specifically, 150 fs pulse corresponds to 45 μm in free space, meaning that only path length differences on the order of 10 μm would be acceptable for MBIL.

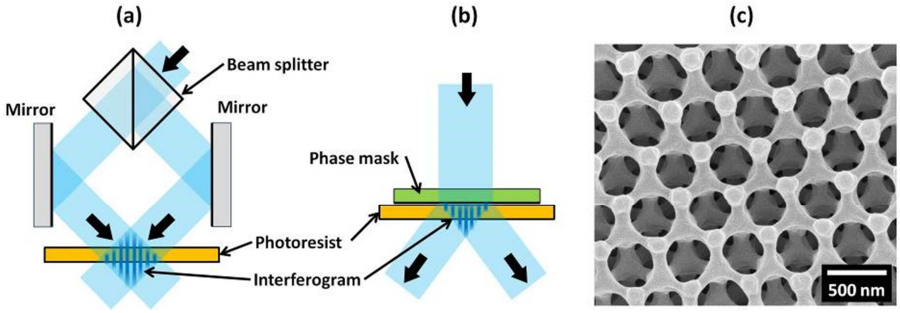

Figure 1-2: Schematic of (a) MBIL and (b) PMIL. For simplicity only two beams are illustrated. (c) SEM image of a SU-8 photoresist structure fabricated by 4-beam MBIL.[43]

1.2.5. Direct write lithography

DW lithography is the most intuitive form of lithography and provides the greatest degree of arbitrary control since patterns are not restricted to a specific periodicity or characteristic length scale. There are three general categories for DW techniques: nozzle printing, charged particle, and optical. All three of these techniques face the inherent limitation of being serial processes, and thus will have to overcome significant hurdles in terms of write speeds. One possible strategy to overcome this is to employ parallel systems consisting of multiple serial writers.

Nozzle-based printing techniques are a versatile method for the rapid production of 3D structures that can be decomposed into vector maps. The most common example of such a technique is commercially available 3D printing tools. These tools use molten polymers or UV-curable polymers to write features on the sub-mm scale. Recently, a variation of this technique using functional sol-gel inks has been developed.[44-48] By utilizing shear thinning colloidal inks, structures of various materials, including polymers,[46] metals,[47] and semiconductors,[48] can be rapidly patterned down to the micron scale. This technique has been applied to structures ranging from photonic woodpiles[45] to vascular networks.[49]

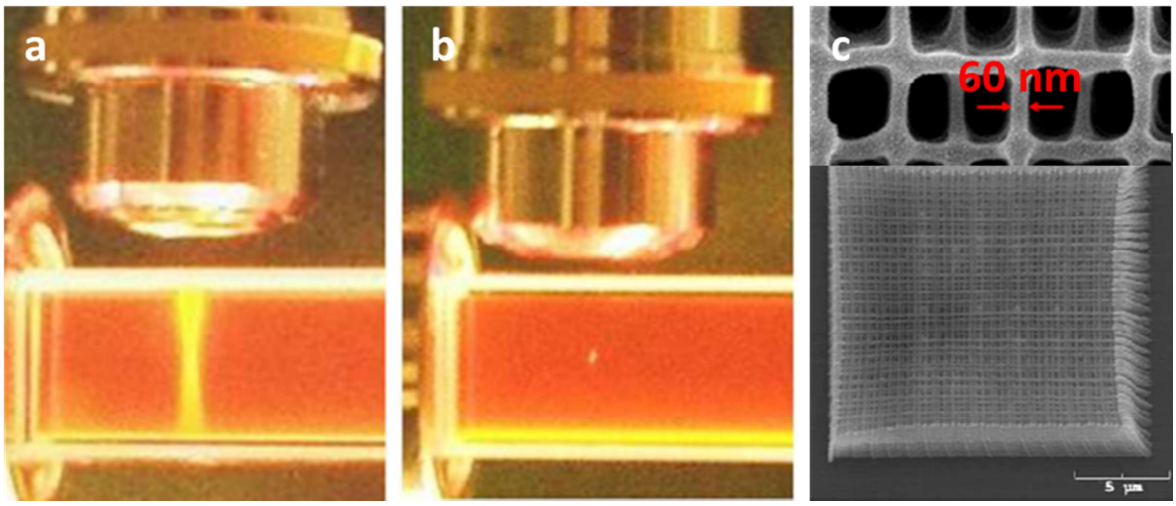

Figure 1-3: (a,b) Illustration by dye fluorescence of difference between single (a) and multiple (b) photon excitation. Smaller excitation voxel size occurs for multiphoton lithography (MPL) due to necessity for high intensity that is only satisfied at the focal point.[50] (c) Example of 65 nm feature size woodpile generated through multiphoton excitation from green light. [51]

A variation on nozzle-based 3D printing is layer-by-layer 3D printing. In this technique, the patterned media is introduced one layer at a time from the bottom up and progressively patterned. This has been accomplished both with granular media using a glue nozzle and also optically with a "light nozzle" or galvan-omirror-steered laser in a highly absorbing liquid photoresists. One specific implementation of the latter technique, called microprojection stereolithography,[52] allows for nearly arbitrary fabrication with micron scale resolution by slowly sinking the patterned structure in a resist bath and exposing the newly formed surface layer of resist to 2D UV light patterns controlled by a digital

mirror array. The exposure light can only penetrate a small depth into the resist, thus defining the rate at which the structure can change. This technique has been utilized to design mechanically actuatable structures by patterning of a hydrogel resist.[53]

For 2.5-3D sub-micron structures, optical DW (3DDW) by a focused laser beam is also a very popular fabrication method. In these techniques, nearly arbitrary patterns are "written" in a photoactive media by the patterning laser via either controlled motion of the relative position of the sample and lens or by deflection within the field of view by galvano-mirrors. While the earliest demonstrations utilized single photon absorption at the edges of the absorption band,[54] MPL[50, 55-59] or other non-linear effects[60-62] have become the standard methods for rapid patterning of nearly arbitrary 3D structures. MPL (Figure 1-3) is performed by the activation of a photoinitiated process by simultaneous (on the timescale of the excitation) multiple adsorptions of light below the absorption edge of the initiator. Most typically this is a UV excitation driven by double adsorption of visible or NIR light, but three photon MPL has been demonstrated.[56]

The capability for MPL 3DDW arises from this multiple adsorption process – the rate of a photoinitiated process will scale as the intensity to the power of the number of simultaneous adsorptions required,[50] thus increasing the resolution of the technique. MPL of photoresins currently has been primarily used for photonics[57] and plasmonics.[63] Recently it has been applied to mechanical metamaterials for fabrication of 3D auxetic [64] and pentamode structures.[65] A large variety of materials systems have been employed in MPL. One of the most common are radically polymerized systems.[51, 57, 66, 67] In these systems, the translating point causes the generation of free radicals by an initiator, these in turn polymerize the surrounding resist. Radical resists are generally restricted to MPL because they are usually liquid (consisting of monomers) and thus often do not form stable films for conventional or IL techniques; however, as a consequence they possess the unique feature of easily generating arbitrarily thick samples as they can be drop cast. The other major family of MPL resist systems is polymeric or oligomeric solid chemically amplified resists (CARs).[60, 68, 69] These systems are more analogous to (and in

fact often are) conventional lithography resists and consist of systems which crosslink (negative tone) or degrade (positive tone) upon excitation of the photoinitiator, often with some additional baking step to speed the process.

A unique process to MPL is the direct photoreduction of a dispersed metallic salt into metal features, either out of solution[70] or from a polymer matrix.[7, 71-73] The photoreduction occurs between the metal ions and some sacrificial reducing agent in the surrounding medium. As opposed to initiation of a radical or crosslinking agent, the energy for photoreduction goes directly into the reaction, meaning that the resulting metal comes in the form of many individual nuclei or nanoparticles. The size and number density of these depends both on the mobility of the ion in the medium and also the local concentration. No matter how high these may be, the final structure is an agglomeration of individual particles and thus often faces issues in connectivity and mechanical stability (though agents such as surfactants in solution have been employed to increase the density of these aggregates).[70] The low connectivity in turn has been shown to deliver poor conductivity, roughly three orders of magnitude below bulk conductivity.[71] The best results approaching the bulk conductivity have been obtained from deposition from high-diffusivity, surfactant assisted solution.[74] As a result, other approaches to obtaining metallic MPL structures, such as coating of functionalized resist[75] or electroplating[76] have been utilized; however, a key advantage of metallic DW that is not possessed by any other lithographic technique (aside from the field of 3D holographic or multilayer memory where small binary contrast is sufficient) is the ability for contrast from unsupported or interconnected structures. While the applications of 3D metal writing have been restricted to optical[70, 77, 78] or electronic structures,[79] the potential of patterning arbitrary high density metallic structures within a soft matrix could be exceedingly useful for the development of mechanical architectures, such as negative modulus structures.

Resolution of MPL is limited by optical considerations. For typical high numerical aperture systems (immersion NA=~1.4), the optical limit is around $\lambda/2$. Even so, feature sizes of $\lambda/4$-$\lambda/8$ are regularly achieved in MPL DW. This is generally due to chemical effects in addition to the usual effects of

development. One example is the quenching of radical activated processes naturally by oxygen present in the resist (see discussion in [50, 67]), which can be enhanced by use of a radical quencher.[80] For this reason, radical resists possess the highest resolution, with the smallest reported patterned size of 60-80 nm (λ/10 of the respective sources).[51] Smaller features have been reported,[81, 82] but these are due to proximity effects where rapid writing in the gap between two larger structures can be used to make very fine fibers due to the cloud of radicals surrounding the previously patterned structures, and are thus extremely limited in possible patterns. Another very interesting technique for making smaller features is through stimulated emission depletion (STED), a technique that, much like MPL, was inspired by florescent microscopy. In this technique (called RAPID in MPL applications),[66] a second pulse or continuous wave (CW) source is used to deactivate by stimulated emission excited initiators before they can complete initiation (generation of radicals, etc). This second source is passed through a phase mask (or multiple sources and masks can be employed) that gives the beam a different shape (such as a torus or multiple high intensity spots), which then are made coincident to the excitation beam. The areas overlapping between the two focal spots are deactivated leading to a smaller excitation area. The most interesting aspect of this is that, while each beam is optically limited, their overlap is not. This has been reported to reduce the feature size from 200 nm to 80 nm, and also to greatly improve the axial resolution, which is always worse than the lateral in MPL systems due to confocal limitations of the spot shape leading to an ellipsoidal spot. Another key aspect of MPL is that, despite its serial nature, it is potentially scalable by use of a multilens array before the focusing optic to provide multiple focal spots. [83]

1.2.6. **Self-assembly**

Self-assembly is another powerful tool for 2D and 3D fabrication of micro/nanostructures. In these bottom-up processes, the natural arrangement of a particular structure is built into the chemical or physical parameters of one or more building blocks. The families of materials that have been studied for self-assembly are too numerous to list, but two of the most successful that are highly relevant for the generation of controllable 3D architectures would be colloidal systems and BCP.

Colloidal crystals are macromolecular assemblies of micro or nano-scale particles formed out of solution. The composition of the particles can range from organic polymers[84] and bioparticles[85] to inorganic glasses,[86] metals,[87] or ceramics.[88] In all cases, secondary van der Waals interactions are the primary driving force for assembly. Despite this, by utilizing either slow evaporation times or various other techniques such as electrophoresis,[86] crystals of very high quality over a large area (up to cm scale) can be obtained. Colloidal crystal arrays have been employed extensively for photonic structures,[84, 85, 88, 89] phononic crystals[90, 91] and energy dissipative structures.[92] One disadvantage to colloidal systems formed by the most commonly employed monodisperse spherical colloids is the fact that they generally all form in the same crystal structure (f.c.c., $Fm\bar{3}m$) and, thusly, all with the same filling fraction. This limitation has been overcome with a variety of strategies, such as using multiple particle sizes (also allowing for multiple functionalities with controlled positioning),[93, 94] pattered substrates,[95] or adding coordinating functionality to the particles by DNA surface binding.[96-98] The net result is a huge increase in the possible number of colloidal crystal structures.

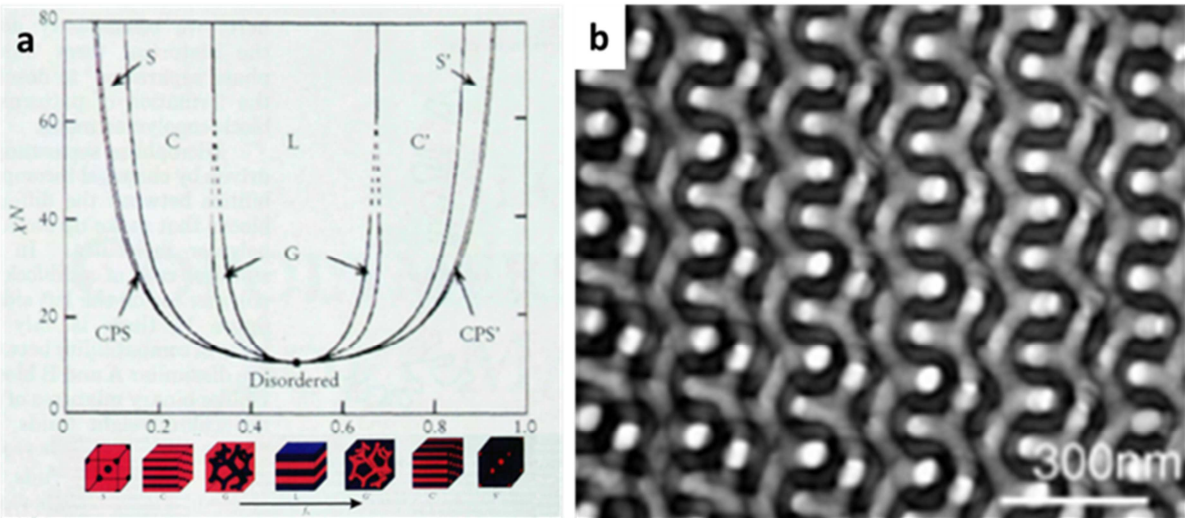

Figure 1-4: (a) Phase diagram of diblock copolymer plotted as a function of χN, temperature dependent interaction energy and the length of the overall polymer, versus the fraction of polymer B.[99] (b) TEM image of double gyroid diblock copolymer self-assembly, the most complex 3D diblock structure.[100]

BCP self-assembly is another route to multidimensional structures that has been the topic of a great deal of investigation.[101] For BCPs made of two or more varieties of immiscible polymers covalently joined end-to-end (or in more complicated architectures such as miktoarm star copolymers[102]), the BCPs undergo microphase separation with microdomains size commensurate to the relative block molecular weights and the period to its overall composition and total molecular weight. The arrangement of these domains is dependent on the relative compositions of the individual blocks and the nature of their connection. For example, in the simplest case of a diblock copolymer (Figure 1-4), there exist four distinct phases (in order of decreasing fraction of the minority block): (1) lamellae, (2) double gyroids of the minority phase in a matrix of the majority, (3) hexagonally packed minority cylinders, and (4) BCC packing of minority spheres.[103] Structural variants of these phases may also be obtained by various means, such as the formation of a helical variant of the cylindrical phase due to a chemical choice of the backbone of the minority phase.[104] Additional symmetries are available by adding complexity to the BCP, such as by moving to a terblock,[99, 105] leading to more than ten new distinct phases. Blending nanoparticles into a BCP solution can also result in highly structured bi-composites due to the ability of

the nanoparticles to reside in low energy regions within the polymer medium, dictated by the geometry and scale of the block domains and the enthalpic interactions of ligands on the nanoparticle surfaces.[106, 107] Applications of BCP include photonic[100, 108] and phononic[109] crystals, which, by virtue of the soft nature of the BCPs can, by selective crosslinking and swelling, have their photonic and phononic dispersion tuned by a variety of stimuli.[108, 110]

1.2.7. **Combined approaches**

All the techniques discussed above possess advantages and limitations. The most general areas of comparison for the various fabrication techniques are patterning rate, degree of structural control and resolution. These parameters are generally not completely independent. Most obviously, rate and control are generally inversely coupled. For example, the most rapid methods, such as techniques using single or multiple exposures (imprint, photomask 2D lithography, glancing angle processes, microprojection, and IL) and self-assembly techniques can pattern a large area (mm-cm scale) in a single lithographic step. While layer-by-layer techniques fall into this category, most of them (other than microprojection lithography) when applied to 3D structures require many intermediate steps that slow down the process. The drawback of these techniques, especially in 3D, is that there is often very limited control over both the naturally occurring and desired defects. This is a particularly large problem in self-assembled structures that contain thermodynamic or kinetically frozen point or line defects. Conversely, IL processes can rapidly pattern a large area uniformly in 3D, but cannot controllably define point defects. In contrast, DW techniques, such as 2D e-beam or laser ablation and 3D printing or MPL, can provide nearly arbitrary control over the structure with the limitation of serial writing. The rate at which these serial processes can occur is often coupled to the resolution of the process, with μm-mm scale DW patternable at m/s rates, while fine MPL structures, writable down to a demonstrated 65 nm,[111] is generally limited to mm-cm/s depending on the simplicity of the patterned structure. Self-assembly is an exception to this rule; for example, BCP self-assembly techniques have the potential for the highest resolution as their characteristic length is limited by molecular dimensions (1-100 nm) rather than optical or mechanical

positioning and can pattern wide areas simultaneously with the drawback of the aforementioned defects. These parametric tradeoffs have led me to my research into combined techniques.

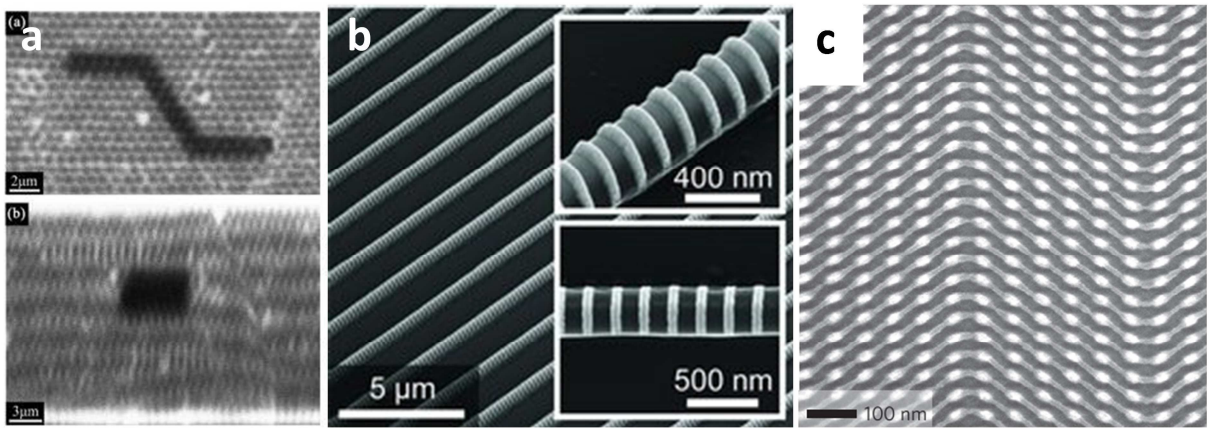

Figure 1-5: Examples of combined strategies for hierarchical 3D structures. (a) Confocal microscopy of a defect written by MPL within a colloid structure. The top image is a planar *xy* map of the defect, while the bottom shows an *yz* cross-section.[112] (b) Gold resonators fabricated by metallic deposition through an e-beam mask on laser DW lines.[113] (c) Self-assembly of a BCP on a complex post pattern. The cylindrical morphology adopts a minimum energy assembly around the posts leading to a unique pattern.[114]

One example of combined techniques is the utilization of 3DDW, usually by MPL, to introduce purposeful defects and create local hierarchical structures in 3D media previously patterned either by IL,[115] direct ink writing,[116] imprint,[117] or colloidal self-assembly (Figure 1-5a).[89, 118, 119] In the case of the structures written on the imprinted pillars, micromechanical actuators were made by patterning in a hydrogel by MPL.[117] Other studies focused on optical devices. A similar approach has been made using conventional short wave UV to fix a photocrosslinkable BCP that had been previously annealed for self-assembly,[120] the second block was then degraded to leave a fine featured hierarchical structure consisting of pores possessing the morphology of the removed blocks. In the above techniques, the fine structure was determined globally by the large area technique and then either altered or positioned by application of the second technique for a resultant binary product of either the 3D structure or fully filled/unpatterned area. A more recent combined DW approach involved exploiting the curvature of 3DDW lines to deposit

gold e-beam "stand-up" plasmonic resonators (Figure 1-5b)[113] (similar to previous work done on IL-defined templates).[121]

Another area of technique combinations is the epitaxy of self-assembled structures. These techniques have been used extensively to guide the formation of BCPs in two dimensions by either chemical[122, 123] or graphoepitaxy[124-126] to order and align the polymer microdomains. In the latter method, polymers are restricted by either a surrounding (produced by e-beam or IL) or embedded geometry (due to resolution requirements, produced exclusively by IL, Figure 1-5c) and are forced to adopt some lowest energy morphology commensurate to the arrangement. For larger area ordering, unstructured, field driven methods of BCP alignment, such as magnetic,[127] electronic,[128] mechanical,[129] thermal,[130-133] or directional solvent[134] evaporation or crystallization[135, 136] driven alignment. Epitaxy of 3D self-assembly is a less studied area, though it has been demonstrated for colloids within conventional lithographic or IL templates[137, 138] and BCP within ordered and disordered pores.[139-141]

1.3. *Equipment*

While a variety of distinct experiments were conducted as a part of this research, many employed the same equipment, which will be detailed in this section.

1.3.1. **Direct write laser system**

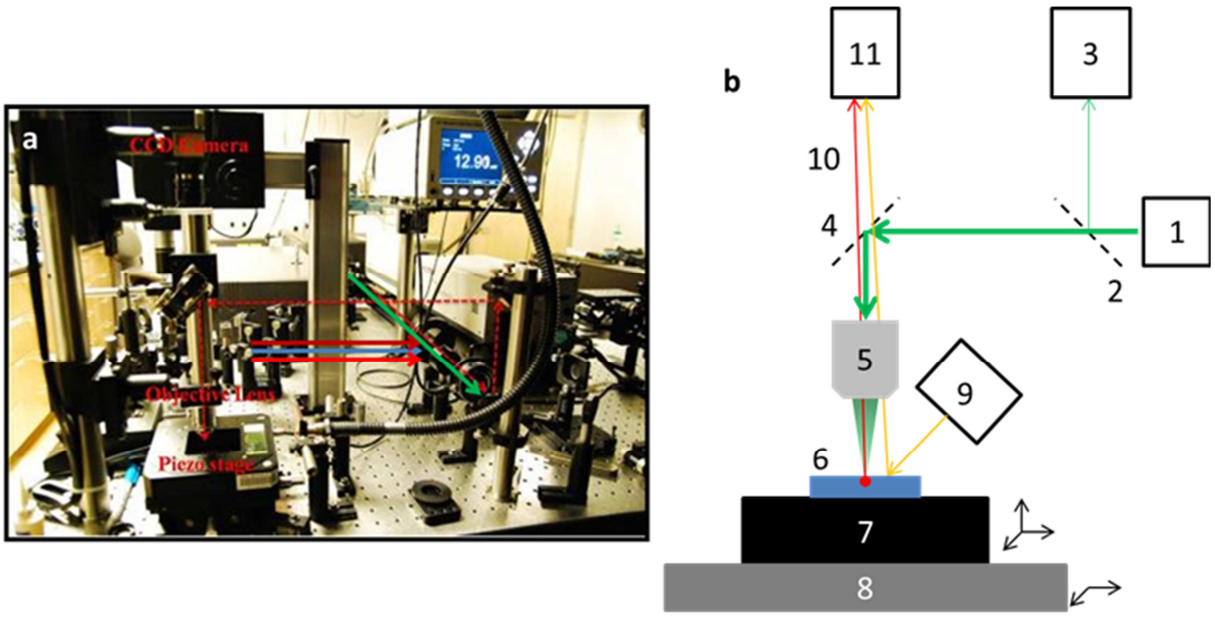

Figure 1-6: (a) Photograph of DW setup illustrating key components and laser paths. (b) Schematic of direct write setup for green. The laser is first passed through a power modulator (1) of one sort or another (possibly within the laser itself). Part or all of the laser beam is then separated by a partially reflecting or removable mirror (2) and measured with a power meter (3). The beam is then reflected by a dielectric mirror (4) through the microscope objective (5) and into the sample (6). Patterning is accomplished by an *xyz* piezo stage (7) placed on top of a course positioner (8). The sample is observed in two ways: through reflected light from an external source (9) that is of a wavelength to pass through (4) or broadband fluorescence from the sample (10). Both of which pass through the objective lens (5) and into a CCD camera mounted above (11).

The system that was used for DW in all studies was a home-built optical table setup, shown in Figure 1-6. Motion of the sample for DW was enabled by a LabView-controlled Physik Instruments PIMars™ piezostage with 300 μm of travel on all three axes mounted on a course micrometer or a Physik Instruments M-686 electromechanical stage for larger motion. In this way, the sample was moved relative to stationary optics, through which the laser was passed. The specific optics and laser depended on the experiment and, furthermore, the evolving state of the laser system. Most generally, the sample was either illuminated from below (or not at all) with orange light which passed through an objective and a partially reflecting mirror selected for the laser light of the experiment and into an imaging CCD camera for

monitoring the experiment (patterning fluorescence was also monitored). The partially reflecting mirror from the other direction could be used to send laser light into the objective for patterning. The laser beam was passed through an electronic shutter for digital beam control and the power was measured either by using a removable (earlier experiments) or static beam-sampling (R=9-20%, dependent on wavelength) mirror into a Newport 818-UV power meter. The other important parameters of a given writing setup were (1) the wavelength laser used, whether it was a pulsed system or not, (2) the polarization, and (3) the numerical aperture (NA) of the objective. The lasers that were used are listed in Table 1-1, while the objectives are in Table 1-2.

Another important distinction between various laser setups was the way that the laser power was modulated. This broke down to three methods: (1) a Thor Labs neutral density filter wheel (ND), (2) a Brimrose TEM-85-2-780 acousto-optic modulator (AOM), and (3) CUBE (C), OBIS (O) or Verdi (V) direct voltage modulation. The ND filter simply utilized passing the laser through a partially transmitting coating that could be adjusted by manually rotating the wheel. Though this imposed a slight slanted-gradient in the intensity profile dependent on the size of the beam, it provided little overall change to the beam shape. The AOM utilized an electronically modulated acoustic grating to controllably separate the incident beam into a 0^{th} order and 1^{st} order set of diffracted beams with varying relative ratios. The net result was a software-controlled amplitude of the 1^{st} order beam from no power to some maximum fraction (~80%) of the incident power. Unsurprisingly, the AOM response is highly dependent on incident wavelength and thus could only be used at 780 nm without complete reconfiguration of the optics. Drawbacks of this method were that the optics required led to a distorted beam shape and a slight time-variance to the beam power. This latter effect did not significantly change the focal spot size when optimally aligned, but led to undesirable effects on grating based patterning to be discussed in Chapter 3, so the ND wheel was used. The C/O control relied on direct voltage control of the output of a Coherent CUBE/OBIS laser system, which, while not affecting the beam properties, did have the disadvantage in the C control of possessing a minimum power output (~10% of the beam total power) due to drift of the

modulation circuit without an applied load. Finally, the V control utilized a power output wheel on the Coherent Verdi V5 to control power. This system is only stable at 80% of its full output (~8 W) and is quite old, so the net result was power fluctuation on the order of 1-3%. This seemingly low quantity was in fact a significant drift with relation to the processing windows of BCP studied in Chapter 5. Somewhat more inconvenient was the drift in alignment experienced due to this lack of stability.

As there are several laser configurations, it is useful to define a code for the system being discussed, which will go as follows: polarization (linear [L] or circular [C])-laser code-objective code-power adjusting method. For example, L-780P-A_0.7-AOM would refer to an experiment utilizing linearly polarized 780 nm light from a Coherent RegA Ti:Sapphire amplifier laser system operating at an 80 MHz repatition rate with 160 fs pulses through a 0.7 Nikon free space objective modulated by the AOM.

Table 1-1: Specifications for lasers utilized for lithography

Code	Model	λ (nm)	Rep. Rate (Hz)	Pulse Width (s)
780P	Coherent RegA Ti:Sapphire Amplifier	780	8×10^{7}	1.6×10^{-13}
780CW	Coherent RegA Ti:Sapphire Amplifier	780	Continuous Wave	-
532	Coherent Verdi-V5	532	Continuous Wave	-
660O	Coherent OBIS 660 LX	660	Continuous Wave	-
660C	Coherent CUBE 660-100C	663	Continuous Wave	-
640C	Coherent CUBE 640-100C	643	Continuous Wave	-
355	Spectra-Physics Quanta Ray Lab 150	355	10	9×10^{-9}

Table 1-2: Specifications for objectives utilized for DW

Code	Model	Numerical Aperture	Medium
O_1.3	Nikon CFI S Fluor 40X	1.3	Oil
A_0.7	Zeiss Epiplan 50X	0.7	Air
A_0.4	Zeiss LD Achroplan 20X	0.4	Air

1.3.2. **Microscopy**

A majority of the analysis was performed by scanning electron microscopy (SEM). For resist studies (Chapter 2 and Chapter 5), the imaging was performed on a JEOL 6060 at an accelerating voltage of 5 keV. All images presented were either taken at normal incidence or a 30° tilt. For studies discussed in Chapter 3 and Chapter 4, higher resolution was required, so SEM studies were utilized by etching away the polystyrene (PS) either into the silicon substrate (in Chapter 3) or just removing the PS block from the poly(styrene-b-dimethylsiloxane) (PS-PDMS) leaving SiO_x from the PDMS (in Chapter 4). These samples were observed by a JOEL 6700 system at 5 keV, at times with a tilt of 25º. Focused ion beam (FIB) cross-sections were performed on a JEOL JEM-9320FIB. Optical images were obtained on a Zeiss AxioSkop 2 MAT with objective A_0.7. Aside from the etched silicon samples (in Chapter 3), all SEM samples were coated with 12-16 nm of AuPd using a Quorum Technologies Polaron SC7640.

1.3.3. **Spectroscopy**

UV-Vis spectra were collected on a Cary 6000 spectrometer in transmission mode. Ellipsometry for film thickness measurments was performed with a J. A. Woollam Co. M-2000D spectroscopic ellipsometer.

1.3.4. **Simulations**

This research includes acoustic, mechanical, optical, chemical, and thermal finite element method (FEM) simulations, which were performed with COMSOL Multiphysics 4.x (with the version changing during the course of the work). COMSOL allows for simultaneous solution of multiple differential equations in the same model. Some coarse simulations in Chapters 4 and 5 were also performed with MATLAB. As no development of FEM code was done during this work, it will only be discussed where it is relevant.

2. Focused Proximity Field Nanopatterning

2.1. *Introduction*

Soft-lithography proximity field nanopatterning (PnP) has been used as a technique to increase the dielectric contrast and pattern control of conventional PMIL. The technique departs from conventional PMIL by utilizing a soft-lithographic process to generate a proximal 2D surface relief pattern, the entirety of which is the active optical element, as opposed to having an optically interacting stamp volume. The innovation of the presented technique, referred to here as focused proximity field nanopatterning (FPnP), is replacing the global optical exposure with a local focused source. As such, localized patterns based on a combination of the beam parameters and the diffraction orders of the surface mask can be defined in a single shot.

A schematic of the steps of the FPnP process is shown in Figure 2-1. Each given mask and set of beam parameters generates a family of patterns, each with a constant angular shape of different overall size, (to be generated) depending on the focal position relative to the mask. FPnP is easily combinable with point spread (PSF) manipulation, recently demonstrated for the single shot fabrication of gear-like structures.[142] Simple modifications to the technique allow for multiple patterning steps. For example, *in situ* removal of the surface mask allow for consecutive, registered 3DDW to enable incorporation of features disparate from those defined by the mask. Additionally, use of a sacrificial layer (SL) allow for cross-sectional control of the patterns formed.

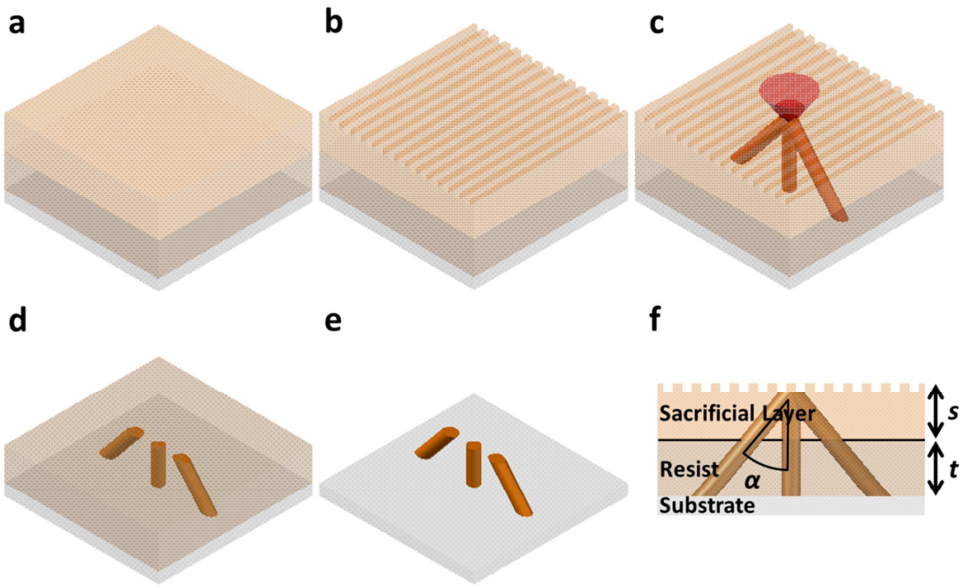

Figure 2-1: Scheme for FPnP. (a) Photoresist and optional sacrificial layer are spun coat sequentially onto the substrate. (b) At elevated temperature (>60 °C) the surface mask is imprinted into the top surface. (c) FPnP patterning is performed by multiple single shot exposures. (d) Sacrificial layer is removed, at this point another cycle of patterning and/or 3DDW can be performed, after final patterning post exposure bake is executed. (e) Sample is developed leaving the final structure. (f) Cross-section of patterning with key parameters, resist and sacrificial layer thickness (*t* and *s*) and branch angle (*α*) indicated.

Structures made by this process all share key similarities in their morphology due to their origin and thus represent a reduction in the arbitrary freedom of 3DDW. These patterns, however, may be produced orders of magnitude faster depending on beam parameters and the fabrication system. Thus, one needs to understand the nature and range of types of motifs that are accessible by FPnP and note promising structural and materials composite applications. "Stand-up" plasmonic microresonators, which generally requires detailed, many-step fabrication processes,[121, 143-145] are one such application area.

2.2. *Methods*

The photoresists used in this study are commercially available negative tone SU-8 2005 (Microchem). Sacrificial layer was made utilizing 20 wt% low molecular weight polystyrene (2k, Fluka) dissolved in cyclohexane (Sigma-Aldrich). All materials were used as received, with the exception of SU-8, to which,

for some experiments, 0.5 wt% of 2-isopropyl thioxanthone (ITX) was added as a multiphoton sensitizer. This allowed for shorter exposures, but also affected on the overall shape of the structures.

For FPnP SU-8 was spun onto a substrate consisting of a previously crosslinked adhesion layer (<1 μm) of SU-8 on a glass coverslip with a 500 rpm spreading spin (10 s) followed by a 1500-3000 rpm spin (30 s). Spin speed determined the thickness of the FPnP sample. The under layer of SU-8 acted as an adhesion layer. Soft bake was then performed at 95 °C for >5 min. At this stage polystyrene SL is then spun on with a similar 1500-3000 rpm spin. Next, a PDMS phase mask is brought into contact at room temperature and then imprinted with light pressure by hand at 95 °C for ~10 s to form a replica of the phase mask pattern. FPnP patterning and 3DDW were both performed using L-780P-A_0.7-ND laser arrangement. Continuous wave 532 nm exposure was performed with the L-532-A_0.7-ND arrangement. Exposures are shown for near IR with focus 2-4 μm below the grating were performed between 25-45 mW of power depending on the thickness of the sacrificial layer for 400 or 800 ms while the sample with focus 8 μm above the grating (Figure 2-2c) was performed at 75 mW for 8.1 s. Structures fabricated with green light shown in Figure 2-5a were made with 800 ms exposures at 85 mW. Samples shown above were generated with 400 ms single shot exposures at various powers. After exposure, post exposure bake was performed for 1 min at 65 °C and 1 min at 95 °C. Sample development was done by immersion in propylene glycol methyl ether acetate (PGMEA) for 10-20 minutes, followed by immediate dipping in isopropyl alcohol (IPA) to rinse the PGMEA and development byproducts. IPA doubly serves to rinse to act as a lower surface tension solvent to limit the capillarity induced collapse of the written structures. For consecutive 3DDW, surface pattern was cleared by 10 s hotplate heating at 95 °C and then realigned by eye using the contrast of the previously written structures.

Far-IR FTIR measurements were performed on the U12A IR beamline at the National Synchrotron Light Source at Brookhaven National Laboratory. Samples were measured on a Continuμm IR microscope (Thermo Scientific) in reflection geometry using polarized light and a Si bolometer detector. The objective used for the measurements was a Schwarzschild-style NA=0.58, 15X objective. Scans were

taken with 4 cm^{-1}, and surrounding metalized area was utilized as background. To prepare samples for resonance measurement 45-60 nm of gold were deposited at 45° four times with 90° rotation between each deposition using a Desk II Sputterer (Denton Vacuum).

2D simulations of FPnP intensity distributions are performed in a 20 μm square cell with scattering boundary conditions (estimations of perfectly absorbing layers). 9.5 μm of air above 5 μm of resist placed on 5.5 μm of glass are used as the sample. Laser illumination is simulated using the analytical Gaussian equation with polarization of the electric field perpendicular to the cell. The 3D simulation of the 2D mask was performed by using a quarter of the cell bounded by a perfect (electric/magnetic) conductor to act as a mirror symmetry for (magnetic/electron) portions of the polarization. 3D resonator simulations are performed with a 15 μm cube cell with periodic boundary conditions in the *x* and *y*. Substrate and structure are simulated as effective impedance boundary using the conductivity of gold ($4x10^7$ $S \cdot m^{-1}$). To attempt to match the Schwarzschild-style objective to reproduce the experimental results, tilted incidence was used at 35.5°, which is the edge of the light cone for an NA=0.58 objective.

2.3. *Fabrication of structures by FPnP*

Any phase mask process is governed by the diffraction of the incident light by the periodicity of the mask into various beam orders. In the near-field, these beams interfere to produce the 3D pattern. The general 1D diffraction equation for light entering a resist from air is:

$$d\left(\sin\theta_i + n\sin\theta_d\right) = m\lambda \qquad \textbf{Eq. 2-1}$$

Where d is the periodicity of the mask, $\theta_{i/d}$ is the incident/diffracted angle of the light, n is the index of the resist, m is the order of the diffraction and λ is the incident wavelength. In typical phase mask IL, θ_i=0, which leads to symmetric interference of the positive and negative orders dependent on the ratio of the mask spacing and the illumination wavelength. In FPnP, however, there are a range of angles in the convergent/divergent beam, and also a beam width at the grating is on the order of the lattice parameter or

less, leading to a low resolvancy (or sharpness of the diffracted beam). The spot size incident on the grating of the Gaussian plane wave focused by the objective lens can be determined by the following:

$$w \approx \frac{\lambda}{\pi NA}\sqrt{1+\left(\frac{\pi NA^2}{\lambda}Z\right)^2} \qquad \textbf{Eq. 2-2}$$

Where Z is the distance of the grating from the focal plane. The FPnP process possesses several degrees of freedom in both the positioning and the final morphology of the fabricated structures, all of which involve the manipulation of elements in either Eq. 2-1 or Eq. 2-2. While this discussion will concentrate on structures produced by FPnP on 1D grating masks for ease of simulations, the concepts discussed are equally applicable to 2D masks with the main important consideration being that the greater number of diffracted beams reduces the fraction of the intensity in each.

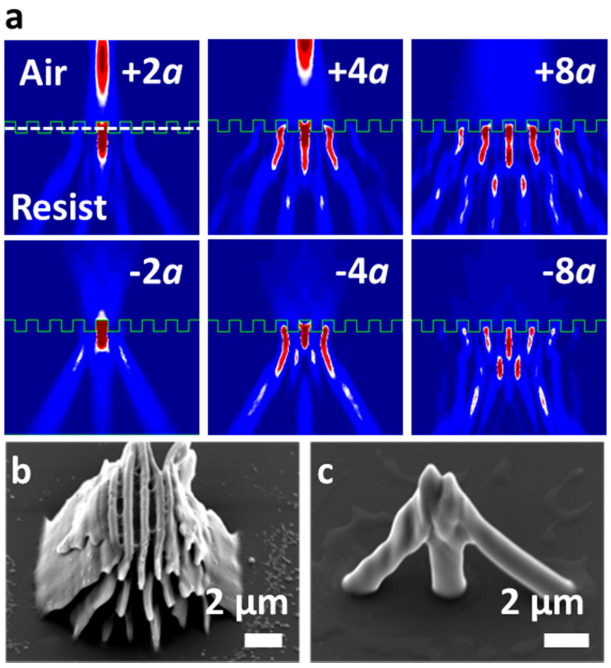

Figure 2-2. (a) 2D FEM simulation of two-photon intensity pattern from 0.78*a* wavelength light with varying focus through an *a*/2 square wave surface imprint. Top row from left to right is focused placed 2*a*, 4*a*, and 8*a* above the imprint midpoint (indicated by dashed line). Bottom row is 2*a*, 4*a*, and 8*a* below the midpoint. (b-c) tilted (30°) SEM images of two SU-8 structures fabricated at different focus heights with 780 nm light and *a*=1 µm. (b) Focus 8 µm above, is representative of interference dominated structures, while (c) focus 2 µm below, is representative of diffraction dominated.

2.3.1. Control of structure by variation of focal position

As discussed above, the primary difference between conventional PnP and FPnP is that the plane wave exposure source is replaced by a focused beam. Figure 2-2 depicts 2D FEM simulations of the two-photon intensity pattern from an 780 nm light source focused (NA 0.7) through a 1 µm periodic square surface grating imprinted 0.5 µm deep into a 5 µm thick SU-8. It should be noted that that all of these parameters are scalable, and thus may be considered in units of the grating period assuming, as in these simulations, that the wavelength dependent optical properties of the resist such as absorption are not considered. There are several clear varieties of local patterns in intensity contrast. When the focus is just above or below the grating (<2x the mask period, Figure 2-2a top-left), the simulated pattern contains

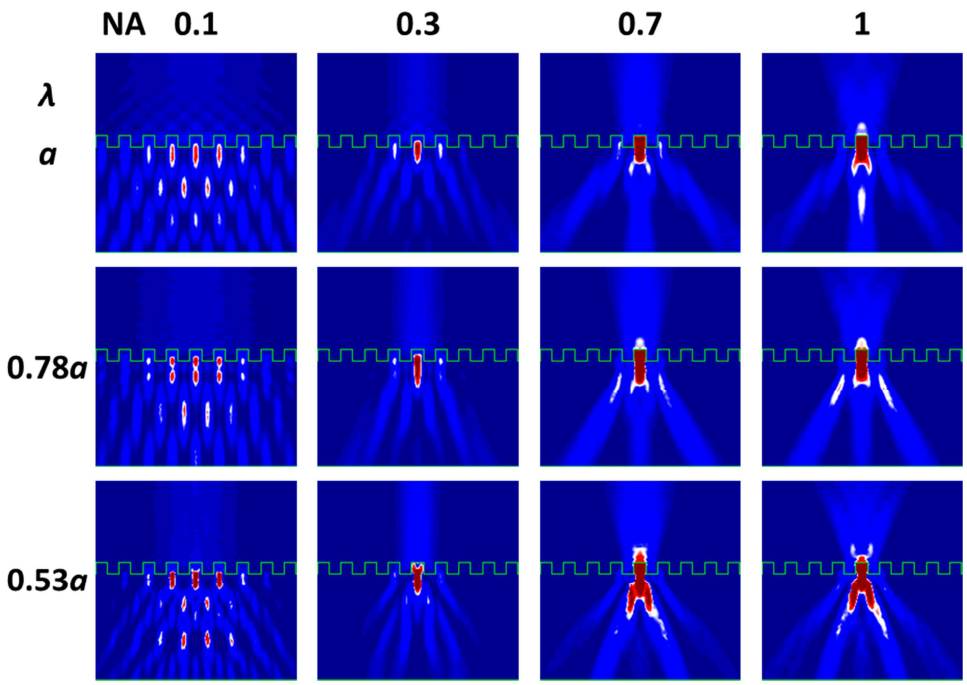

Figure 2-3. FEM simulations of two-photon intensities for a variety of NA and λ values of a beam focused 2*a* below the surface of the structure described in Figure 2-2. It can be seen that these two parameters can control the aspects (angles/number of beams, proportion of intensity in each beam) of the final intensity pattern.

features dominated by the diffraction orders of the beam. By a combination of the beam size and divergence from a plane wave, the resultant diffraction occurs at a range of angles, with a net "branch" of high intensity occurring where the scattered light of various portions of the beam is most in phase, thus generating the maximal contrast for transfer to the resist. For these reasons, this effective diffraction angle, ~26°, is not that predicted by Eq. 2-1 (29.8°). In contrast to the near focus, as the focal plane gets further away from surface grating, the illumination area grows in size and the local pattern begins to take on the features of conventional interference. The resulting patterns, however, possess tilted features due to the wide range of incident angles included in the convergent/divergent focused beam. As described below, a surface imprint can be created by pressing an elastomeric stamp into resist materials heated above their flow temperature. Examples of both types of structure fabricated in SU-8 utilizing a polydimethylsiloxane (PDMS) mask with the same dimensions as the simulation are also shown in Figure 2-2b,c. Despite the 2D nature of the simulations, the experimental structures demonstrate excellent agreement with the

simulated intensity distributions in their central cross-section as the 1D surface grating does not greatly alter the parallel beam distribution.

2.3.2. **Control of structure by beam parameters**

While the focal position of the beam to a large extent determines the morphology that will be fabricated by the FPnP process, many characteristics of the structure are set by the beam wavelength and the objective's NA which controls to the range of incident angles of the illumination. Figure 2-3 shows a table of simulated intensity patterns at various normalized wavelengths and objective NAs for a given focus (2 μm below the grating center). Tuning of the laser wavelength changes the angle and number of diffracted orders as described in Eq. 2-1. It also changes the diffraction efficiency of the grating and thus the relative dose and feature size of the diffracted branches. For example, Figure 2-5 (a) shows the transition from three to two branches by using near IR or green 3DDW respectively. In the case of the sub-imprint green light, the 0^{th} order is relatively suppressed with respect to the 1^{st} orders. This is an especially attractive method for tuning the structure since wavelength in most tunable laser systems can be set with a high degree of precision for single angle alteration of the diffracted orders. The wavelength also affects the overall spot size, but to a lesser, linear extent. The effect of tuning NA can be more complex as it is coupled to both the spot size given by Eq. 2-2 and the angular range of incident light. This changes the effective branch angle; however, altering the NA with the beam focus near the surface imprint mainly spreads the beam, resulting in patterns similar to that of the mask with plane wave illumination at low NA.

2.3.3. **Effect of lattice registration**

Until this point, the discussion has assumed perfect registration between the surface grating and therefore symmetric patterns. Even though with modern alignment techniques registration is not impossible, it is important to consider to what extent registry affects the fidelity of the patterning. Further, the possibility for *deliberate* symmetry breaking as a potential degree of freedom can be assessed. Figure

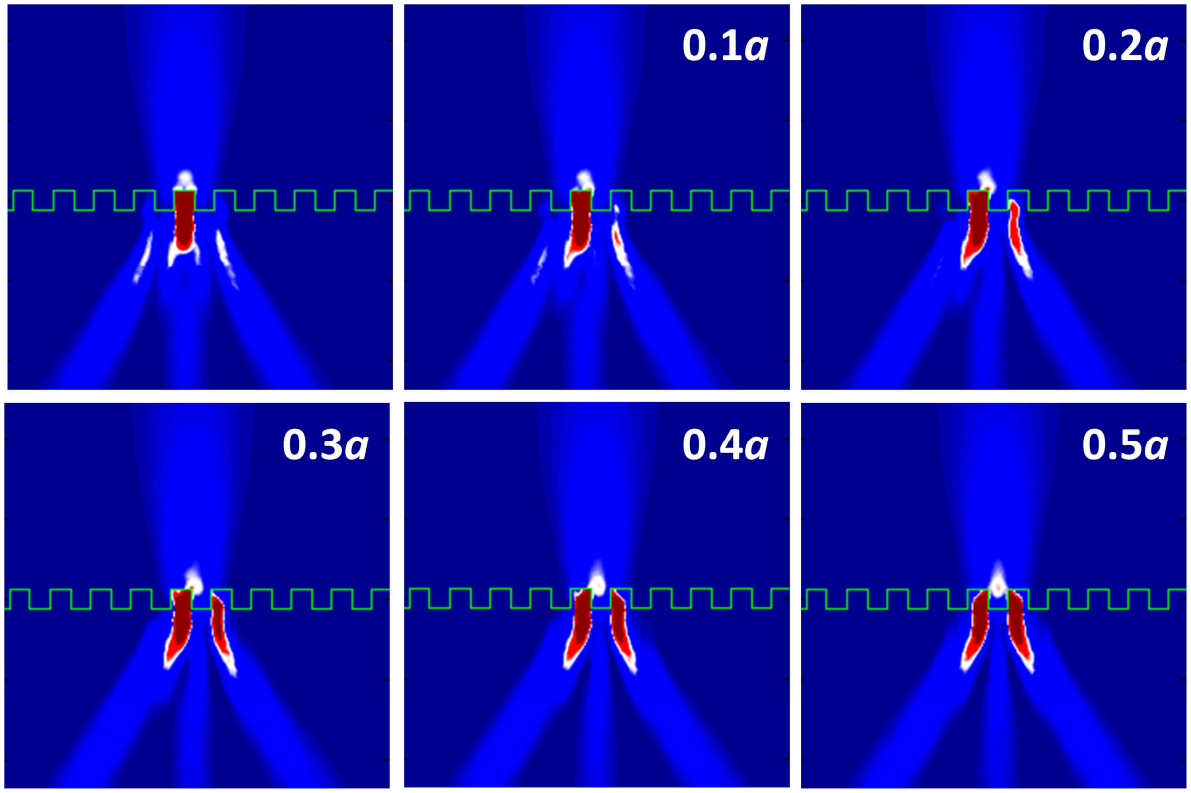

Figure 2-4: Demonstration of the effects of registry on the intensity distribution. While the overall effective angle of the 1st order branches is only altered slightly, the 0th order branch intensity becomes asymmetric changing the relative areas in the unpatterned regions between the branches.

2-4 shows simulation of the progressive variation of the intensity distribution as the lattice registry of a tightly focused beam is broken. The result is that while the overall diffraction angle of the branches does not change significantly, the 0th order beam is deflected, changing the area of one of the two open areas of the structure. This is a subtle effect. As a result, for most applications, registry is not as critical a control parameter as the others introduced, thereby reducing the need for a high degree of registration.

2.3.4. **Sacrificial layer for cross-sectional control**

In conventional IL, cross-sectional control as a concept is relatively unimportant – different sections of the intensity distribution are periodic along the incident axis, and therefore, any sizable portion of the resultant structure can be expected to exhibit similar physical properties. This is not the case for FPnP

structures, which possess no axial periodicity. Because of this, distinct axial slices of FPnP structures will be different, which can lead to useful variations in their properties. In addition to cross-sectional control, another concept generally not critical for conventional IL is proximal positioning (including partial overlap) of multiple motifs.

An SL can be used to enable both of these additional levels of pattern control. A SL consists of a non-photoactive material deposited on top of the resist that is able to be imprinted without affecting the resist. In this way, the thickness of the SL can be used to control the top of the targeted structure, with the bottom portion controlled by the total bilayer thickness. SLs have been used in the past for isolation of 2D cross-sections from colloidal PnP utilizing resist separation by deposition of a thin layer of silica.[36] Rather than utilize an additional deposition technique and hydrofluoric acid etch as in this prior work, it would be preferable to identify a spin-coating-compatible SL material that was soluble in an orthogonal solvent to the resist. Additional important considerations for the SL include a similar refractive index and glass-transition temperature as the utilized resist so to avoid distortion in the optical pattern or require incompatable processing, respectively. A suitable SL material is low molecular weight (<2.5 k) PS, which is soluble in cyclohexane, a non-solvent for most resists. This allows the PS to be spun directly

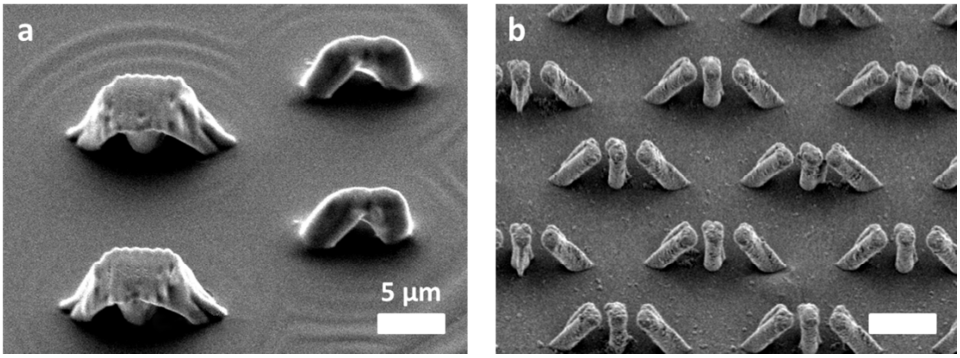

Figure 2-5: Structures generated with two different thicknesses of sacrificial polystyrene layers. (a) Sample with reduced top grating, patterned with both NIR (left, 780 nm) and green (right, 532 nm) 3DDW. (b) An array of structures with removed top grating layer leading to gaps between the branches.

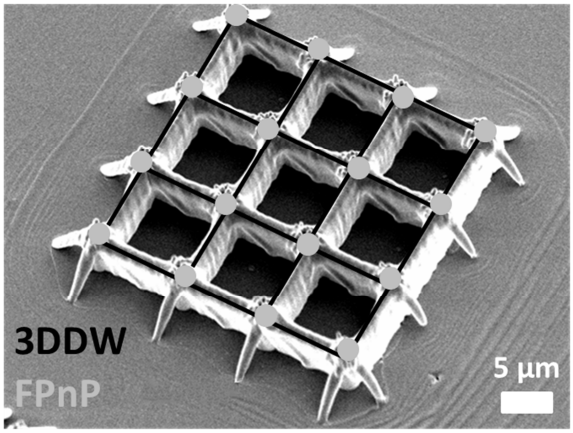

Figure 2-6: Structures created by a sequence of FPnP, surface pattern clearing by heating, and subsequent registered MPL. Realignment for 3DDW patterning step after sample removal and heating was assisted by optical contrast which formed in the FPnP patterned areas after baking the resist due to shrinkage of the exposed resist.

onto a resist layer and removed either with a predevelopment soak step in cylcohexane or in the same developer as the resist. More specifically, we utilized 2 kg/mol PS possessing a glass transition temperature of ~60°C allowing for imprinting at modest temperatures (<100 °C). The thickness of the SL was controlled by spin speed. Figure 2-5 shows structures patterned using polystyrene SLs demonstrating cross-sectional control.

2.3.5. **Consecutive 3DDW**

The enhanced patterning speed of FPnP comes at the cost of the arbitrary freedom of DW which could be detrimental to targeted devices that require additional features not available from the FPnP motif. Since an FPnP system is already designed for DW, consecutive 3DDW is an attractive option for defining these additional features. One way that this can be performed is by the thermal clearing of the surface impr int. By once again raising the resist/SL above the flow temperature, the surface imprint quickly (~1-10s) smoothes by curvature driven flow. For CARs, such as the SU-8 employed in this study, this can be performed as a part of the post-exposure bake (PEB) by either removing, baking, and repositioning or ideally, performing the PEB with an integrated hot-stage. After erasing the original diffractive surface element, conventional, though relatively low NA, 3DDW may be performed (Figure 2-6**).** This is possible because 3DDW in CARs often does not require its own PEB due to the high intensities involved.[60, 61, 146] Alternatively, in such applications where arbitrary high resolution (<500 nm) patterning is necessary,

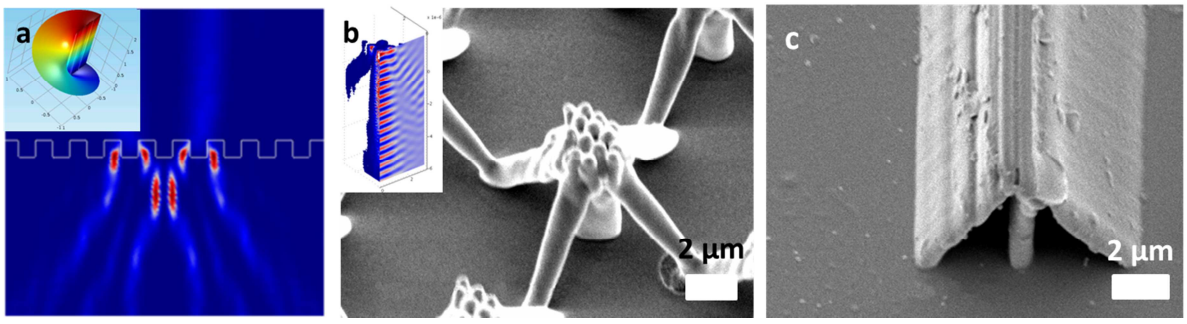

Figure 2-7: (a) Simulated two photon intensity pattern generated by a charge-1 vortex ramp (phase shift progresses as the angle, shown in inset), which can be produced by a commercial optic. (b) Array of structures made with a square array of ~250 nm radius pillars and 800 nm lattice parameter. Compared to the 1D mask discussed in this work the four branch structure has less of the intensity in the diffracted beams and effects of polarization are more apparent. This can also be seen in the simulated intensity (inset). (c) Registered line written following the direction of the imprinted 1D mask forming two enclosed channels with triangular cross-sections.

3DDW may be performed side by side by using top and bottom objectives and a transparent substrate to permit oil immersion (NA>1).

2.3.6. **Other control methods**

It is clear that there are myriad means by which to control FPnP structure formation. Several such means that were not investigated at length are discussed here (Figure 2-7). First, changing the dimensionality of the mask from 1 to 2D (or even multilayer 3D) will of course generate additional beams. This places a practical limit on this method of alteration since each additional diffracted beam will possess less of the overall intensity. While three-branch patterns are impossible, four-branch were tested using 2D imprint patterns of an analogous square mask pattern of 500 nm diameter and height with 800 nm period posts (Figure 2-7a). These patterns tended to have large anisotropy between the various branches as can be seen in the simulation, which could possibly be addressed by utilization of circularly polarized light. Beam shaping was also simulated. Figure 2-7b shows a 2D simulation of a charge-1 vortex ramp, in which the beam shifts half a wavelength radially across the central axis resulting in an

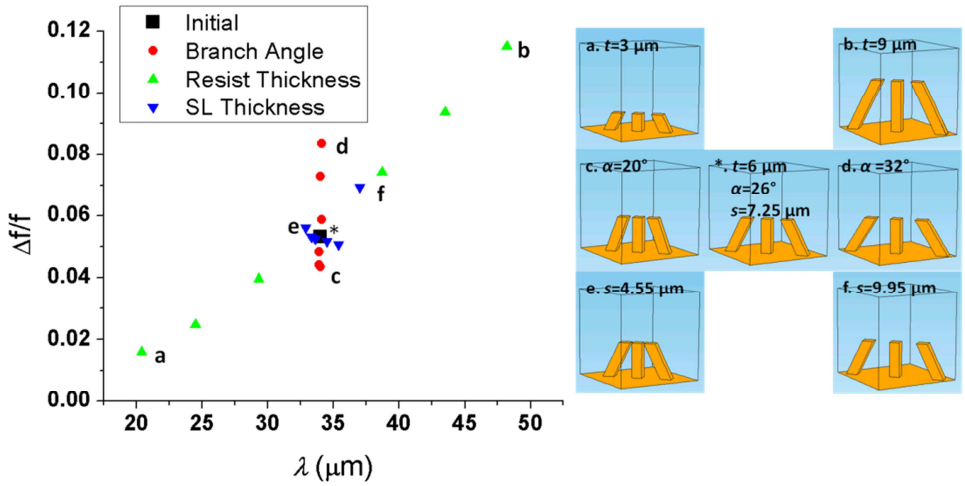

Figure 2-8: FEM simulations of the resonant peak position (*f*) and normalized peak width (*Δf/f*) of arrays of "stand-up" resonators produced by FPnP with varying processing parameters. Initial orientation (*) was chosen to be a similar, simplified geometry to the devices shown in Figure 2-6b: 15 μm arrays, 6 μm resist thickness (*t*), 780 nm exposure (leading to ~26° branch angle (*α*)), and 7.25 μm SL thickness (*s*). Starting from this configuration, *t* (a-b, 3-6 μm), *α* (c-d, 20-32°), and *s* (e-f, 4.55-9.95 μm) were varied to determine the effects of these parameters. Images of the simulated unit cells for the maximum variations in geometric parameters (a-f) and initial configuration (*) are shown on the right side of the figure.

elimination of the 0th order of diffraction. Finally, it is certainly possible to leave the shutter open and translate the beam in the standard mode of DW. If the pattern is commensurate to the motion, for example by following the direction of a 2D imprint, it is possible to create channel-like structures (Figure 2-7c). One interesting extension would be to continuously vary the power and focus while writing to arrive at even more complex gradient channels.

2.4. *FPnP microresonator structures*

One area where FPnP structures are advantageous is the generation of "stand-up" microresonators. Resonators such as ring and split-ring produce their artificial-atom resonances by coupling the magnetic field of incident light into the induction of the ring. In split-ring resonators (SRR), the presence of a capacitive gap acts to shift the resonance to longer wavelengths than the size of device and therefore

allows for low-scattering coupling. One disadvantage to these SRRs is that for micro or nanoresonators fabricated by conventional lithographic techniques, it is simplest to pattern rings in the plane of the substrate. As a result, the coupled light must also be in the same plane for the greatest effect on the magnetic properties (such as effective permeability). For most resonator applications, it would be preferable to couple into light incident perpendicular to the substrate by using "stand-up" resonant structures. FPnP is an ideal technique for the fabrication of such structures via the design methods detailed above, combined with metallization by, for example, multi-angle coating,[147] selective electroless-plating[75] of negative resist structures or backfill electrodeposition[76] of positive resist structures, which have all been previously utilized to generate plasmonic or photonic structures from 3D lithography. In order to determine the ability of the FPnP process to create double SRR-like "W" resonators, SL structures similar to those shown in Figure 2-5 (b), with gold coated structures and substrates, the optical loss properties were modeled with 3D FEM simulations. Figure 2-8 shows the effects of varying several write parameters (resist thickness, effective diffraction angle of the branches, and SL thickness) on the thermal loss due to induced current flow in the SRR with the other properties held constant. Plotted are both the position of the resulting resonance and the relative spectral width as a fraction of the resonant frequency of the peak when fit to a Lorentzian. Variation of the resist thickness can be seen to have the largest effect on both parameters. The observed trend in resonant wavelength is as expected due to linear relation between resonant frequency and resonator size that has been demonstrated in the past for SRR of in this size range.[148] In this case, the correlation is non-linear because the branch thickness and gap size remaining constant while the width of the structure increases. Furthermore, this also resulted in sharpening the peak width as the structures became smaller. Variation of the branch angle displayed some effect on the peak width, but, despite changing the width of the structures, did not significantly affect the resonance peak position. This is an effect of the coupled variation of parameters leading to a cancellation in the overall effect of the change on the resonant frequency, which therefore leads to patterning wavelength being a useful tool in adjusting the peak width of the resonance alone. A similar result can be seen in the variation of the SL thickness, which, despite significantly changing the structural geometry,

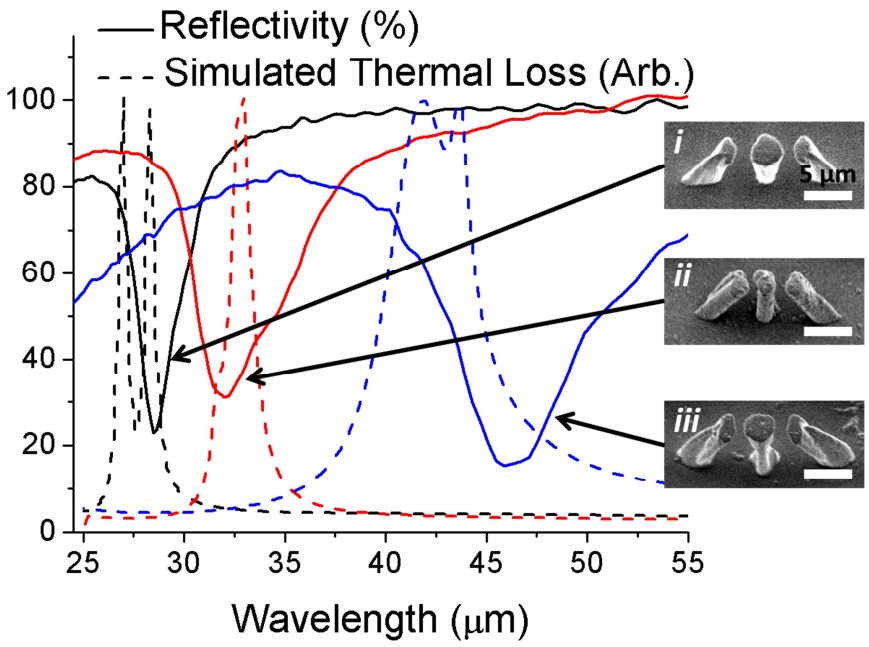

Figure 2-9: Far-IR FTIR reflectivity spectra of the response of resonator arrays fabricated with various sample parameters along with inset SEM images of the structure. Resonant response is indicated by a suppression of the reflectivity. Dashed lines show FEM simulations of simplified structures showing qualitative agreement with the observed results. Parameters of the resonators compared to those in Fig. 6 were *i*) t=4.07, s=9.06, and α=25.72, *ii*) t=5.63, s=8.04, and α=25.82, *iii*) t=7.03, s=6.28, and α=25.45, with additional changes to match the specific features of the structure.

has little effect on the resonant frequency or peak width. It is important to note, however, that the SL is necessary up to the point where the capacitive gap is generated in order to allow for the superwavelength resonance.

2.5. *Conclusion*

By utilizing different thicknesses of resist and SL and beam parameters, we fabricated a wide variety of "stand-up" W resonator array structures, which were then coated with gold and measured with far IR FTIR microscopy. The reflectivity data of a few examples is shown in Figure 2-9. Resonances are observed as suppression of the reflectivity due to absorptive losses of the driven current of the resonant

mode and occurred only when the beam was polarized with the magnetic field perpendicular to the SRRs, this polarization dependence, in combination with the simulations, assured that it was magnetic resonance as opposed to an electronic dipole effect. These results demonstrate that by the simple variation of patterning parameters with a single mask element, it is possible to fabricate resonator structures with superwavelength resonances in a range of wavelengths (here 25-45 μm, or 2-4x the largest dimension of the resonator). Further, based on measurements from SEM images of the structures, it was also possible to refine the FEM model to match the geometry of the actual structures. Specific peak position of the simulations tended to be blue shifted due to approximations in the sample/measurement geometry and electrical properties. Meanwhile, peak width of the experimental results were broadened by the wide range of incident angles of the probe beam which had significant intensity – for the center-blocked Schwarzschild-style IR objective used here, this is a range of angles between ~15-36°. Despite these limitations, the simulations demonstrate the ability to obtain quantitative agreement with the resonant behavior (even in a complex measurement geometry), allowing for predictive design and determination of the proper write parameters for a desired application.

3. Focused Laser Spike Dewetting of Polymer Thin Films

3.1. *Introduction*

The next three chapters will discuss the use of focused laser spike (FLaSk) annealing. The FLaSk technique developed for these lithographic approaches is an extension of laser spike annealing (LSA), an alternative to standard thermal treatment in semiconductor technology.[149-151] In this technique, a high intensity CW or pulsed laser is rapidly scanned across an absorbing surface, such as a silicon wafer substrate supporting the device or polymer film. The local temperature at the laser spot spikes to a high value and then, once the laser light is removed, very rapidly drops back to ambient temperature. Because of this, both the temperature and annealing time of the thin film can be controlled by selection of laser intensity and exposure time. Additionally, annealing can be performed while avoiding unwanted effects, such as material degradation or diffusion. More recently, LSA has been applied to the annealing of soft materials for the microphase separation of BCPs[152] and CAR PEB[153] as will be discussed in greater detail in the relevant sections below.

Much as with FPnP, the approach in FLaSk is to turn the broad-focus LSA into a tightly focused DW technique. This introduces several new aspects to the approach with regards to soft matter. The first is the presence of surrounding confinement. Polymers can undergo large changes in their mechanical properties and dimensions with even mild increases in temperature, especially if those increases cross the glass transition temperature of the polymer. In a FLaSk process, however, the heated polymer is always surrounded by a polymer region of a much lower temperature leading to the potential for very large mechanical strains. The second, following from the first, is the presence of very large (1-1000 K/μm) thermal gradients.

In the thin (<60 nm) films heated from the substrate (2D FLaSk), it was observed that the films would be selectively removed when sufficient heat was applied. This was observed for PS-PDMS BCPs, and

occurred irrelevant of the substrate, though some key features were affected. There were two possible mechanisms proposed for this phenomena: ablation and dewetting. Upon further investigation (decomposition checked in 7.1), dewetting is the most likely explanation. Regardless, the resolution of the effect was very impressive, meriting consideration as a possible patterning technique.

Dewetting has been utilized as a method to generate nanopatterns in thin films of metals[154] and polymers[155] through film-stability-based self-assembly, most generally under near global heat provided by a hotplate or large-area pulsed LSA. In these techniques, the driving force is a large change in the surface energy of the film due to the increased temperature leading to dewetting and growth of isolated droplet features. A related technique based on the flow of liquids down a thermal gradient (the thermocapillary effect)[156-158] has been developed to form large area nanopillar arrays[159, 160] and, most recently, for the nanoscale removal of a protective thin film by resistive heating of carbon nanotubes.[161] The generalized expression for thermocapillary force is:

$$\tilde{\tau} \cdot \hat{n} = \frac{d\gamma}{dT} \nabla T \qquad \textbf{Eq. 3-1}$$

Where τ is the shear stress, $\hat{n}$ the surface normal, and γ the surface tension. The surface tension almost always decreases with temperature leading to a net force down the thermal gradient. In the case of the nanopillars, the thermal gradient was generated along the film normal by using a heated substrate under a thin film, an air gap, and a floated cooled superstrate to create sharp (~50 K/μm) thermal gradients, which drives the formation of the pillars. The nanotube patterning employed similar magnitude gradients to displace a protective thin film above only the higher-resistivity conducting tubes with gradients being essentially 1D, emanating from the nanotubes. For the FLaSk technique, the in-plane gradients generated radially from the spot can be equal to or much greater than those generated in either previous technique. Beyond this, FLaSk provides these gradients on demand locally to a submicron region of the film, thus enabling a DW technique.

3.2. *Mechanism of FLaSk dewetting*

To understand the mechanism of 2D FLaSk dewetting, it is important to first consider what the temperature of the silicon substrate is during line writing. Determining this is complicated by the fact that the polymer layer acts as an anti-reflective coating (ARC) for the silicon. To determine the effects of such an ARC, the transfer matrix method (TMM) is used:[162, 163]

$$\rho_{ij} = \frac{n_i - n_j}{n_i + n_j} \qquad \textbf{Eq. 3-2}$$

$$\tau_d = e^{-i\frac{2\pi n_2}{\lambda}d} \qquad \textbf{Eq. 3-3}$$

$$R = \left|\frac{\rho_{12} + \rho_{23}\tau_d^2}{1 + \rho_{12}\rho_{23}\tau_d^2}\right|^2 \qquad \textbf{Eq. 3-4}$$

Where *i* and *j* are indicies that indicate the layers which the light is propagating from (*i*) and to (*j*) in a particular step, *n* is the index of refraction, *d* is the ARC thickness, λ is the free space wavelength and *R* is the total reflection after all three layers, being air (1), polymer (2), and silicon (3) are considered. The intermediate values ρ_{ij}, τ_{ij}, and τ_d are the reflection, transmission, and phase shift values through the respective layer pairs of the ARC, respectively.

Taking the polymer layer to be an ARC of index *n*=1.55 on the silicon substrate (*n*=4.14), the reflection for 532 nm illumination determined from Eq. 3-4 is shown in Figure 3-1a for one cycle of the periodic film-thickness ARC effect. In a dewetting process, both thinning and thickening occur, since the formed trench generates a surrounding ridge by material displacement. It is possible to identify three regimes of dewetting behavior: (I) where thinning the film increases reflectivity and thickening decreases it, (II) where any sizable change in thickness will result in an increase in reflectivity and (III) where thinning the film decreases reflectivity and thickening the film increases it. Each of these regimes can be expected to have very different pattern formation behaviors. For example, in (III) the temperature initially *increases* as the material thins, raising the risk of crossing the damage threshold, but then cools, making it

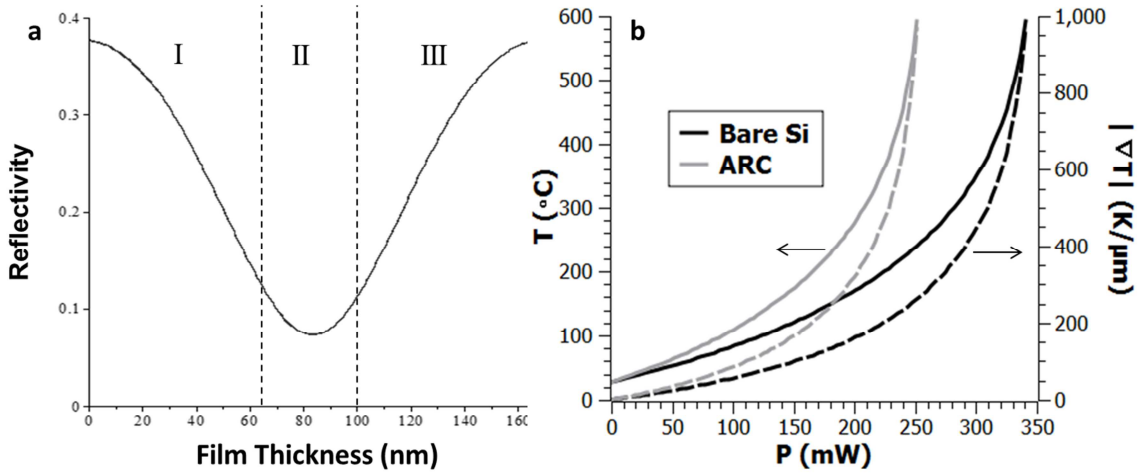

Figure 3-1: (a) Effects on the surface reflectivity of the polymer film considered as an ARC by the TMM. (b) Expected peak temperatures (solid) and thermal gradients (dashed) from FEM simulations for the bare wafer (black) and a 60 nm ARC (grey). Thermal histories of the film start on the grey curve (at a lower effective power) and gradually move to the black at the exposure power as the film dewets.

unlikely that full dewetting will occur. (II) can be considered the "safest" thickness since any large changes in thickness result in cooling. (I) results in cooling in the highest intensity, heated, regions, and additional heating in the ridge areas and was thought to be the best initial target for high resolution patterning for reasons explained below, though all regimes will be explored in the future.

With this as a starting point, FEM simulations were used to estimate the temperatures and gradients that the polymer would experience during the FLaSk anneal. The thermal profile was analytically modeled as a Gaussian source (NA=0.4) along with the optical absorption and heating that would be expected to occur. For materials properties, temperature-dependent values for silicon substrate were utilized for the thermal conductivity, heat capacity, and density.[164] The optical absorption also displays an exponential dependence on temperature, so it was simulated using a previously derived empirical model for near-intrinsic silicon excited with 532 nm light.[165] Finally, the starting point for the absorbed power by the substrate (to be modified by the ARC results) was determined by measuring the damage threshold of a bare wafer (350-355 mW), which corresponds to a peak temperature of ~1400 °C where the silicon

surface melts.[166] Using these simulations, it is possible to plot the range of peak temperatures and thermal gradients expected for a given power as the film dewets (Figure 3-1b). A typical thermal profile (which can be seen in Chapter 4 as the Z=0 trace in Figure 4-2b) consists of a FWHM=~1 μm Gaussian distribution, which for the 100 μm/s speed employed in this study translates roughly to a 10 ms thermal spike. During this excursion the optical absorption can be expected to track through a range of temperatures as the film heats from the moving source and simultaneously dewets and then cools. This is a highly complex process since the film will heat faster when it is thicker and thus likely thins before the peak temperature is reached; however, the largest magnitude thermal gradients, which are spatially in front of the temperature peak, may be experienced during this process. As a result, the full kinetics will have to remain for future work, but could be approached by an elaboration of the 1D method developed by others.[161] Regardless, it can be seen that for the power range employed (200-320 mW) gradients of approximately 100~1000 K/μm, around an order greater than those from vertical dewetting, can be expected.

3.3. *Experimental results of FLaSk dewetting*

3.3.1. **Experimental parameters**

Lightly doped p-type silicon substrates ([100] orientation, 10 Ω·cm) were coated with films of PS (18 kg/mol, Sigma Aldrich) from 1.8 wt% solutions in PGMEA to prepare films of 50-60 nm thickness by spin coating. Patterning was performed with system L-532CW-A_0.4-V. Patterns are transferred from polymer into Si layers using STS ICP-RIE. The etching gas is a mixture of C4F8/SF6 with a 2 min etching time at a power of 1200 W and gas rates of 50 and 80 sccm respectively. AFM imaging was performed with a Veeco Dimension 3100.

3.3.2. **Demonstration of pattern transferred FLaSk dewetting**

The results of this dewetting can be observed by AFM, as shown in Figure 3-2a for isolated FLaSk lines patterned at different powers at a write speed of 100 μm/s. Each line shows two distinct features, (1)

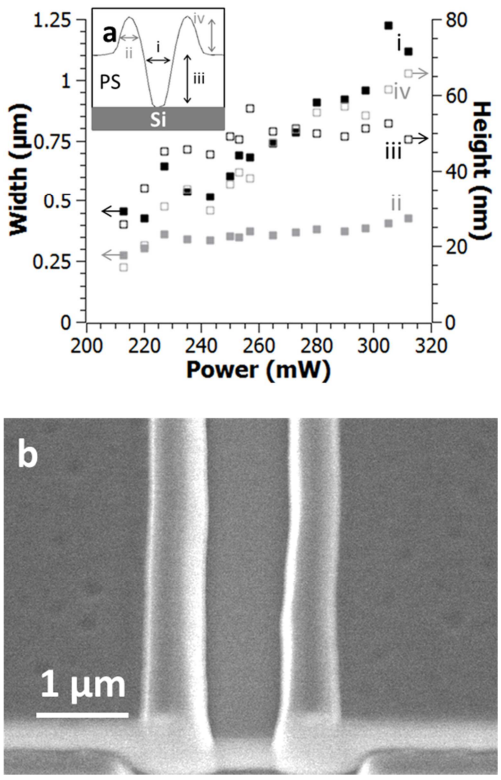

Figure 3-2: (a) AFM analysis of isolated dewetted lines written at different powers and 100 µm/s write speed. The scan of a single line is shown in the inset (with materials schematic added). The extracted features are as indicated in the inset: (i) trench FWHM (black, filled symbols), (ii) ridge FWHM (grey, filled), (iii) trench depth (black, empty), and (iv) ridge height (grey, empty). (b) Tilted SEM image of FIB section of a transferred FLaSk patterned at 310 mW, 100 µm/s.

a trench formed by dewetting and (2) the accompanying ridges due to the displacement of material from the trench. As can be seen, with increasing power the trench width (measured as the FWHM of the bottom of the trench to the top of the ridge) increases roughly linearly from 0.4 to ~1.2 µm, while the depth (defined from the film surface) increases rapidly until it asymptotes at the full thickness (here ~50 nm at ~230 mW). Ridge height grows linearly, even past the asymptotic limit of the trench depth, due to the fact that the ridge width (defined as the FWHM from the surface of the film) remains relatively stable compared to the trench width, only increasing from ~0.3 µm to ~0.45 µm. This difference in feature size may be explained due to the fact that, while the trench includes increasingly more material that is above the flow temperature of the PS, the ridge is always in a low mobility region of the film, leading to a buildup. One significant feature of both the lines and ridges is that they are below both the width of the optical spot (FWHM for ideal NA=0.4 focus is 0.66 µm) and the thermal spot size. By the metric of either feature, the apparently linear feature increase of the single FLaSk lines still manages to possess regions of sub-optical limit resolution.

The ultimate goal for most lithographic processes is pattern transfer into the underlying substrate. Therefore, pattern transfer into silicon and FIB cross-sectioning was approached to demonstrate the capabilities for the technique (Figure 3-2b). It can be seen that at this power and focus the individual lines consist of ~0.85 μm width trenches bounded by ~0.5 μm rectangular buildups, with trench depth of ~0.78 μm. The accessible depth of patterning can be increased with the selectivity of the utilized polymer, but indicates that submicron pattern transfer is even possible with a conventional polymer (like PS).

The line width varied from exposure to exposure. For the results shown here, the range of trench sizes observed was 0.6~0.9 μm. While there was a dependence on write power, it appeared to depend to a greater extent on the focus and local film thickness. For a given environment and focus, a higher write power did lead to thicker lines and deeper trenches/larger ridges (see Figure 3-2a). Despite this, the best characterization at this time, until a better set of film thickness, power, and focus dependencies are identified, appears to be the width of an isolated feature.

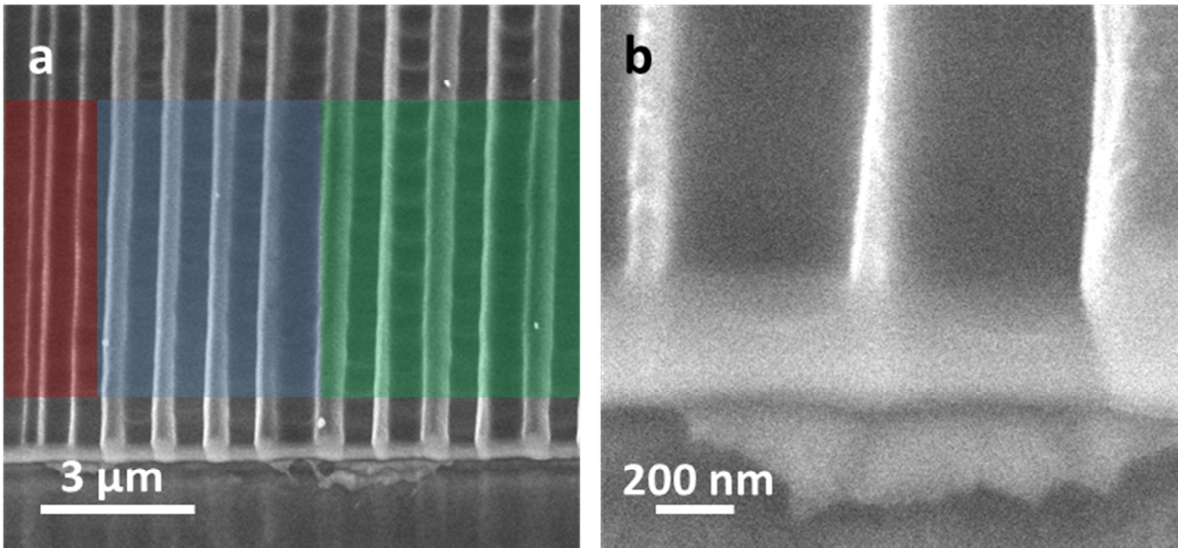

Figure 3-3: Pattern transferred dewetting lines written at 260 mW, 100 µm/s. Three sets of lines patterned with different periodicities: 1 µm (green), 0.5 µm (blue), and 0.25 µm (red). Three distinct behaviors can be observed. (1) At 1 µm, there are two different line spacings (~1, ~1.1 µm) and widths (~0.3 µm, ~0.5 µm). (2) At 0.5 nm, a single line spacing (~1 µm) and width (~0.4 µm) is adopted, with not all lines being patterned to make up for the doubling of period. (3) Finally, at 250 nm, smaller lines are observed, with the only successful pattern transfer from this particular line set shown in (b). (b) Patterned transferred line from 0.25 nm set (though at the transition to 0.5 nm period), width is observed ~80 nm and tilt corrected height of ~0.16 µm.

An interesting distinction between dewetting and ablation is the *displacement* of material as opposed to its complete removal. Due to this, the patterning behavior of lines as they approached one another was of considerable interest. Figure 3-3a shows the evolution of the pattern-transferred lines with three pattern periodicities (1 µm, 0.5 µm, and 0.25 µm) written at 260 mW, 100 µm/s (leading to ~0.9 µm ridge-to-ridge features). As the lines approach one another they go through a transition from the isolated line behavior to where the ridges start decreasing in size. After this point, the ridges become the relevant feature as opposed to the trenches as they are now the high resolution feature. At a certain spacing, a bifurcation of the pattern occurs where the ridges adopt two line-to-line spacings (in Figure 3-3 for 1 µm spacing, ~1 µm and ~1.1 µm) and two line widths (in Figure 3-3, ~0.5 µm and ~0.3 µm). At 0.5 µm spacing, another regime can be seen where the ridges adopt a single line width (~0.4 µm) and spacing (~1 µm). The latter is surprisingly disparate from the patterning periodicity, and also (necessarily) results in

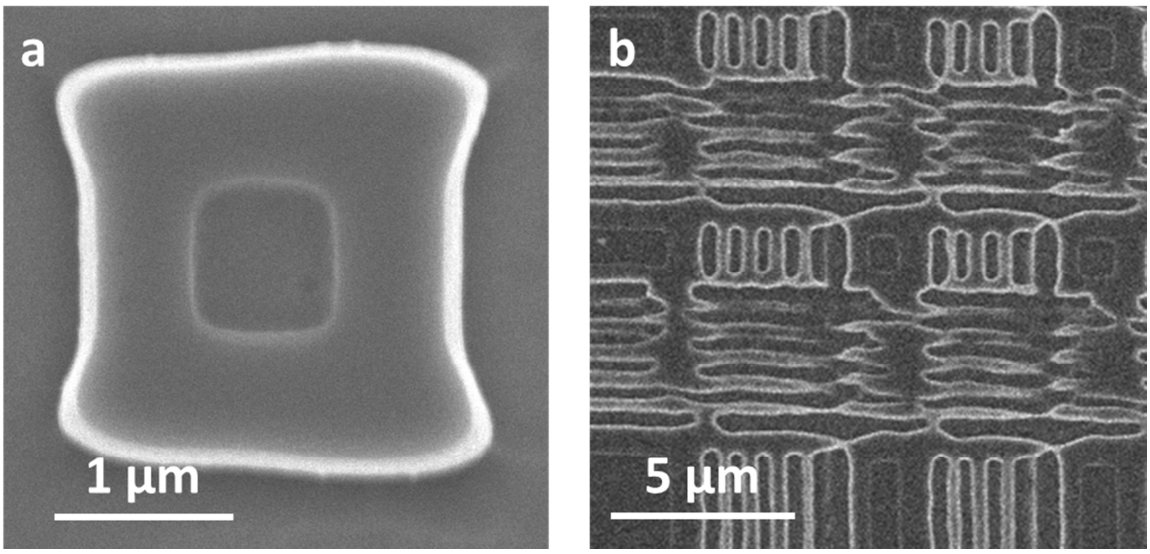

Figure 3-4: Images of etched 2D patterns generated by intersecting dewetted lines. (a) an isolated square generated by the crossing of four lines. Center divit is the original film thickness surrounded by ridges of the lines. Effects of the second set (horizontal) sealing the lines created by the first can be easily seen. (b) Sets of intersecting dewetted lines with the horizontal (patterned second) overwrighting and sealing the first patterned lines, resulting in complex dewetting patterns.

only four lines despite the write consisting of eight. This indicates that the mechanism that leads to their formation is more complex than the simple linear combinations of multiple line patterns. At 0.25 µm, even more unusual behavior is observed – only three of eight lines were patterned at extremely small and inconsistent spacing (though this may have to do with the proximity to the 0.5 µm grating and the few repeats of the total grating). While of the three lines in Figure 3-3, only one acted as an effective etch mask (Figure 3-3b), it did so with a line width of ~80 nm and an aspect ratio of ~2.

One possible unfortunate consequence of the displacement mechanism is interference between any crossing lines. For example, Figure 3-4a shows a square pattern defined between two sets of vertical and horizontal lines with the vertical patterned first. The portion of the vertical line that was crossed by the horizontal line can be seen to partially close because of the induced dewetting from the second, horizontal line. This can also be seen for multiple line patterns where the second set of lines will undo the first and result in complex disordered patterns (Figure 3-4b). While it is possible that these could be rendered

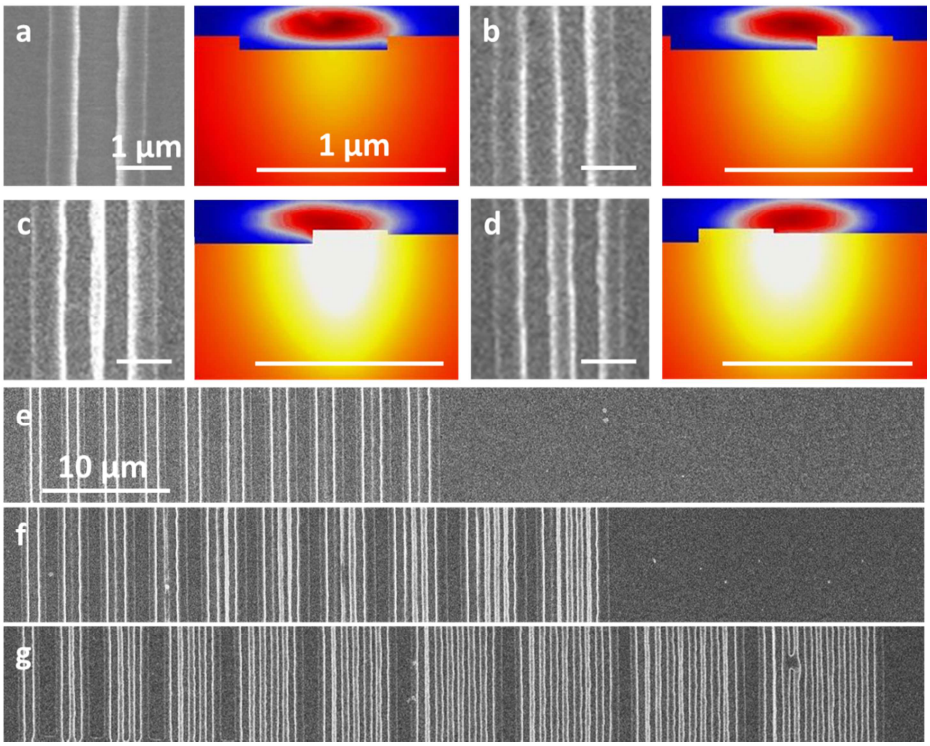

Figure 3-5: Analysis of sequential line patterning at 305 mW, 100 µm/s. (a-d) Second line patterns and associated 3D simulations for (a) 0.1 µm, (b) 0.3 µm, (c) 0.5 µm, and (d) 0.9 µm. It can be seen that small line features are best formed when the ridge amplifies the edge of the patterned line only. (e-f) Ten line evolutions, with a single line on the far left and ten lines at the far right, for (b) 0.1 µm, (c) 0.4 µm, and (d) 0.9 µm. Three different patterning regimes are evinced: the building up of a single, very narrow line (0.1 µm), the complex evolution of a regular grating (0.4 µm, showing the following number of line features: 0, 1, 1, 1, 2, 3, 3, 3, 4, 5), and the simple formation of a regular grating (0.9 µm).

useful by a more complicated patterning design, currently, it serves as a limitation on the sorts of features which can be patterned by FLaSk dewetting.

3.3.3. **Patterning of multiple adjacent lines**

While there are highly dynamic processes involved, further FEM simulation can elucidate some of these behaviors. To accomplish this, static simulations were performed using the observed cross-section ratios for the second-patterned line. The critical factor is the effect of film thickness on the optical absorption of the substrate. As shown in Figure 3-1a, thicker portions of the film lead to higher optical

absorption, while thinner films lead to lower optical absorption. The net result is that a line patterned with a majority of the focal intensity within a trench will have a lower peak temperature. Alternatively, when some portion of the intensity is within the ridge, a hotspot can develop with a size independent from the actual beam spot, but rather depending on the overlap. Based on this, several distinct regimes of behavior can occur. This can be seen clearly in the second line patterned, which is shown for several line-to-line spacings in Figure 3-5 (a-d). As the beam spot approaches the ridge, at first (0-0.1 μm) the temperature is insufficient to generate any line formation. Then, (0.2 μm-0.4 μm) a reduced spot due to overlap and ARC effect causes the formation of very high resolution lines. Once the overlap becomes great enough (0.5 μm-0.7 μm), the spot fills the ridge leading to larger lines and complete dewetting of the ridge (allowing for some of the uniform periodicities observed at these spacings). Finally (>0.8 μm), the spot reaches the other side of the ridge and causes the formation of an entirely new line. The formation of these second lines does not necessarily leave the same spacing between the patterned region and the ridge as the line that formed it, leading to the potential for each of the successive lines to display a different behavior, such as the bifurcation observed in Figure 3-3a. Figure 3-5e-g shows ten lines patterned at different spacings. In the case of the 0.1 μm spacing (Figure 3-5e), each successive line slowly approaches the ridge, leading to gradual buildup of a single line. It is interesting to note that, since the small feature does not cause a significant ARC effect, it remains cold and the dewetted portion of the ridge, pushed down the gradient, is pulled to build up the existing feature rather than starting a new feature at a distance commensurate to the second line (~0.4 μm) from the ridge. The 0.4 μm set (Figure 3-5f), leads to an interesting (apparently cycling) behavior of (i) three successive lines building up a single ridge, (ii) the fourth line creating a fully formed ridge of a similar size, and (iii) the fifth line starting the small nucleus for the next two lines. The net result is oddly a relatively uniform grating, though the first patterned feature is always smaller, as it takes a few lines to establish the pattern that will dominate. Finally, the 0.9 μm set (Figure 3-5g) shows an instance where the grating forms regularly with each successive line.

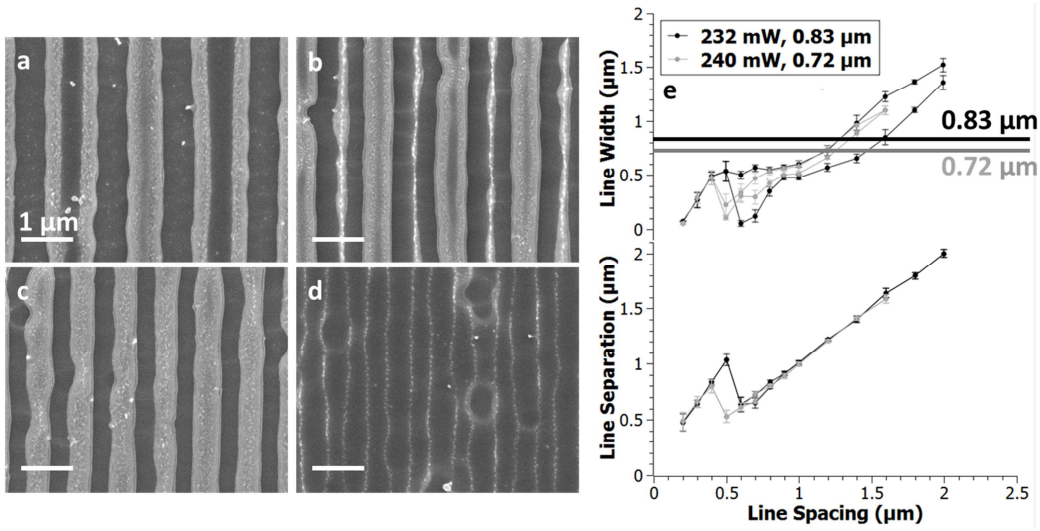

Figure 3-6: Grating patterns written at 232 mW, 100 µm/s at written line spacings of (a) 1.4 µm, (b) 0.7 µm, (c) 0.4 µm, and (d) 0.2 µm, along with aggregated apparent line width and separation (e, black). Also shown in (e, grey) is the aggregated data for a set of lines with a smaller isolated feature size (written at 240 mW, 100 µm/s). The ridge-center-to-ridge-center width of the isolated line (0.83 µm and 0.72 µm respectively) are marked by the horizontal black and grey lines.

Having now developed some intuition for the patterning mechanisms, it is useful to approach a systematic set of patterns. Figure 3-6a-d shows several characteristic 1D grating patterns. As the periodicity changes, several regimes of patterning occur. This is shown for two sets of gratings starting from different-sized single line patterns (0.83 µm in the black trace corresponding to the shown SEMs in Figure 3-6a-d and 0.72 µm for the grey trace). First, (not shown) the ridge spacing will be equal to the separation minus the line width when the lines are far enough away not to interact. Then (~2 µm), a bifurcated line width regime (shown for 1.4 µm line-to-line spacing in Figure 3-6a) will begin with alternating large and small ridges as discussed above and spacings equal to exactly the write spacing, since every line written is a line patterned. Once the widths of these features approach the isolated feature size, their width difference can be seen to narrow, as each patterned line finds itself in a very similar environment as the one prior due to the filling of the ridge observed in Figure 3-5c. With decreasing separation, the bifurcation begins to increase (and some spacing bifurcation is also observed) as the overlap effect shown in Figure 3-5b begins to occur until high resolution (down to ~70 nm) features

begin to occur for the small line (Figure 3-6b for 0.7 μm, possessing ~0.1 μm features). Finally, the smaller feature disappears entirely (~0.5 μm writing spacing), thus leading to an increase in the feature-to-feature distance. After this transition, multiple lines will pattern a single feature in a relatively uniform fashion (Figure 3-6c for 0.4 μm), but this behavior will only be stable down to a certain point, shown with ~70 nm features for 0.2 μm writing spacing in Figure 3-6d.

A few interesting observations: first, it can be noted that more than two line spacings are never (or rarely, considering all samples fabricated) observed, at least at a noticeable enough difference to exceed the displayed error bars. Rather, there seem to always be either alternating line sizes (and spacings) or a single dominate size and spacing. Why this is the case is not entirely clear, but it is definitely convenient for the purposes of a lithographic technique. One unfortunate result for the small spacings is a side effect of multiple lines patterning the same feature, which is sensitive to process fluctuations. This is especially evidenced in Figure 3-6c,d. The result is line 'wiggling' and small laser induced damage (LID) effects when the illuminating beam encounters small density or thickness variations or impurities. This will have to be addressed to be able to get these high resolution features with acceptable quality. That being said, the grating structures fabricated at higher spacings are still below the optical limit (~1 μm for these optics) and are of a reasonable quality. In comparing the grey and black traces in Figure 3-6e, it can be seen that the transition to single low periodicity occurs later in the smaller feature patterns (grey) as may be expected, but despite this, the trend for both the feature size and spacing appears to follow the same linear traces. The slopes of these lines are ~1.7 for the line spacing and ~2.0 for the line width. Both observations are unexpected considering that, as can be seen in Figure 3-5f, lines may be formed from different numbers of exposures. This is a behavior that could be expected to greatly depend on the size of the optical spot. Rather, the suggestion of these observations is that there is a fundamental shape and size that is adopted for a given film thickness, polymer, and written line-to-line spacing. The last parameter, being a property of the experiment, is very surprising, and will definitely need to be investigated further

both through 3D simulations of the line evolutions and experiments with different spot sizes to see if this trend holds for larger variations.

3.4. *Conclusions*

In this chapter, thermocapillary dewetting of a simple polymer system (PS) was demonstrated as a positive tone direct write process that can be used effectively for pattern transfer of submicron lines without the necessity of a development step. While this is already a useful technique, the patterning capability becomes even greater as the lines are brought together. Due to the fact that the driving force for dewetting and pattern formation (proportional to thermal gradients) is a result of a combination of the optical exposure and the thermal properties of (primarily) the absorptive substrate, consecutively patterned lines near to one another possess anti-reflection effects leading to subwavelength thermal profiles. In this manner of decoupling the optical resolution from the resultant thermal pattern, isolated features down to <100 nm or grating patterns with near constant periodicity near the optical limit (0.5~1 μm) and line widths still below the optical limit either in a large-small alternating pair or constant size may be generated. The resultant polymer film height variation features are still robust enough for pattern transfer and therefore represent a new method to create high resolution features in a three step (resist deposition, laser patterning, and etching) process – eliminating the necessity for wet chemical development from the lithographic process. To improve the resolution and consistency of this method, the current NA (0.4) could be increased. In addition, different thin film materials possessing either more beneficial properties for patterning or pattern transfer could be approached. In the former regard, it is not clear *a priori* what properties will lead to superior response, but it is likely that increasing the softening temperature and decreasing the mobility (such as with higher T_g or molecular weight polymers) could achieve a smaller extent of isolated dewetted features. Finally, it may be possible to employ water or alcohol soluble polymers, to completely remove the need for hazardous chemicals from the lithographic process.

4. Focused Laser Spike Annealing of Block Copolymer Thin Films

4.1. *Introduction*

As introduced in 1.2.6, BCP thin films have shown much potential as a pattern transfer medium for ultra-fine (<20nm) features. Thin films of microphase-separating BCPs are commonly self-assembled through the use of annealing processes which allows the kinetically trapped, as-cast polymer microdomain structure to attain the equilibrium morphology via diffusion by increasing temperature to overcome the energetic barrier for reptation.[103] As an alternative, Solvent vapor annealing involves placing the BCP in a vapor environment where solvent molecules can diffuse into the film and plasticize the polymer, decreasing the glass transition temperature and improving the mobility of the BCPs for self-assembly at ambient temperatures.[167] Due to limited morphological control of thermal or solvent annealing, several techniques for the manipulation of BCP thin film ordering and morphology have been developed, with the most common being chemical[123, 168] or graphoepitaxy.[126, 169-172] In general, these methods result in thin films possessing the same equilibrium phase that would be present in the BCP film without epitaxy, albeit with enhanced order and control of defects and relative domain orientation. Techniques for the generation of BCP films containing regions of different microdomain types (e.g. coexisting regions of spheres and cylinders) have also been investigated. These methods involve trapping the BCP in a first morphology determined by one annealing process, then immobilizing the chains in regions of the film by crosslinking to fix one of the two phases. Both e-beam[169, 173] or UV[173] exposure can be used to fix the initial microdomain structure, then a further annealing step with a different (or no) solvent can access a second morphology in the un-crosslinked regions. In a recent approach the second solvent annealing step is performed locally with a DW solvent vapor nozzle without the need for crosslinking.[134] While these techniques enable feature control (using e-beam crosslinking) down to the lengthscale of a single microdomain, most require the inclusion of crosslinkable block chemistry and possibly an additional crosslinking initiator and do not necessarily provide control over the in-plane

orientation that may be desirable for pattern transfer applications. In order to develop a technique that could potentially be used for many BCP systems and enable both localized phase and orientational control without necessitating additional modification, the FLaSk annealing described in the previous section was approached. In Chapter 3 it was revealed that application of a focused heat source to a polymer thin film universally led to dewetting at some threshold unless LID occurred first. Possessing similarly extreme thermal conditions, the kinetic regime just before dewetting was investigated for zone annealing of BCP thin films. This was attempted for a PS-PDMS BCP and further enhanced by incorporation of solvent vapor.

As discussed in Chapter 3, LSA has been used for BCP microphase separation.[152] For BCP systems, the first demonstration of LSA was performed in 2007 and utilized a high power (on the order of a Watt), ms pulsed CO_2 laser exposure, which could initiate microphase separation for ~1 min total exposures, but did not demonstrate good domain ordering and often resulted in considerable polymer damage including burning and void formation, ostensibly due to intrinsic optical absorption and degradation of polymer.[152]

In considering LSA of a thin BCP film, there are obvious similarities to zone annealing, a technique utilized on both thin and thick films of BCP for achieving simultaneous annealing and alignment. In zone annealing, a BCP film is moved over an induced thermal gradient resulting in ordering along the direction of the motion. One important distinction between various zone annealing techniques is whether they are hot (above the order-disorder transition (ODT))[131, 174] or cold (below the ODT)[130, 175] at their maximum temperature. In both cases, microdomain ordering and alignment happens primarily in the regions of thermal gradient: for hot zone annealing, ordering occurs as the BCP passes back through its ODT, while in cold zone annealing it was shown that a majority of ordering occurs in the cold-to-hot portion of the gradient and was relatively independent of subsequent baking, indicating the importance of a gradient for driving the reordering of the domains.[175] A combined approach of cold zone annealing with thermal expansion-induced surface

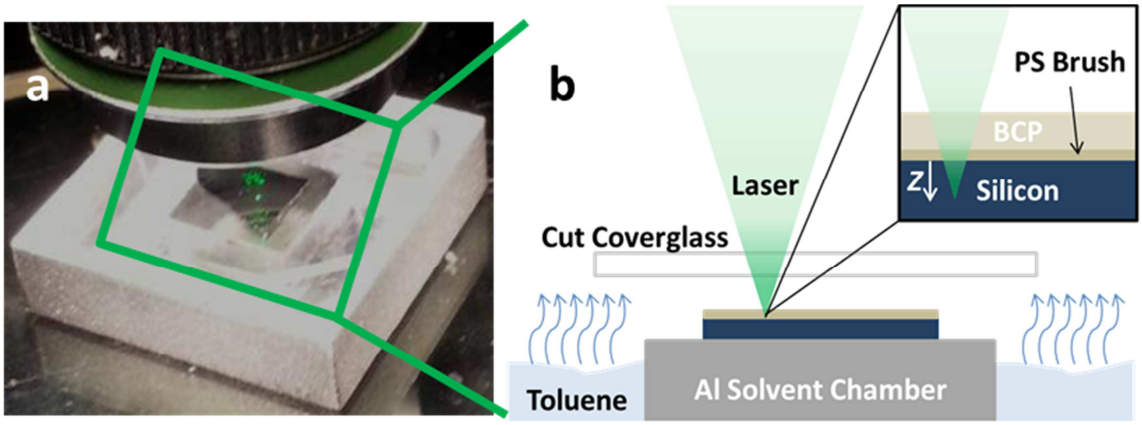

Figure 4-1: Photograph (a) and schematic (b) of FLaSk zone annealing solvent setup. The solvent chamber (grey box in (a)) possesses a platform surrounded by a solvent reservoir. The sample is placed on the platform underneath a cut coverglass. The surrounding solvent reservoir is filled with solvent (here, toluene) and slowly evaporates around a cut coverglass to generate a steady-state partial pressure of solvent. For the patterning, the BCP is spun on top of a PS brush, and the laser is focused through the glass with spot size controlled by the axial focal position (*Z*).

shear by a top PDMS film resulted in exceptionally high order and alignment for annealing rates of up to 200 μm/s (travelling through a 0.045 K/μm, 9 K/s gradient) and film thicknesses from a single layer of microdomains up to 1 μm.[133] Additionally, it was shown that without the presence of the PDMS, thermal gradients of a similar magnitude could lead to vertical alignment with respect to the substrate,[176] which was most recently used to accomplish roll-to-roll perpendicular alignment of BCP domains.[177]

Much as with the dewetting work, FLaSk zone annealing is similar to conventional LSA in that it utilizes the quasi 2D absorption of the substrate to generate heat (Figure 4-1), but still allows for LSA on a region of polymer similar in size to confining geometries utilized in graphoepitaxy, creating an effective instantaneous confinement by the surrounding unheated polymer which possesses a much lower mobility. The one key difference from the dewetting work (in Chapter 3) is the incorporation of a partial pressure of solvent (here, toluene) by use of an aluminium reservoir that forms a steady-state solvent atmosphere by evaporation around a cut coverglass. The coverglass focuses the high

solvent atmosphere above the sample and also allows for (corrected) FLaSk annealing. Once again, the use of circularly polarized light prevents any polarization-dependent absorption and, additionally, polarization-based BCP alignment effects.

In this study, we employed a 31 kg/mol-11 kg/mol PS-PDMS BCP trapped in a metastable state consisting of spherical micelles after spin-coating and utilize the FLaSk anneal to transform to the equilibrium phase (i.e. cylindrical PDMS domains). From a zone anneal standpoint, PS-PDMS is strongly segregating (room temperature $\chi N \approx 95$) and the ODT (~3000 ºC) should not occur before significant polymer degradation. PS-PDMS ODT was only recently observed for the first time by our group in ultrahigh energy impact[178], where adiabatic compression of Mach 1.5 projectiles resulted in massive, nearly-instantaneous adiabatic heating. For these reasons, FLaSk for this particular BCP may be classified as a cold zone annealing with thermal gradients orders of magnitude greater than those previously explored.

4.2. *Mechanism of FLaSk zone annealing of BCP*

As a tool to investigate the thermal mechanisms of FLaSk of BCP, FEM simulations were used to estimate the temperatures and gradients that the polymer would experience during the FLaSk anneal. The thermal profile was analytically modeled as a Gaussian source (NA=0.4) and the optical absorption and heating that would be expected to occur. For materials properties, temperature-dependent values for silicon substrate were utilized for the thermal conductivity, heat capacity, and density.[164] The optical absorption also displays an exponential dependence on temperature, so it was simulated using a previously derived empirical model for near-intrinsic silicon excited with 532 nm light.[165] Finally, the absorbed power by the substrate was determined by measuring the damage threshold, which corresponds to a peak temperature of ~1400 ºC where the silicon surface melts.[166] Utilizing a steady state approximation with these empirical parameters, the simulated peak temperatures and gradients as a function of measured laser power (before objective and coverglass reflection) beam focused on the

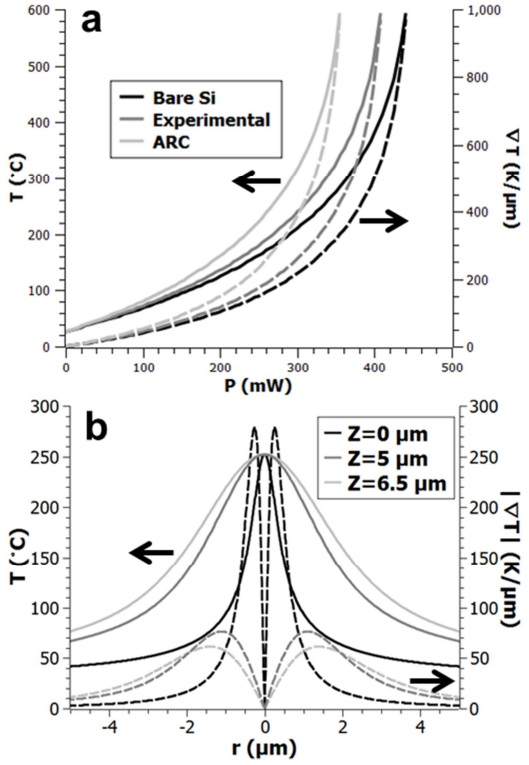

Figure 4-2: (a) FEM simulation of the peak temperature and spatial thermal gradient experienced by a central point along a FLaSk write path focused in the plane of the substrate surface for bare silicon (black), experimental BCP (dark grey) and the high limit of the full BCP film acting as an ARC (grey). (b) Temperature (solid) and gradient-magnitude (dashed) profiles for two differing focus laser spots from the surface of the sample. Here the BCP thickness is considered negligible for the purpose of defining focus, which is also considered as independent of the silicon index (*i.e.* free space focal translation).

surface are shown in Figure 4-2a for three scenarios. These represent the temperatures determined for a bare wafer (black trace, 17.5% optical energy absorption), a calculated value for the bare wafer with a 50 nm polymer antireflection coating of average index (1.55) corresponding to the BCP (grey, possessing a lower reflectivity and higher absorption of 20.8%), and the calculated curve using the observed damage threshold during the actual annealing experiments (dark grey, 18.9% absorption). Due to the fact that the patterned lines are observed to thin (discussed below), we believe that, even at constant power, the temperature progresses from the light grey trace to the black as the film thins, resulting in a temperature near the dark grey trace. Under the hypothesis of the thermal gradient being the key factor, it is important that for the laser powers utilized (300-350 mW, corresponding to an average temperature of approximately 200~300 ºC), gradients on the order of 100~750 K/μm are created. The temporal gradient can be approximately determined by the spatial gradient multiplied by the write speed, corresponding to temporal thermal gradients on the order of 3,000~75,000 K/s depending on write speed (30-100 μm/s). These are two to four *orders of magnitude* greater than

those used in the previous cold zone annealing studies.[130, 133, 175-177] The spatial temperature and gradient profiles are shown in Figure 4-2b for a peak BCP film temperature of 250 ºC demonstrating the tunability by changing the focus (Z=0, 5, and 6.5 µm offsets) to control the effective spot size from 0.5 to 3 µm, here defined as the distance between peak gradients.

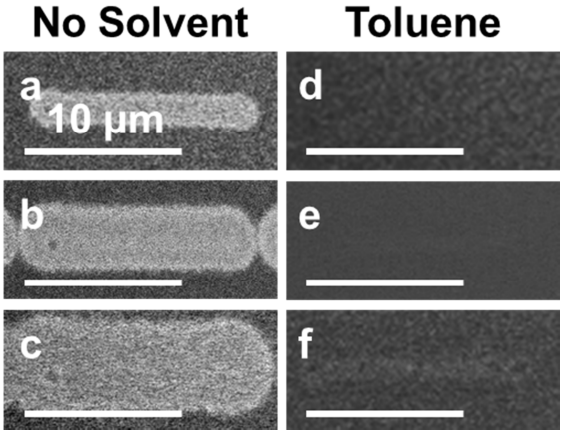

Figure 4-3: Characteristic lines patterned with focus at 0 (a,b), 5 (c,d), and 6.5 (e,f) µm below the surface of the substrate without (a, c, e) and with (b, d, f) toluene vapor. The contrast due to film thinning is present to a much larger extent in the lines patterned without solvent indicating a larger area of heated polymer likely due to the lack of evaporative cooling.

To create an initial metastable state, the PS-PDMS BCP was spun from a PGMEA solvent that was preferential for PS leading to a film consisting of spherical micelles with the minority PDMS blocks at the core, with PS-air and PS-PS-brush contact surfaces. The micelles pack into a monolayer hexagonal array, as opposed to the equilibrium cylindrical phase, without a PDMS surface layer which typically forms in annealed PS-PDMS films due to the lower surface energy of PDMS. Subsequent morphological changes during FLaSk annealing are therefore not affected by any directional bias from preexisting cylindrical microdomains. Films were swollen to 140% of their as-cast thickness using toluene vapor during the writing process (as measured by reflectometry) which was attributed to a vapor pressure of toluene of approximately 19 Torr (~85% of the saturation vapor pressure).[179] While this increased the mobility of the film, it was insufficient to allow changes in the morphology of spherical micelles in the absence of FLaSk heating during the timescale of a given experiment. At these molecular weights, the individual chains are likely not highly entangled (M_e=~13 kg/mol and ~12 kg/mol for PS and PDMS respectively).[180] We expect that the major contribution of the

solvent, beyond increasing mobility of the PS chains, was to induce evaporative cooling during the onset of annealing leading to a sharper thermal gradient; this interpretation was supported by observations of the electron contrast in the surrounding heated region. Figure 4-3 shows a series of single-pass lines written at different focuses with respect to the plane of the substrate for films with and without solvent vapor. Without solvent, the bright region in the SEM images surrounding a given patterned line is ~5x the apparent annealed width, while little or no similar effect is observed in the presence of solvent, indicating a reduction in the extent of the thermal effect. As the samples are swollen with solvent rather than immersed, it can be expected that the solvent will be completely removed at the highest-temperature portion of the spike, thus allowing for the peak annealing temperature to be reached and resulting in a sharpened gradient. Due to the complexity of the combined solvent and thermal anneal with rapid removal of solvent, we leave more predictive simulations for future work.

4.3. *Experimental realization of FLaSk zone annealing*

4.3.1. **Experimental parameters**

Lightly doped p-type silicon substrates ([100] orientation, 10 Ω-cm) were coated with hydroxyl terminated polystyrene (M_n = 3000 kg/mol, PDI= 1.06, PolymerSource P2969-SOH) and heated to 170 °C for 16 hours in a vacuum oven. The wafers were then rinsed with toluene to remove the unreacted brush layers after which BCP films of PS-PDMS (31 kg/mol-11 kg/mol, PolymerSource) were spun from 1.8 wt% solutions in PGMEA to prepare films of 49-55 nm thickness. Patterning was performed with system L-532CW-A_0.4-V through the solvent chamber described above.

4.3.2. **Linear patterns from FLaSk zone annealing**

Images of selected lines patterned by the 532 nm laser are shown along with the 2D Fourier transforms of the laser annealed region in Figure 4-4a-d. Despite the very short anneal times, formation of cylindrical microdomains occurred in which the cylinders were preferentially aligned along the writing direction, as can be further seen by the asymmetry in the Fourier transforms. Domain size in the annealed

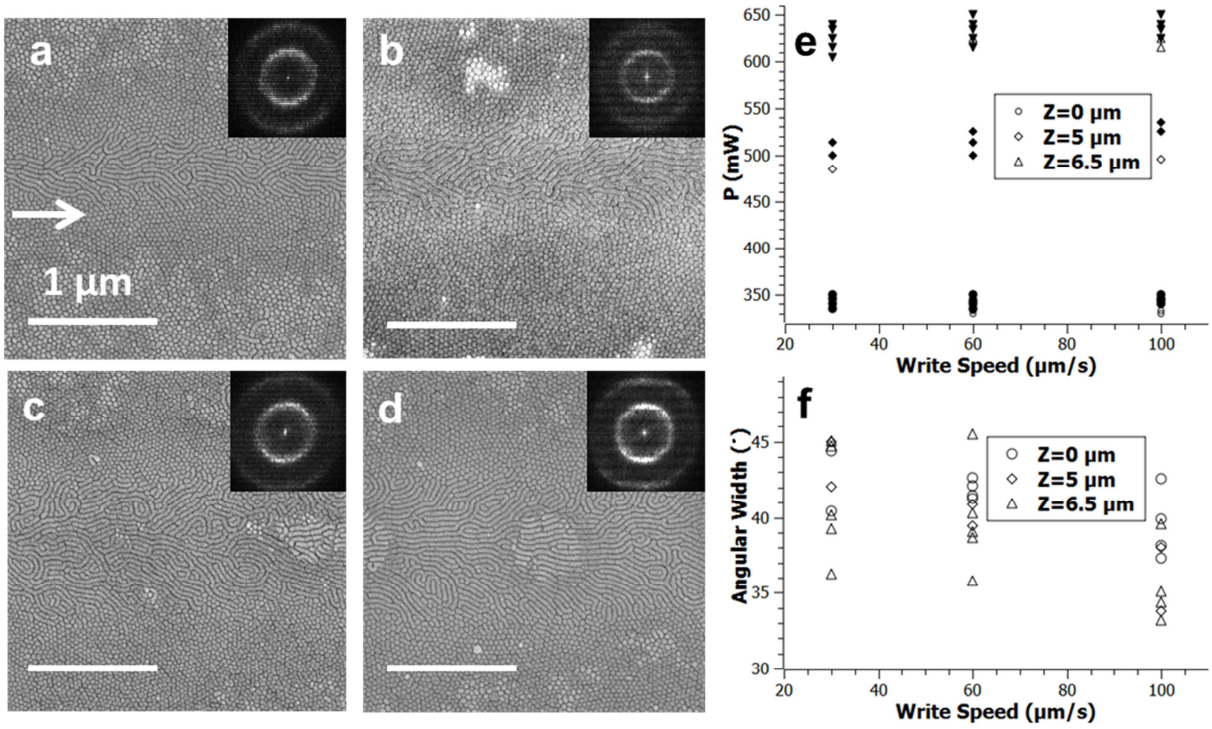

Figure 4-4: (a-d) Images of some characteristic FLaSk patterned lines. Horizontal lines are written with solvent annealing left-to-right for different speeds and powers at three focuses: 335 mW, 60 µm/s (a) for focus at the substrate surface and 500 mW µm/s, 30 µm/s (b) for focus 5 µm in the surface, and 625 mW µm/s, 30 µm/s and 635 mW µm/s, 100 µm/s (b) for focus 6.5 µm in the surface. 2D Fourier transforms of the line regions (inset) confirm the preferential alignment. (e) Processing windows for cylinder annealing. Each symbol corresponds to a sample where the micelles are transformed into cylinders. For comparison, the samples processed without (empty) and with (filled) solvent are included. (f) Alignment, as defined by the angular width of the anisotropic 2D Fourier transform of the annealed regions for solvent annealed FLaSk samples.

region appears larger than the surrounding unannealed region due to relaxation of the kinetically-trapped, collapsed PDMS micelles (~35 nm center-to-center spacing) to the equilibrium domain spacing (~40 nm period). Linewidths, which could be controlled by adjusting the laser focus, exhibited sub-wavelength resolution due to the strong nonlinearity of this process – the in-focus patterned regions have typical linewidths between 0.3 and 0.5 µm, compared to the expected thermal spot size of 0.86 µm. The FLaSk-induced transformation only occurs for a specific processing window, illustrated in Figure 4-4e for

samples with and without solvent vapor. Only patterns where a majority of the expressed morphology was cylinders are plotted, excluding mixed-morphology lines.

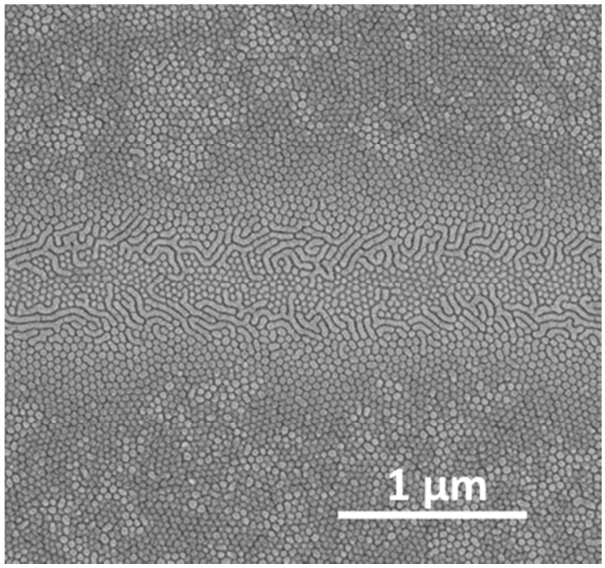

Figure 4-5: FLaSk line written at higher power (365 mW, 100 µm/s) between the dewetting regime and the ordering regime. In these conditions, it appears that the spherical micelles are locked in by the degradation or crosslinking of the PDMS.

When the power was too low, the spheres relaxed, but did not fully transform, as would be expected from the heat-quench mechanism; however, when the power was too high and the speed too slow, two distinct behaviors were observed. The first was a complete dewetting of BCP in the annealed region. This is an expected result since all of the lines thinned during the annealing, as expected from the effects discussed in Chapter 3. The second was the observation of spheres possessing the same dimension as the collapsed micelles in the as-cast film surrounded by cylinders, which indicates that the temperature was high enough that the PDMS fully degraded or crosslinked during the anneal (Figure 4-5). The effect of the solvent was to broaden the processing window, especially for deeper focuses (5 and 6.5 µm), by sharpening the effective gradient.

Cylinder alignment for the solvent annealed samples as determined by the localization of the first order Fourier transform peak of the annealed region was also analyzed (Figure 4-4f). From these single pass lines, the in plane orientation of cylinders within an angular distribution of 33° can be observed (shown in Figure 4-4b), with a general trend of increasing alignment with speed for a given writing power, and wider lines (created by focus within the substrate) possessing more overall better alignment. The latter observation is to be expected as a narrower line width (given a similar magnitude of the gradient) experiences greater confinement from the surrounding immobile polymer. Though the scan speed is

limited here to 100 μm/s due to the stage accuracy, ongoing experimentation has demonstrated ordering for speeds up to 1000 μm/s, so the limitations of the ordering rate (set by mass transport) have not yet been reached.

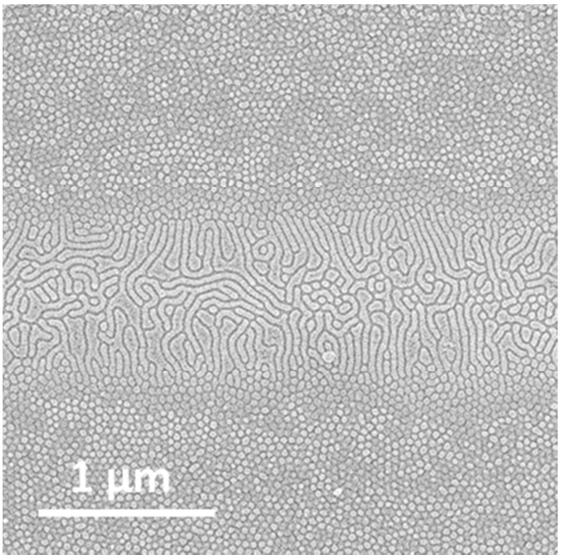

Figure 4-6: FLaSk line patterned at low power (285 mW) and speed (3 μm/s) of a surface-focused beam resulting in perpendicular BCP cylinder alignment.

Beyond the patterning capability, the results obtained by FLaSk zone anneal offer insight into the mechanisms of cold zone annealing. First, it is important to differentiate the ordering mechanism from other phenomena occurring during the anneal, such as dewetting (see discussion in Chapter 3). It is tempting to link these two behaviors, especially as the flow field generated by dewetting would be in the observed direction of alignment and could be analogous to similar elogational flow alignment obtained in electrospun BCP fibers.[58] Counter to this explanation is the lack of any observation of film thinning in previous cold zone annealing studies and the fact that dewetting often occurred *without* simultaneous alignment, such as in lines written at low (<30 μm/s) speed. Indeed, the only samples where significant regions of alignment purely perpendicular to the writing direction were observed were the highest focus lowest speed (3 μm/s) lines conducted at powers corresponding to typical thermal anneals (~225 ºC, Figure 4-6). These samples predominantly show horizontal alignment perpendicular to the write direction, as opposed to the parallel alignment dominant in the majority of lines. The faster lines do exhibit features suggestive of perpendicular alignment near the edges, where the cylinders cant outward, but always with a bias towards the direction of the writing.

These two observations support the magnitudes and sequence of the thermal gradients being the key factors in determining the alignment and also differentiate the perpendicular alignment from that predicted in existing models of moving mobility gradients.[181, 182] Rather, in the case of the slow speed

lines, the perpendicular alignment is initiated by the side gradients occurring just after the onset of parallel alignment, breaking up the order of the central cylinders. The second parallel gradient (i.e. cooling) did not initiate additional reordering, consistent with the experimental cold zone observations. The perpendicular alignment of slow lines has only been demonstrated for the tightest focus, and parallel alignment in slow these lines was not observed. This suggests that there is a threshold gradient that needs to be achieved in order to induce ordering and alignment. The presence of parallel alignment in fast lines further indicates that the threshold is related to the *temporal* gradient, which increasingly favors the writing direction as the speed increases. This explanation is supported by the trend in ordering discussed above.

What remains to be understood is the driving force for the gradient-mediated alignment. As mentioned earlier, it does not appear to be caused by mass transport, though this is presumably the limiting factor both at low speeds due to the dewetting and high speeds due to a kinetic limitation. One possible cause is film shear forces that also serve as the driving force for dewetting. Shear has been shown as an effective way to align BCP microdomains,[183, 184] including in recent cold zone studies.[133] Thermocapillary shear is generally expressed as[156, 157] $\tilde{\tau} \cdot \hat{n} = \nabla\gamma = (d\gamma/dT)\,\nabla T$, where τ is the shear stress, n the surface normal, and γ the surface tension. The surface tension almost always decreases with temperature leading to a net force down the thermal gradient. By approximating the surface as pure molten polystyrene ($d\gamma/dT$=0.07 mN/m·K)[185] stresses on the order of 10-100 kPa for the gradients utilized in this experiment are calculated. This is consistent with the high end of values for external shear stresses used in alignment studies.

It should be noted that the reframing of surface tension gradient in terms of the thermal gradient is not strictly applicable in the case of FLaSk experiments, where the thermal removal of solvent from the film also affects the spatial profile of the surface energy. This is a relatively unique mechanism to FLaSk as most solvent swelling gradients, such as the ones provided by rastered nozzle writing,[134] are relatively diffuse; however, in FLaSk the film can be expected to transition from swollen to dry over a similar

length scale as the thermal gradient (*i.e.* submicron). If we consider as a first approximation that, for PS, $\Delta\gamma$ at a peak temperature of 300 ºC is on the order of -γ (γ=31.0 mN/m),[185] then for the gradient of the solvent concentration to have a similar magnitude effect, it would have to alter the surface tension by a similar factor. Prior simulations have indicated that solvent vapor effects on surface tension can be expected to be of this magnitude and therefore, a "solvocapillary" shear force due to solvent gradient may be expected to be one additional contribution. The removal of solvent, however, can be expected to *increase* the surface tension, suggesting that the solvocapillary shear would be in the opposite direction of the thermocapillary shear. This view is over-simplistic, however, as the value of $d\gamma/dT$ can also be expected to be affected by the solvent (though to the author's knowledge this has not been studied), coupling these two effects. Were the incorporation of solvent to increase the negative magnitude of $d\gamma/dT$ (an intuitive result) the "conventional" thermocapillary stress would be enhanced, consistent with the observation of alignment only during the heating portion of the gradient, as the line immediately behind the moving laser spot would be expected to still be relatively dry from the laser heating.

There are likely also complex effects due to thermal expansion-induced strains within the polymer film itself. This is likely enhanced both due to constrained expansion along the gradient and mismatches between the constituent blocks. Thermal expansion gradients were proposed as a mechanism for the observed vertical alignment in samples submitted to relatively "sharp" conventional cold zone thermal gradients.[176] As vertical alignment was not observed in this experiment, despite the much sharper nature of the spatial and temporal gradient, it can be expected that these results represent a regime where the contributions of the thermocapillary driving force overcomes the driving forces for vertical alignment, possibly also reduced by the simultaneous contraction that occurs as the solvent is removed from the film.

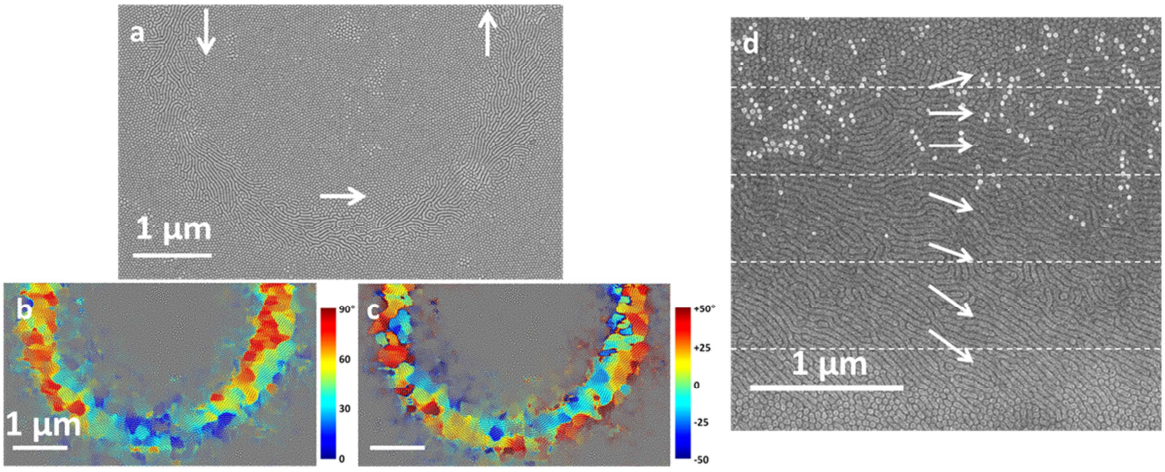

Figure 4-7: (a) Portion of a 5 µm diameter circular counter clockwise path written with a 545 mW beam moving at 60 µm/s focused 5 µm into the surface. Domain alignment can be observed to track the writing direction. This is further confirmed by alignment mapping (b), with much of the observed deviation correlating with the outward canting of boundary domains as can be seen when the alignment is compared to perfect circular orientation (c). (d) A multiline block (dashed lines) written with focus 6.5 µm in the substrate at 610 mW, 60 µm/s. The alignment gradually rotates due to the edge seeding, but results in higher order (solid arrows).

4.3.3. Advanced patterning by FLaSk zone annealing

The ability of this technique for making more complex patterns was demonstrated by annealing in a circular write path at a focus of Z=5 µm to determine if the orientation control could match a constant alteration in the writing direction. A SEM image of the highest curvature available (0.20 μm^{-1}) with two orientation mappings are shown in Figure 4-7a-c indicating that it is still possible to obtain orientational tracking of the moving beam even with line curvature, though the limits of this ability will still have to be tested beyond the limits of our patterning system. The first orientational map (Figure 4-7b) shows the evolution of the orientation angle on an absolute scale. While the orientation is certainly tracked, there are definitely deviations from perfect order visible. To examine this, the second map (Figure 4-7c) shows the orientation error (*i.e.* the divergence from perfect tracking). On the inside of the path, the map is bluer, representing an enhanced domain tilt inward, while the outside of the path shows an outward domain tilt.

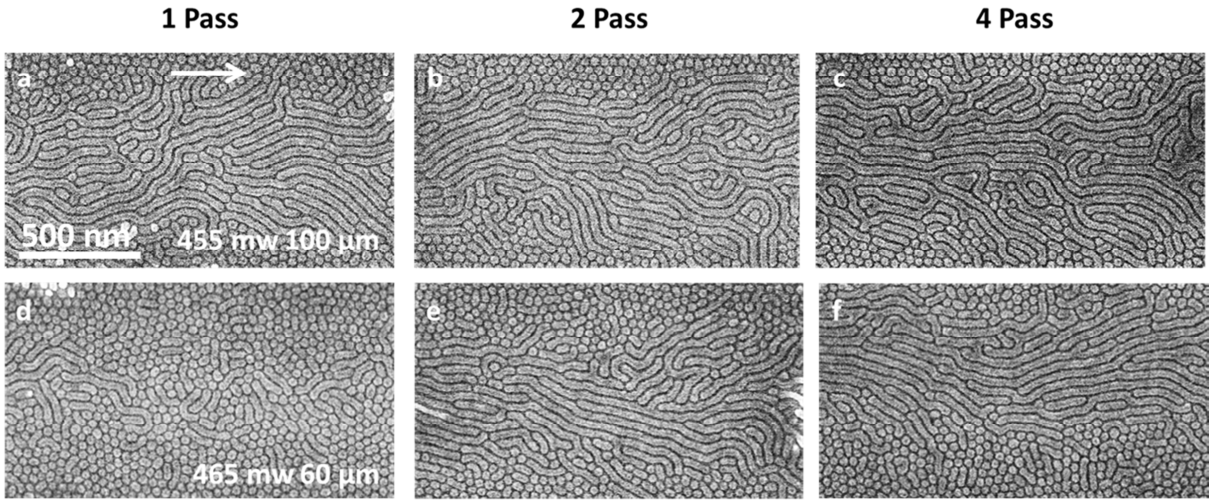

Figure 4-8: Multipass lines for the indicated writing conditions. When the first past is sufficient to generate cylinders (a-c) no additional ordering is observed; however, if the power is low enough that it takes multiple passes to initiate order, the final result appears to have larger cylindrical domains.

This is consistent with the effects of the outward canting of the cylinders due to the moving side gradients discussed above. This may be correctable by, for example, using a focal spot with an elliptical point spread function. The purposefully asymmetric thermal gradients would be expected to increase the alignment bias along the short axis.

Four line blocks at a focus of Z=6.5 µm were also patterned to assess the performance of adjacent lines (a characteristic example is shown in Figure 4-7d). Even though tilted alignment was observed because of the outward cant of the edges, it was possible to obtain larger domains of patterning in this way. These regions were often of a higher overall order than the single lines, suggesting that the canted edges were acting as seeds for the subsequent patterning. Interestingly, a similar effect was not observed with multiple passes over the same line, possibly due to the kinetics for defect removal being much slower than those of cylinder formation. Nevertheless, lines formed through multiple passes where a single pass was not sufficient to fully initiate transformation were observed to qualitatively possess longer continuous single cylinder whenever formation did occur (Figure 4-8). This effect will have to be investigated further but, it is likely that the gradual formation of smaller, aligned pre-cylindrical domains

can act (once again) as seeds for the subsequent patterning, serving to reorient the previously present spherical micelles in such a way as to more easily form continuous domains.

4.4. *Conclusions*

By an application of a FLaSk zone annealing we have demonstrated a method for driving transformation of a metastable BCP thin film to its equilibrium microdomain morphology. This is accomplished with a subsecond thermal anneal possessing thermal gradients on the order of 100~750 K/μm (3,000~75,000 K/s), which additionally leads to alignment of the generated cylinders along the writing direction analogous to larger scale cold zone annealing experiments. Based on the observations of both the lines patterned at high and low speeds, it appears that the temporal thermal gradient is the key driving force for the preferential alignment, with faster write speeds leading to a higher degree of orientational order, with the angular distribution of the cylindrical microdomain axes $\geq 33^{o}$. This annealing was performed at a previously unprecedented speed, occurring in 10-100 ms. Including solvent vapor in the sample chamber resulted in film swelling and subsequent evaporative cooling. To the best of our knowledge, this is the first application of incorporating solvent vapor in a direct write process. In this case, the effect of solvent was to increase mobility and increase the thermal and surface tension gradients, leading to an expanded processing window. Even with solvent, the processing window was only ~5% absolute power, corresponding to only tens of ^{o}C temperature differences. Despite this, the technique still represents a highly scalable method of controlling the in-plane alignment of BCP self-assembly and producing films that incorporate multiple morphologies by converting large-area cold zone annealing into submicron direct write. The parameter space of both FLaSk and conventional cold zone annealing has just begun to be explored, including the effects of using different BCP molecular weights, compositions, and volume fractions. Further, the use of solvent vapors with different block preference and boiling points represents a previously unconsidered (for zone annealing) parameter that can potentially lock greater ordering and alignment enhancement and even further degrees of freedom in morphology manipulation.

5. Focused Laser Spike Anneal of Chemically Amplified (Photo)Resists

5.1. *Introduction*

In keeping with the idea of drawing hierarchically patterned lines established in Chapter 4, it is tempting to consider the combination of 3DDW and IL. While optical IL possesses a larger minimum resolution than BCPs, the degree of uniformity and order of an IL pattern is much greater as it should possess few defects (related to dust rather than thermodynamics) and can have an area of uniform patterning commensurate to the size of uniform beam that can be generated. Further, the number of available patterns conveniently available to IL is much greater than those generated by self-assembly, being either a combination of Fourier terms (MBIL) or a projection into a higher dimensional space (PMIL). As discussed, 3DDW has been approached as a way to fill in 3D structures, such as those created by IL,[115] to generate "digitally" patterned spaces of either the 3D pattern or a completely filled (empty, in the case of positive tone) region. If it were possible to not only accomplish this, but also to add an additional degree of freedom, the capability of the combined technique would become much greater as it would add another dimension of control. For example, the simplest conception would be to incorporate both positive tone and negative tone functionality, which would make it possible to design where the pattern would be placed (by removing other areas) and also define filled defects such as waveguides, cavities, or supports. If, in addition to this ternary patterning, it were possible to completely access all (or many) of the midpoints by controlling the fill from empty to completely solid (likely with some minimum and maximum "grey" states as will be discussed), gradient fill structures with highly complex and detailed submotifs would become possible.

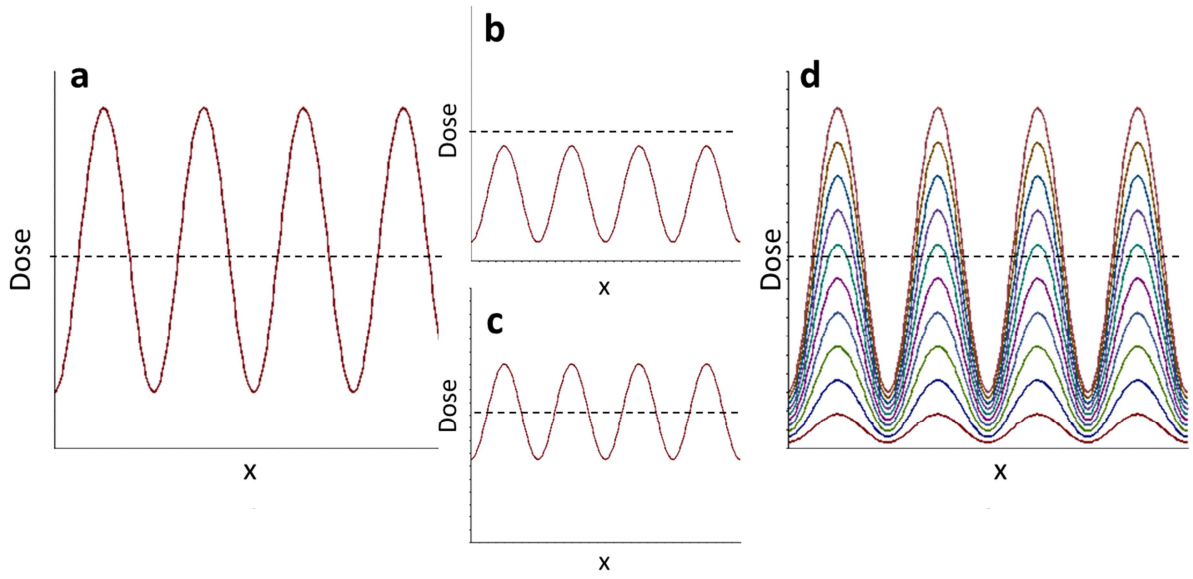

Figure 5-1: Simple schematic of the IL and hybrid process. (a) Structured exposure (and bake) where some portions of the pattern exceed a crosslinking threshold (dashed line) allowing for some contrast upon development. Hybrid technique with a secondary DW (or flood) exposure (b-c). Initial exposure and bake (b) is insufficient to reach threshold, but additional uniform exposure (c) lowers the overall contrast. (d) FLaSk-CAP hybrid technique where initial exposure is insufficient, but the laser baking crosses the threshold with tunable contrast and feature size.

In realizing this capability, one logical idea is using additive exposures. Specifically, to expose the resist lightly with IL, such that no region is exposed to a dose high enough to cross the patterning threshold and result in structuring upon development, and then to utilize the 3DDW to provide the dose to "push" the resist over the edge. This is shown schematically in Figure 5-1a. The issue with this approach can also be seen in the figure – contrast in IL patterning is a result of the absolute difference between the minimum and maximum exposure. Thus, underexposure results in a lower contrast (Figure 5-1b) and the linear addition of a 3DDW dose (Figure 5-1c) results in a very narrow range where the contrast is maintained and the crosslinking threshold is crossed. The ideal solution would be to maintain the same contrast and approach it gradually, as shown in Figure 5-1d. This is the idea behind FLaSk of CARs (here referred to as FLaSk-CAP where the "P" stands for photoresist). The final structuring of CARs is, to a degree, decoupled from the optical exposure by the need for a post-exposure bake. In general, excitation

of a CAR causes a photoacid/base generator (PAG) within the resist to produce a distribution of photoacid/base, which autocatalytically causes a deprotection of some chemical group in the structure of the resist polymer. This in turn leads to a change in solubility of the patterned resist by crosslinking, degradation, or change in functionality which leads to the patterning during development. This process is driven by a PEB anneal, generally by hotplate or oven. Conventional LSA was approached as a method to activate sub-millisecond crosslinking of a conventional CAR, thereby reducing the unwanted diffusion of photoacid into unexposed regions that occurs to a greater extent during a hotplate PEB.[153] This is possible because of differences in the activation energies of the two processes. The LSA of CARs was only reported for thin films of resist (~100 nm), patterned by conventional lithography. Nominal improvements in lithographic contrast were demonstrated, this study did show that rapid, high-temperature crosslinking of CARs on the order of 500 μs is possible. Furthermore, the quality of the resultant structures, as measured by both feature resolution and distortion due to PAG diffusion, was equal to or better than conventional post-baking.

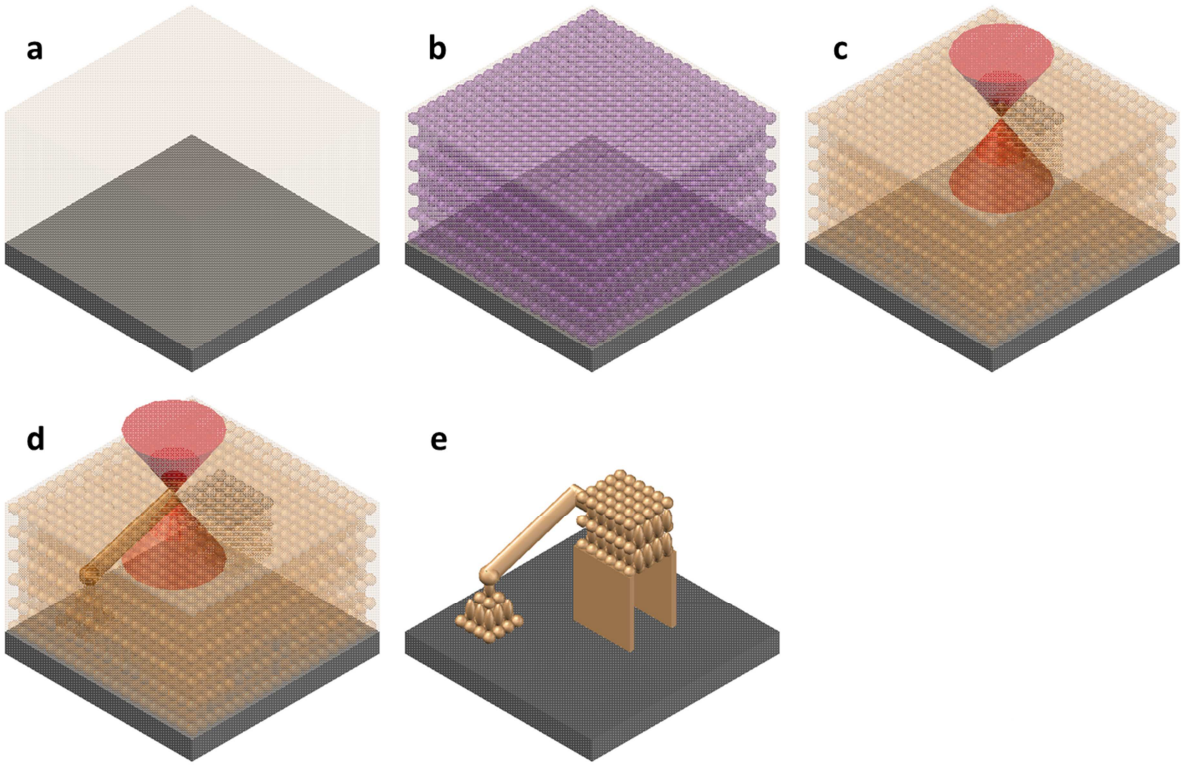

Figure 5-2: Schematic of the combined FLaSk and 3DDW process on a dye-doped CAR. (a) Deposition of the active resist layer. (b) IL exposure by phase mask or multibeam. (c) FLaSk step: CW heating beam at the wavelength of the dye absorption is moved through the resist, locally annealing the IL-exposed, chemically activated resist creating a crosslinked 3D structure. (d) 3DDW step to define solid features such as supports, defects, or other structures not a part of the IL pattern. (e) Development of the patterned structure without additional post-baking.

FLaSk-CAP is the extension of FLaSk and LSA of CARs to 3D. Figure 5-2 shows an idealized schematic for the eventual capabilities of FLaSk-CAP. In FLaSk-CAP, the broadly focused rastering laser beam is replaced with a high numerical aperture, focused visible source. This allows for 3DDW LSA with sub-micron features possessing hierarchical substructure defined by the IL step. Ideally, this process occurs without the DW beam performing additional photoinitiation, thus maintaining the contrast and fidelity of the IL. By selecting from the broad palette of available IL structures, the pre-image of exposed PAG within the CAR may be defined either globally or vary within a range of possible fills (including no fill and complete oversaturation) as a function of position. The FLaSk exposure then selects regions

where the patterning will be fixed, allowing for the definition of lines, dots, and complex geometries of the chemically biased pattern. Further, in IL of CARs, the filling fraction of the final structure, a critical factor in device design, is defined by a combination of the exposure fluence and the PEB time. Other than variations due to factors such as optical absorption, fluence and PEB are generally considered to be homogeneous over the sample as normally desired. In the case of FLaSk, however, the thermal history and thus the PEB can be set by the DW parameters. This should, in turn, allow for tuning of the fill fraction of patterned structures and even the introduction of controlled defects by either multiple exposures or continual varying of either parameter. By using PMIL with multiple motifs, it may be possible to incorporate multiple patterns on the same sample by using a hybrid mask and avoiding the regions of overlap, something that would impossible by a global exposure where these intersecting regions would result in undesirable effects. If effectively controlled, these degrees of freedom should enable the patterning of 3D devices to a degree that would be impossible by any technique other than 3DDW.

While the potential speed and parameter space for the FLaSk process of CARs is highly promising, there are components of devices where it is undesirable for the IL sub-structure to be present. Examples of this include: supports, interconnecting waveguides, or high-Q defects. For the purpose of such structures, 3DDW possesses a great advantage over FLaSk. Integration onto a DW stage allows for the possibility of consecutive FLaSk and 3DDW steps to pattern these or any other 3D structure with a differing motif than the IL pattern. Through this, the design freedom of the FLaSk combined with 3DDW becomes immense, while at the same time, by placing the bulk of the patterning on the FLaSk and minimizing the 3DDW steps, the potential scalability when compared to 3DDW alone or a layer-by-layer process is enhanced.

In terms of practical considerations for FLaSk-CAP, the major property requirement is for the photoresist to contain two distinct ranges of optical absorption – one for the activation of the PAG by either single or multiphoton excitation and one for the LSA. This is in order to accomplish the local PEB

with minimal additional photoinitiation. Without the existence of a natural absorption band in the resist, an absorbing agent, such as a dye, that is relatively transparent in the region of the spectrum where crosslinking occurs (generally UV) is needed. Thus, the development of FLaSk-CAP is as much a question of materials selection and chemical design as definition of patterning parameters and processing.

5.2. *Simulations of FLaSk-CAP*

In order for FLaSk-CAP to become a viable technique for device applications, it is necessary to be able to predict the expected results for a set of experimental parameters. Given the wide variety of possible IL structures and difficulty of 3D structural analysis, it would be impractical to attempt to utilize purely empirical methods to form a catalog of FLaSk-CAP structure-dose behavior. Fortunately, the individual steps of FLaSk-CAP, composed of IL (electromagnetic (EM) and photochemical), FLaSk (EM and thermal), and the resulting structuring (chemical and thermal) are compatible with FEM simulations. These can be integrated together to form a multiphysics fine-grain simulation of the FLaSk-CAP process, but the degrees of freedom and mesh size necessary for EM is prohibitive for large simulations. In most cases, the EM components of the simulation can be performed analytically, since both the IL and FLaSk exposure is dependent only on the total intensity and the polarization is unimportant. It is important to note that this is certainly not the case for either the detailed MB or PMIL process, where the polarizations of the incident beam(s) can lead to vastly different intensity distributions. In both cases, however, the resulting distributions can always be expressed by Fourier series, either predictively (MBIL) or through a spectral decomposition of a precalculated distribution (PMIL). What follows is a discussion of the fine-grain simulations of the FLaSk-CAP process that were used to access the feasibility and study the components of the technique. After, coarse-grain approximations of these simulations for larger scale approaches will be discussed.

5.2.1. **Fine-grain chemical modeling of IL**

The kinetics of PEB have been studied both experimentally and theoretically for a variety of CARs,[186-191] though most often for thinner films designated for 2D lithography. In experimental kinetic studies, optical techniques are used to track the transformation of bulk films, giving the rates of crosslink formation and acid depletion and diffusion. The general equations for these processes, following the form of Li *et al.*,[189] are as follows:

$$\dot{M} = -k_D M^p H^q \qquad \textbf{Eq. 5-1}$$

$$\dot{H} = -k_A H^m + \nabla \cdot (D_H \nabla H) \qquad \textbf{Eq. 5-2}$$

Where M and H are the concentrations of protected groups and photoacid respectively, p, q, and m are the reaction orders, the ks are the reaction rate constants, and D_H is the diffusivity of the photoacid, which is assumed to be negligible at the timescale of FLaSk-CAP. The fine-grain components of the simulation are inserted in the rate constants, which take an Arrhenius form and thus possess a mapping related to the instantaneous temperature, and initial concentrations, which are defined by the EM exposure. While the initial value of M is a property of the resist, the initial value of H is determined by the resist properties and the photoexposure, as expressed in the following:

$$H_{init} = G\left(1 - e^{-CE_{exp}}\right) \qquad \textbf{Eq. 5-3}$$

Where G is the concentration of PAG groups, C is the photoinitator sensitivity, and E_{exp} is the dose energy of the IL exposure. It is in this initialization of the acid concentration that incorporates the first analytical EM step. More specifically, E_{exp} is evaluated as the appropriate Fourier series for the IL exposure. In order to increase the accuracy of this step, the E_{exp} can be multiplied by an appropriate decay factor to account for the absorption of the photoinitiator (related to C by the yield of the initiator). Ideally, this factor will be near to zero for the thickness employed, which can be accomplished either by use of a high IL dose or non-liner multiphoton IL where only a small fraction of the incident radiation at the

highest intensity regions is absorbed. While, no purely chemical fine-grain simulations were performed, the fine-grained coupled simulations used the parameters found in Table 5-1 for SU-8.

Table 5-1: Chemical parameters for coupled simulations

Parameter	Value
SU-8	
Protection Concentration	5.0e7 μm^{-3}
A_{pro}	1.28e12 $\mu m^3 \cdot s^{-1}$
E_{pro}	141.99 $kJ \cdot mol^{-1}$
Acid Concentration	4.5e7 μm^{-3}
A_{acid}	29.2 $\mu m^3 \cdot s^{-1}$
E_{acid}	70.0 $kJ \cdot mol^{-1}$
Acid Reaction Order	2
Positive Tone (normalized)	
A_{pro}	2.9 s^{-1}
E_{pro}	5.98 $kJ \cdot mol^{-1}$
A_{acid}	3.5 s^{-1}
E_{acid}	4.92 $kJ \cdot mol^{-1}$

5.2.2. **Fine-grain thermal simulations of FLaSk**

The second major component of a FLaSk-CAP simulation is the thermal behavior. Here, the governing physics is the canonical heat equation:

$$\dot{\boldsymbol{T}} = \frac{\mathbf{1}}{\boldsymbol{c_P \rho}}\left(\boldsymbol{k \nabla^2 T + q}\right) \qquad \textbf{Eq. 5-4}$$

Where T is the temperature, c_P is the heat capacity, ρ is the density, k is the heat conductivity, and q is the thermal power source. In the case of FLaSk, the q term in Eq. 5-4 arises from EM excitation of the resist and takes the form of:

$$\boldsymbol{q = \eta_Q \alpha e^{-\alpha d} I} \qquad \textbf{Eq. 5-5}$$

Where η_Q is the loss efficiency, α is the absorption of the resist, d is the distance from the surface of the resist and I is the optical intensity, which can be approximated analytically by Gaussian optics equations:[192]

$$I = I_0 \frac{1}{1 + \left(\frac{\lambda z}{\pi w_0^2}\right)^2} e^{\frac{-2r^2}{w_0^2\left(1+\left(\frac{\lambda z}{\pi w_0^2}\right)^2\right)}} \qquad \textbf{Eq. 5-6}$$

Despite the apparent complexity of this expression, besides the spatial variables (which are relative to the focal position of the beam), it contains only three parameters: I_o, the total incident intensity, λ, the wavelength inside the material, and w_0, the minimum beam radius. The final parameter can be approximated from the objective NA as $w_0 = {}^{2\lambda_0}/_{\pi NA}$, with λ_0 being the free space wavelength.

Eq. 5-5 introduces two important considerations to the selection of materials for FLaSk CAP. More specifically, the exponential decay indicates that the overall α must be relatively small to not result in a large difference between the heat source at the top and bottom of the film or even the top and bottom of the hot spot (both generally compounded by the thermal conductivity of the substrate vs. the superstrate), while the η_Q value should be as high as possible (*i.e.* low fluorescence). Both problems could theoretically be solved by using a very low doping and very high I; however, there are practical limitations to this that will be discussed in 5.3.

One important advantage of not using the complete EM simulation is that, in absence of motion, Eq. 5-6 is cylindrically symmetric about an axis that passes through the focal point of the heating laser. Using this fact, it is possible to rapidly assess the target resist properties as well as the effects of the substrate and superstrate. For example, in the case of dye loading, it is not guaranteed that a

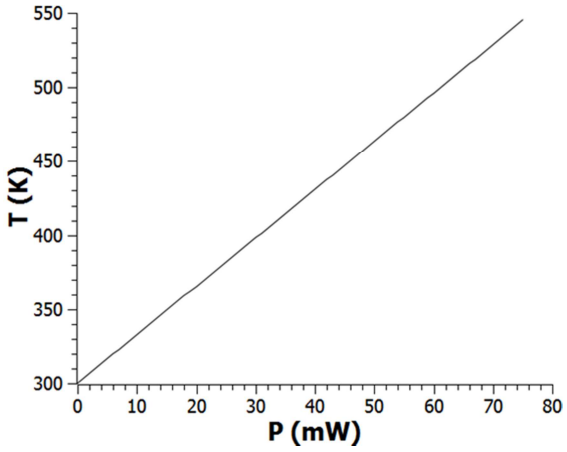

Figure 5-3: Simulated power to temperature relation from a typical polymer system with doped absorption of 25 cm^{-1}.

sufficient temperature for rapid LSA could be achieved without significantly decreasing the penetration depth of the heating laser or increasing the necessary intensity beyond a reasonable value. According to the previous work on LSA of CARs,[153] sub-millisecond PEB results similar to hotplate PEB were obtained when calculated LSA temperatures were ~20% greater than the corresponding hot plate temperature. Though not explicitly stated in the prior work, curves of a similar shape in both the sensitivity and extent of diffusion appeared to correspond to factors of 1.21-1.22 greater temperature in K (*e.g.* 388 K vs. 473 K, 423 K vs. 513 K). This would call for a FLaSk temperature of ~450 K for most conventional resists. Taking 500 K as a target temperature, a practical restriction of the depth loss due to the decay term in Eq. 5-5 was taken to be a variation of 10% in 30 μm of depth (a high value for reasonable depth of uniform UV IL). This criterion can be translated into a maximum α of 35 cm^{-1}. Therefore, the first fine-grain simulation was to determine the appropriate power range to achieve the target temperature with an optical loss lower than the specified tolerance (*i.e.* $\eta_Q<1$). This model utilized a geometry typical for high numerical aperture immersion DW: a glass substrate and silicon superstrate encasing 35 μm of active material. The cell extends 100 μm radially to prevent any effect of the low thermal conductivity of the resist. Thermal and optical properties for these layers are shown in Table 5-2. The absorption was set to a constant 25 cm^{-1} (η_Q=0.714) in the resist layer. The power of a 780 nm heat source focused in the center of the active region was gradually increased while monitoring the peak temperature (Figure 5-3). This approximate model showed that degree of optical absorption selected for the model was more than sufficient to reach a target maximum temperature of 500 K, which was shown to occur at ~60 mW of light intensity. This is not a high intensity even for a handheld laser pointer diode, let alone lab systems, and should further not be excessive enough to cause unwanted effects at most wavelengths.

Table 5-2: Optical and thermal parameters used for coupled simulations

Parameter	Value
N	1.6
$\rho_{polymer}$	1190 $kg \cdot m^{-3}$
$k_{polymer}$	0.19 $W \cdot m^{-1} \cdot K^{-1}$
$C_{polymer}$	1420 $J \cdot kg^{-1} \cdot K^{-1}$
ρ_{silica}	2203 $kg \cdot m^{-3}$
k_{silica}	1.38 $W \cdot m^{-1} \cdot K^{-1}$
C_{silica}	709 $J \cdot kg^{-1} \cdot K^{-1}$
$\rho_{silicon}$	2329 $kg \cdot m^{-3}$
$k_{silicon}$	130 $W \cdot m^{-1} \cdot K^{-1}$
$C_{silicon}$	703 $J \cdot kg^{-1} \cdot K^{-1}$

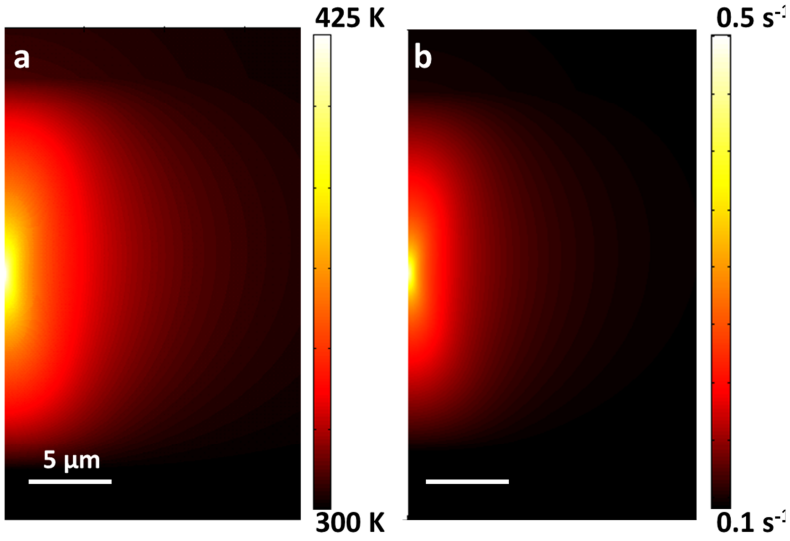

Figure 5-4: (a) Thermal profile results for the axially symmetric FEM simulation of FLaSk at a power of 35 mW. 15 µm of active layer was placed between two 100 µm layers of glass with the radial boundary set 100 µm from the center. All boundary conditions were set to a constant temperature of 300 K, which was also the initial temperature. Absorption was set at 25 cm^{-1}, and the light source was modeled as an ideal Gaussian beam with λ=780 nm and NA=1.3. (b) Rate constant map calculated from the thermal profile in (a) using an Arrhenius model for SU-8.

The cylindrical fine grain model also allows for some quantitative assessment of the expected resolution and uniformity of the FLaSk technique. Figure 5-4a shows the thermal distribution obtained in the active region of the previously described sample geometry for a 660 nm laser in 25 µm of resist at an incident power of 15 mW (a scenario closer to the ideal patterning). The computed FWHM ellipsoid of ΔT (though the distribution is distinctly non-Gaussian) has a diameter of 3 µm and a height of 10 µm. It is important to note that this is not necessarily the most accurate metric of the resolution; rather, the rate constant, k_c, of the crosslinking reaction serves as a better gauge. Plotted in Figure 5-4b is k_c determined by an Arrhenius model using the parameters from Table 5-2 for SU-8. The effective

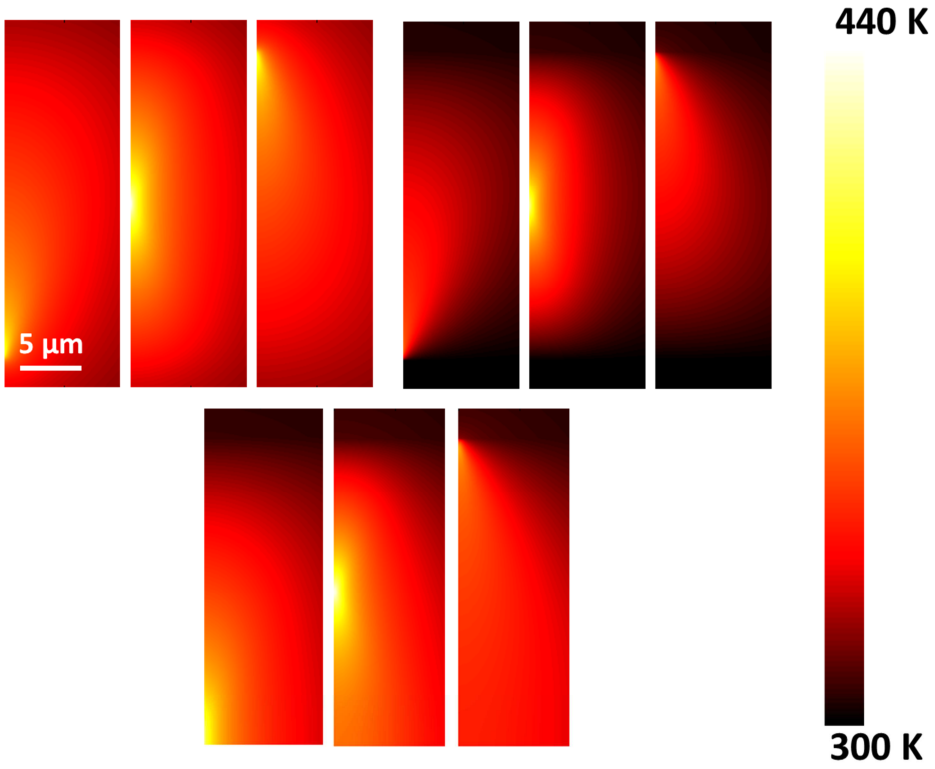

Figure 5-5: Thermal profile with focus set at the center and 12 µm above and below center for a thermally matched substrate and superstrate, maximum temperatures are indicated in white. Also shown are profiles for glass-resist-silicon (e) and glass-resist-air.

resolution is much improved (d=2 µm, h=7 µm), though in the FLaSk application it may not be the case that the tightest focus is desired for the purpose of rapid patterning, as will be discussed in 5.4.3.

Such simulations can also give insight to the expected uniformity of the ellipsoidal thermal profile. Changing the focus or the material of the sub- or superstrate affects the symmetry and local thermal environment of the sample geometry. Figure 5-5 shows temperature profiles for three focal points inside of some possible sample geometries: (a) thermally matched with non-photoactive resist above and below, (b) glass above and air below, and (c) glass above and silicon below. In all three cases, there is some distortion of the thermal profile due to the change in materials properties. The distortion seems mainly to affect the shape of the profile away from the focal spot, likely due to the relatively low thermal conductivity of the resist. More critical is the change in spot temperature at differing foci. Even the best

case – for the thermally matched resist – shows a considerable distortion and (36 K) temperature difference, which must come from a lack of absorption in the boundary resist. In such a scenario (for example, a polymer immersion coverglass and a thermal spacer before the substrate), distortion could be corrected by using boundary layers that also contain absorbing dye. In the other two cases, the distortion and temperature difference is much greater, displaying the extremes of the thermal distortion – a highly non-conductive (air) substrate and a highly conductive (Si) substrate. In the first case, the scenario representing the most typical 3DDW sample geometry of patterning through a glass coverslip into a spun layer of resist, the profile takes on the unusual, but intuitive, feature of extending to the resist surface albeit with a more stable (Figure 5-6) temperature profile. This behavior at first seems undesirable, but the extended zone of uniform heat could be beneficial in a situation where a thick slab of uniform structure is desired. In other situations, this issue can be easily solved by adding a very thick buffer layer *after* the patterning by using, for example, the orthogonal solvent method described in 2.3.4. In the case of the semiconductor substrate, the temperature of the focal spot changes by 10% over a distance of 10 μm, compared to the thermally matched case of 5%. These changes in temperature and profile could be compensated for by use of thermal spacers, however, they are likely to always remain to some extent. In accepting this reality, what remains is to address whether desired structures may still be obtained by clever programming of the dynamic patterning power control utilizing, for example, an AOM or EOM, the use of such an experimental system for gradient structures will be discussed in 5.4.5. As important as the experimental apparatus is the ability to solve the inverse problem and thereby inform the patterning parameters, which will be considered in 5.2.5.

While much can be learned from cylindrical simulations, they are not appropriate for time-dependent studies of the full process FLaSk. To simulate a time dependent pulse with cylindrical symmetry would effectively be simulating a stationary pulse since a moving line does not possess cylindrical symmetry. Nevertheless, the case of such a pulse is not entirely irrelevant since it can be used to consider the amount of time necessary to achieve peak temperature – it is given that there will be a finite time required to achieve stability in any write process. For example, in conventional laser DW, whether guided by a galvano-mirror or piezostage, there is some acceleration from the stationary state before the final speed of writing is achieved in addition to an amount of time for the intensity controlled laser to reach full power. With modern AOM technology, the latter can be nearly instantaneous, but the former will always lead to overexposed regions at the start end of the written line. In the case of 3DDW with an AOM, this can be corrected by ramping the power up at a matched rate with the laser spot motion. In the case of FLaSk, there are the additional considerations of achieving thermal steady state. Consider, for example, a case where the thermal conductivity of the resist approached zero. In such a case, the temperature at the focal spot would continuously increase in temperature on any relevant time scale and, even with the laser off, could persist as a slowly spreading hot spot for a considerable length of time. Were this to occur, a precise control of the baking history at any given point of the resist would be impossible, especially in the case of a moving laser spot. Alternatively, an infinitely conductive resist would allow for instantaneous thermal steady-state and therefore, perfect control of the thermal history. As most resists are polymeric in nature, the actual behavior falls between these two extremes, leaning toward the former. The practical consequence of this fundamental limit in the accurate patterning rate is the ultimate resolution of the system, as it would be very difficult to account for thermal drag affecting surrounding areas.

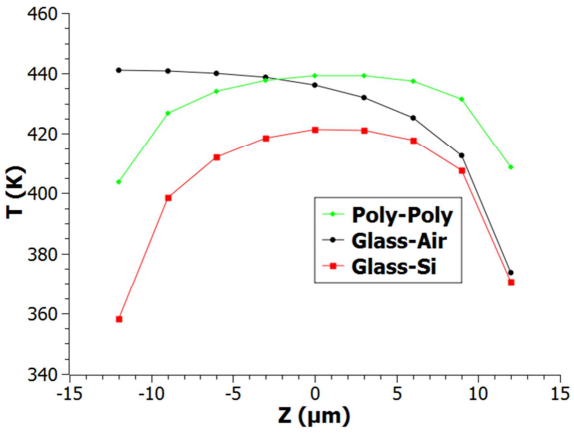

Figure 5-6: Tabulated peak temperatures for various focal positions in the simulated samples described in Figure 5-5.

To assess the extent of this limitation, cylindrical simulations in the same cell with glass superstrate and silicon substrate were utilized in a simulation of a thermal pulse. In this experiment, an instantaneous (to isolate it from ramp up effects) 40 mW rectangular pulse is applied for 0.6 ms and the time to plateau both upward to peak temperature and during the return to ambient temperature were observed (Figure 5-7a). From the results of this study, it can be observed that the peak/ambient stabilization is the limiting step at a time-to-stability (±5 K) of ~10^{-4} s. Several thicknesses were considered to determine at what thickness the resist could be approximated as behaving like an infinite film of resist (worst case scenario), which was shown to be ~15 μm. To approximate the limitation that the finite ramping places on the write speed, one must consider the amount of time that a point in space spends in the hot spot of a moving beam. As this time approaches the time to thermal stability, there will be a difference between the temperature at the beginning and end of the pass. The net effect of this will be that the temperature in the written line will gradually increase until the steady state temperature (which will be different for a moving spot, but related) was eventually reached leading to a non-uniform bake. The dwell time at a single point can easily be approximated as the spot size divided by the write speed. For a 500 nm spot, this therefore limits the speed to ~5 mm/s.

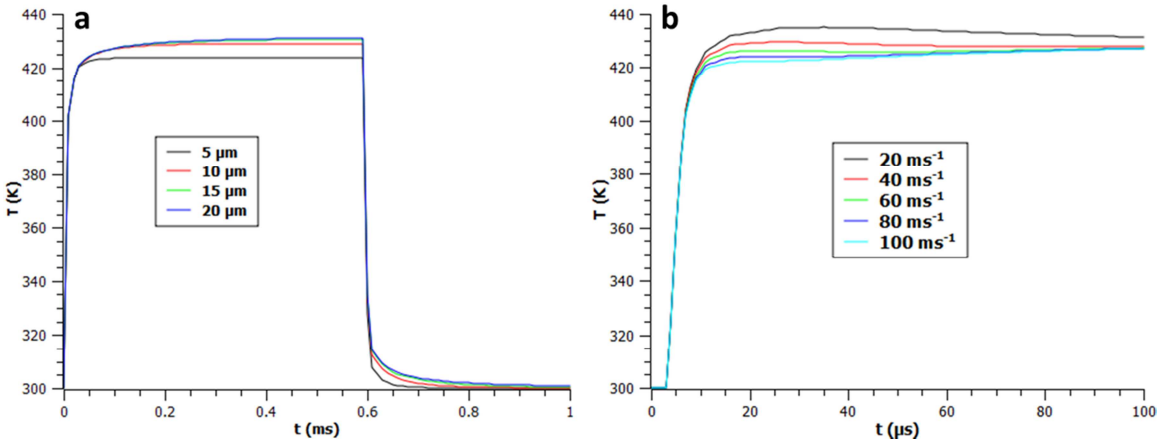

Figure 5-7: Simulated tests of thermal stability. (a) The time to equilibrium for a thermal step function for different thicknesses of resist. By 15 µm, the film thickness, the time to equilibrium reaches a maximal value, making it indistinguishable from an infinite film at ~0.1 ms. (b) Use of a preliminary spike to decrease the time to equilibrium to ~10 µs.

It was discussed previously that for 3DDW, the ramping problem can be addressed by ramping the intensity in a commensurate fashion with the speed in order to achieve a uniform dose profile. It is tempting to attempt a similar strategy for decreasing the time-to-steady-state of the thermal profile, but in the *reverse*. Namely, overdosing the early portion of the line and then ramping down to the target intensity/temperature. Figure 5-7b shows an attempt at improving the time-to-stability by applying the following form to the power:

$$P = P_0 * (1 + p_c e^{-rt}) \qquad \textbf{Eq. 5-7}$$

With P_0 being the target final power, p_c being the overshot correction, and r being the decay rate of the correction. It can be seen that at a correction of p_c=0.2 and r=40 ms^{-1}, the sample reaches the target temperature within 10 µs without exceeding the maximum temperature, thereby increasing the bound for the maximum write speed to 5 cm/s. This is near the current record for high resolution DW patterning speed achieved by galvanomirrors.

As discussed above, simulation of the complete FLaSk process cannot be executed with cylindrical simulations. For this reason, further thermal studies (other than simplified models that will be discussed in

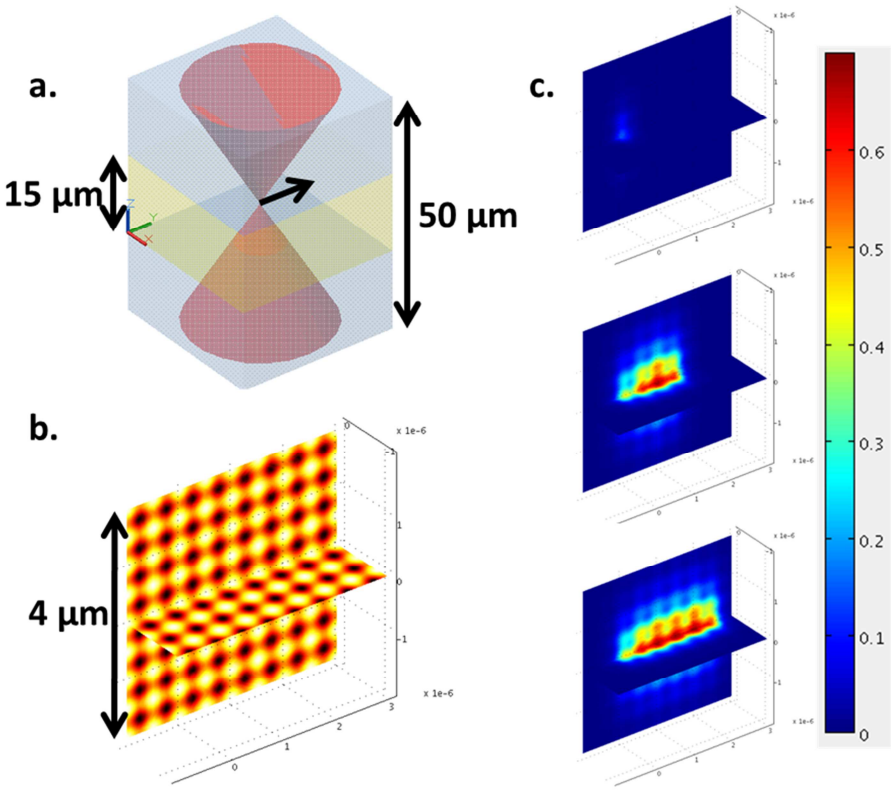

Figure 5-8: (a) Schematic of transient simulation of FLaSk anneal indicating the cell size. 35 mW was selected to achieve the desired temperature of ~450K and a write speed of 100 µm/s was selected. (b) For the purpose of the chemical model, IL was implemented using the Schwartz P-surface to define an IL pattern with 500 nm periodicity. (c) Results of the kinetic model at 1, 15, and 25 ms. Deprotection of the IL defined pattern up to a maximum fraction of 0.7 is observed in the moving FLaSk line.

5.2.2) require full 3D simulations, which, among other things, greatly increase the computational cost of FLaSk simulations (one of the considerations that will lead to the approach of coarse-grain models in 5.2.5). The computational cell utilized in these simulations is shown in Figure 5-8a. Relative to the size of the thermal spot (~1 μm) the cell is quite large, a consequence (once again) of the low thermal conductivity of the resist, as a result, multiple mesh sizes are utilized to allow for finer resolution near the focal spot, and keep computational requirements to a minimum. Another way this is done is by recognizing that the process, while 3D, does possess a plane of mirror symmetry along the write direction if the writing is conducted in the plane of the sample cell. Thus, only half of the system need be simulated. Beyond these considerations, the materials and exposure parameters of the 3D system are kept the same as those used in the cylindrically symmetric case with a glass superstrate and silicon substrate to make a simplified 3DDW geometry.

5.2.3. **Fine-grain thermochemical simulations of FLaSk**

Having established a framework for both the chemical (5.2.1) and thermal (5.2.2) modeling of FLaSk-CAP, it is possible to perform coupled thermochemical modeling of the FLaSk process. The cell utilized in the 3D studies discussed in 5.2.2 was utilized as a platform for the combination of the thermal model with the chemical parameters defined in Table 5-1 for SU-8. For the value of E_{exp} from Eq. 5-3 we selected the Schwartz's P-surface, which is a profile that can be achieved by MBIL and possesses a simple mathematical representation. Additionally, the P-surface has been identified as a family of structures that can possess photonic bandgaps[193] and is a bicontinuous structure, which is essential for application of FLaSk-CAP to positive tone resists, which, as will be discussed in 5.3.1, is one of the target capabilities for the final technique. The specific form of the P-surface used here (Figure 5-8b) is:

$$E_{exp} = \frac{E_{max}}{6 + e_{min}}\left(3 + e_{min} + \cos\frac{2\pi x}{a_x} + \cos\frac{2\pi y}{a_y} + \cos\frac{2\pi z}{a_z}\right) \qquad \textbf{Eq. 5-8}$$

Where the *a*s are the respective lattice parameters (here all a uniform 500 nm), E_{max} is the maximum dose of the exposure pattern and e_{min} is the unitless portion of exposure at the lowest dose regions of the

pattern. This last term is especially important as it illustrates the lack of perfect contrast and the potential for patterning of a fully solid object (from the negative tone point of view) despite the application of a deliberately selected exposure distribution. Here the e_{min} was taken as a typical value from an IL text[27] of 0.765 (corresponding to ~6% minimum exposure). E_{max} was tuned for appropriate final contrast. Through this prepatterned resist, a 35 mW, 100 μm/s beam is passed. Results of this simulation are shown in Figure 5-8c. As the FLaSk beam moves through the sample, it progressively defines a line with hierarchical structure prescribed by the P-surface IL step up to a reaction completion fraction of 0.7. These results clearly demonstrate not only that the FLaSk process provides adequate thermal treatment to locally deprotect/crosslink the resist, but, more critically, that this process can take place in a relatively small region and, further, maintain a consistent spot size, aside from the start of the line. This latter effect is likely unavoidable as there will always be an edge transition to the sample, however, depending on the cutoff for development, may not result in patterning upon development. Further, the extent of this region is already quite limited (~200 nm).

Despite the amount of work that went into arriving at this result, there are several discouraging aspects to it. The most obvious is the computational complexity. The displayed result is a 30 ms simulation that writes a 3 μm line. This represents a 1.5 million degree of freedom simulation that takes a current top-of-the-line twelve core server 3 hrs. Considering the capabilities of cloud computing, this is not necessarily prohibitive; however, there is also no simple route to an *inverse* solution in this manner that is immediately apparent, though one could imagine, given a target structure, starting with a guess for intensity and then varying it on a point-by-point bases until the target structure is achieved. This is not impossible (and is in fact how the coarse-grained inverse solver described in 5.2.5 operates), but is beyond our current capabilities. Regardless, this simulation serves as an excellent starting point to demonstrate the feasibility of a controllable FLaSk-CAP patterning process.

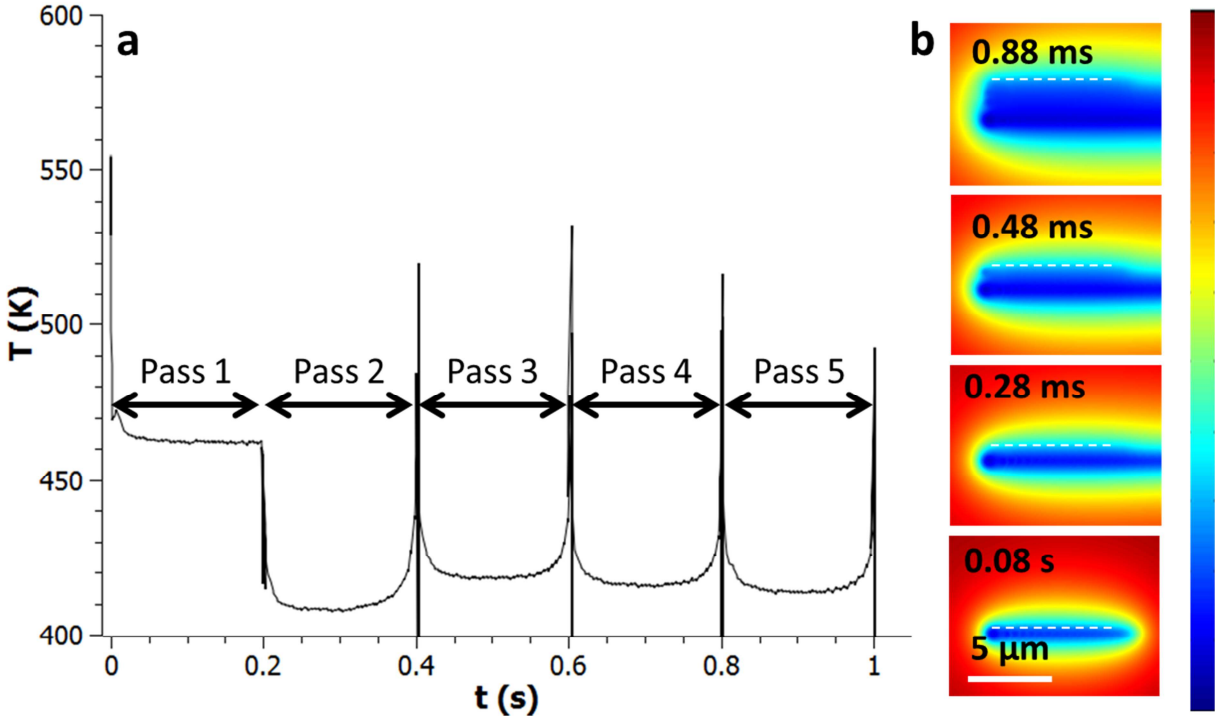

Figure 5-9: Simulation of exaggerated dye bleaching in a 2D system undergoing rastered chemical bleaching. (a) A plot of the peak temperature during five passes at 100 µm/s. The first exposure and pass (along with the first and last exposure in each line) demonstrate elevated temperature. While the second pass occurs at a lower temperature and then a gradual decrease to steady state bleached temperature. (b) Normalized absorbance map during the passes with the current writing position indicated by the dashed line. It can be seen that the tail created by the source leads to the lower maximum temperature in the following lines.

While full fine-grain thermochemical simulation of FLaSk-CAP is somewhat impractical, it can be utilized to design a simple test system for a phenomenon that is critically important to the experimental FLaSk-CAP process – photo/thermochemical dye bleaching. As will be discussed in 5.3.2, real thermal dyes often possess bleaching mechanisms that make their thermal absorption vary during exposure. Were the thermal spot infinitesimally small, any single exposure irrelevant of the bleaching behavior, would be indistinguishable from any other; however, the laser spot has a finite size and, further, the spatial range of its effect on thermally activated chemical processes depends on its intensity. To investigate the actual effect of dye bleaching, a simple 2D cell was set up with a chemically bleaching absorbing dye and a

rastered Gaussian laser spot. The results of this study are shown in Figure 5-9a. It can be seen that the initial exposed point occurs at a peak temperature of 560 K, but then subsequent points in the first line occur at a lower, but relatively stable temperature of 465 K. Beyond the higher exposure of the initially exposed point, this result would not be prohibitive to controllable patterning; however, the second line reveals the real issue with the use of a bleachable dye. Patterning of the subsequent lines (other than the first spot which is always high) occurs at lower temperatures – 405 K the second pass, 425 K the third and slowly decreasing towards the temperature value of the second pass beyond. The reason for this (illustrated in Figure 5-9b) is that the heating laser light bleaches all surrounding dye, because of this, the initial exposure creates a bleached circle which lessens the temperature of the next exposure in the first line, which in turn progresses the bleaching. This cycle continues as the patterning progresses, but, because the bleaching reaction initially occurs rapidly and then asymptotes, the temperature stabilizes. As the second line begins, it goes through this process, but with a lower initial starting point. For all lines after these first two, an alternating sequence of two temperature ranges begins as a procession of high-temperature/bleaching and low-temperature/bleaching. While these ranges are close to each other, they are still far from the temperature of the first line. This is one of the several issues that leads to what we refer to as the "hot line" effect which will be discussed in 5.4.3, and represents one of the major stopping blocks to FLaSk-CAP as a reliable process.

5.2.4. **Fine-grain EM simulations and analytical modeling of multiple PMIL**

One of the initial promises of FLaSk-CAP outlined in 5.1 was the ability to sample not only one, but multiple patterns from the library of possible IL structures in a single patterning step. The previous simulation sections have shown the potential for the FLaSk-CAP process to effectively fix an IL structure, but these have only been considered for a single pattern. MBIL cannot effectively generate multiple patterns due to the beams arriving at the sample from the far-field. In the case of PMIL, however, the patterning beams are generated in immediate proximity to the resist. It is simple to design a phase mask consisting of multiple, adjacent patterns stitched together in a single mask. It is similarly apparent, however, that the interface between patterns on the combined optic will not smoothly transition through the thickness of the material as the diffracted beams at this interface, much as with the edge of a PMIL sample, will not have commensurate diffracting beams coming from the other direction to generate the interferogram. In case of the single PMIL edge effects, there is no constructive interference of the unpaired beams leading to a relatively clean interface, such as has been demonstrated in local PMIL patterning by double imprint[35] or within microfluidic channels.[33] This is not the case for the hybrid interface, where beams from the adjacent masks combine together to generate a cone of distorted, aperiodic pattern. To illustrate this, Figure 5-10, shows a 2D simulation of monochromatic PMIL patterning of two adjacent gratings. The distorted region between them can be clearly seen.

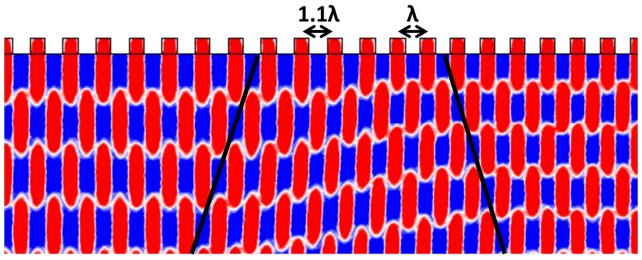

Figure 5-10: Evaluation of adjacent phase masks by 2D simulation of optical intensity. Intensity is plotted binary in terms of a cutoff. While 10% mask spacing can significantly change the pattern, there is a sufficient distance where the pattern is recovered (demarcated by the black lines).

As we have identified a source for the distortion the lack of beam pairing at the interface between multiple masks, and further, identified the source as something which can be described mathematically (diffraction), we can develop a simple analytical approximation for the minimum proximity of two

patterns originating from adjacent masks. Going back to the diffraction equations discussed in the FPnP section (2.3.1), the minimum separation can be defined as the distance travelled from mask interface of the shallowest diffracted beam of significant intensity from the masks through the thickness of the resist to be patterned. As this will most frequently be the first order, the distance can be expressed as:

$$s_{min} = t \cdot \tan\left(\sin^{-1}\frac{\lambda}{na}\right) \qquad \textbf{Eq. 5-9}$$

Where t is the thickness of the resist and s_{min} is the separation between the two films. For a typical set of parameters, this would allow for a proximity of around 1:1 for each micron of thickness. While not immediately proximate, this still represents a massive potential for patterning multiple periodic and quasiperiodic structures by a single FLaSk-CAP patterning step.

5.2.5. Coarse-grain simulations of FLaSk-CAP: finite difference approach

The full simulation method detailed in 5.2.1 consisted of a coupled thermal and chemical FEM simulation taking several hours to complete. There are multiple reasons for the complexity of the simulation (low symmetry, high resolution requirement, fully time resolved results, low thermal conductivity, etc.), many of which are intrinsic to the patterning method. To make matters worse, this simulation utilized a numerical approximation for a MBIL pattern rather than a complete simulation which would require another multiphysics step (EM simulation). With these requirements, both forward and inverse solution of large gradient patterned structures is currently impractical. As discussed in 5.1, FLaSk-CAP is not the correct technique for

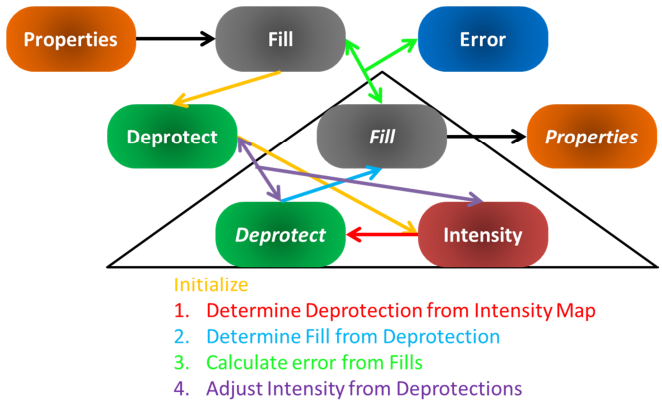

Figure 5-11: Simulation scheme for coarse grain simulations. Calculated values are indicated in italics Recursive loop is denoted by the steps in the triangle.

structures consisting of mainly submicron features, where 3DDW is the more appropriate method. FLaSk-CAP is rather suited for structures where the property in question (index of refraction, impedance, bandgap etc.) varies on a scale greater than the IL characteristic feature size (*i.e.* effective medium). In the effective medium case, the specific details of the structures should be less critical, and the overall simulation can be simplified by turning the problem into a coarse-grained simulation where the solution method involves simplification of the complex system into multiple approximate interpolated forms of tabulated data from previously solved, more accurate FEM simulations. Figure 5-11 shows a diagram of the coarse-grain solution method. In this procedure, the desired property is translated into a fill fraction map, something as trivial as a weighted average (density) or weighted squares average (index of refraction) of the properties of the material and the medium or as complex as an inverse band diagram calculation for the desired IL structure. From this starting point, a deprotection map is generated, which is utilized to make a first guess for the intensity map. Having so initialized the system, the optimization procedure proceeds – first, the intensity map is utilized to generate the fitted deprotection map, which can in turn be used to create a fitted fill map. This generated map is compared to the target to find a modified least squares error, the fitness function to be minimized. To progress to the next iteration, the initial and generated deprotection are used to adjust the intensity map. The necessary information and preparatory detailed simulations to perform each of these steps will now be discussed in detail.

Defining the Radial Temperature Profile

Cylindrically symmetric thermal simulations have already been discussed in 5.2.2. Here we adopt stead-state time independent solutions as a basis. This will act as a discretization of the thermal history. As with any discretization, this will lead to errors which will diminish with the resolution of the solving mesh (here, time step). Built into the discretization is an assumption of rapid transition between any two given temperatures within the span of the exposure time. There is a need to convert the profiles generated in FEM simulations of the hot spot into a numerically continuous, addressable form (such as an analytical discussion). Due to the complexity of the hot spot within the substrate-resist-superstrate system, it is

unlikely that a compact analytical form exists for the thermal profile, leading instead to the use of *splines*. Essentially, for each thermal simulation, MATLAB generates an interpolated map of all points, which can be stored in hard memory and loaded for future simulations. In this way, it is only necessary to generate a map for every given focal position and temperature and then utilize the symmetry of the thermal spot to select the appropriate spline for every point in the solver mesh. Of course, it is impossible to store a continuous (*i.e.* infinite) set of thermal maps; therefore, some reasonable approximations to limit the set of maps must be utilized. The first is that the shape of the thermal profile does not vary largely over the distance of 250 nm in focus. The second was that the shape of the thermal profile was independent of temperature and the magnitude of the excursion from room temperature (ΔT) varied linearly. While clearly an approximation, a comparison of temperature excursions at the extremum of the studied range near the substrate (where the profile shape is the most unusual) were used to demonstrate the relative validity of this model (Figure 5-12). The net result was a reduction of maps to four per micron of resist thickness, a very manageable number to keep in RAM for quick access. For the systems that will be discussed below, a set of thermal maps with silica superstrate and silicon substrate were defined for 660 nm light (an eventual target of the FLaSk technique) and the same optical and resist properties discussed in 5.2.2.

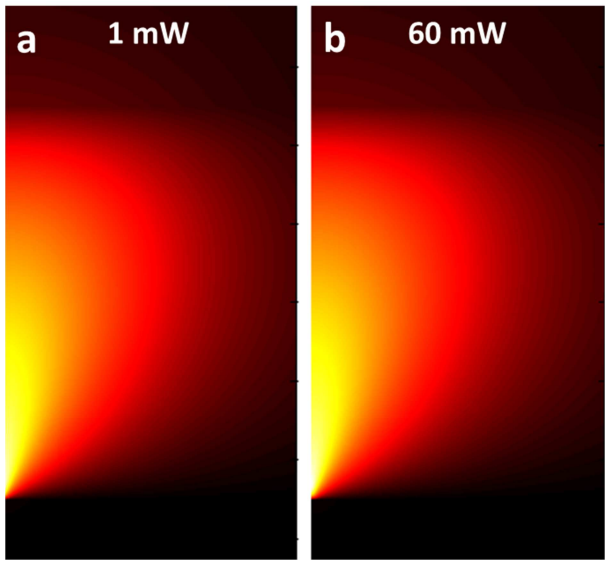

Figure 5-12: Comparison of thermal spot shape at an extremum focus (near the a high conductivity surface) at two very different powers. While there are some differences, the shape of the profiles are highly comparable.

Defining Deprotection Function and Fill Conversion

PMIL has many advantages over MBIL for a scalable FLaSk-CAP application, as discussed both in 5.4 and 5.2.4; however, from a simulation standpoint, PMIL is more computationally intensive as the intensity map cannot be expressed fully analytically. Because of this, the necessary mesh for simulation must contain at least four mesh units per wavelength inside the material, leading to it being a large component of the total calculation of a coupled multiphysics simulation. Fortunately, due to the symmetry of the system, a coarse-grained simulation can approximate a PMIL experiment to the solution of a unit cell, with the horizontal dimensions determined by the phase mask periodicity and the vertical by the Talbot length. The Talbot length is the distance to repeat of the EM distribution from an infinite diffracting optic and is determined by the mask dimensions, the optical properties of the material and mask, and the wavelength used for exposure. It can be approximately expressed as:

$$z_T = \frac{2a^2 n}{\lambda} \qquad \textbf{Eq. 5-10}$$

Where z_T is the Talbot length. There are several important assumptions made in utilizing the unit cell of the phase mask, the most critical being the *z*-positional independence of the exposure field. This is not generally the case due to the absorption of the photoresist necessary to initiate crosslinking, which would result in a gradual decrease in the exposure intensity through the thickness of the resist. Much as with the MBIL case, this effect can be rendered relatively negligible for finite resist thickness by use of low absorption and high intensity light, such as is used in multiphoton exposure or band edge absorption. The latter is the preferable method for FLaSk-CAP due to the fact that UV-absorption, either by single or multiple absorption, tends to bleach or decompose all materials, such as those necessary for subsequent FLaSk heating or MPL exposure. This could be addressed by the utilization of pulsed NIR light and visible-band MPL absorption, but this would place limitations on the resolution of the mask as detailed by Eq. 5-10, where the z_T shrinks to the point where the structure is undefined as λ increases.

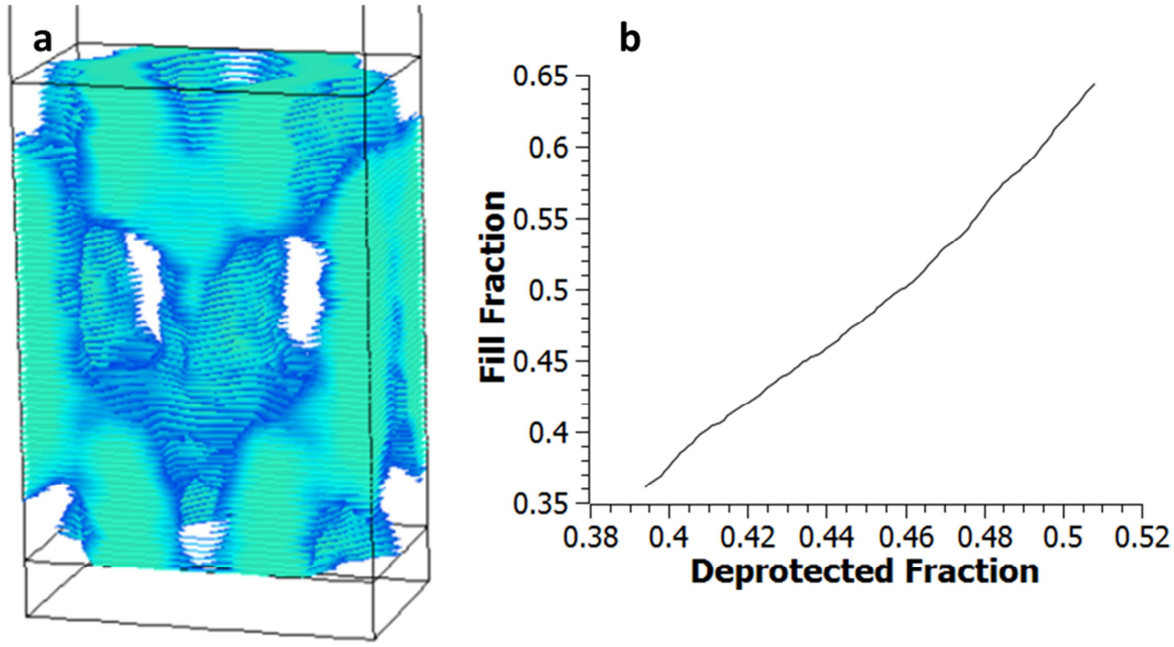

Figure 5-13: (a) Simulation cell and structure from a unit cell hexagonal phase mask EM simulation. The lattice constant is 600 nm. (b) Splined correlation between the deprotection fraction and the fill fraction between the threshold for connected solid structure and connected empty structure, which corresponds to the regime where a 3D structure can be developed (though this is relaxed for negative tone FLaSk strutures). Data was collected by meta-analysis of many different temperature bakes.

To obtain the solution to this reduced EM problem, here an *xy*-periodic mask pattern, as would be generated by nanoimprint, is illuminated from above to generate the PMIL exposure in a unit-sized box located some distance away from the mask pattern. The distance here is to allow for the formation of the periodic Talbot pattern without the ultra-near-field effects of the varying index at the mask region. Results of such an EM simulation conducted with circularly polarized green (532 nm) light on a hexagonal phasemask with 600 nm periodicity and optical and chemical parameters similar to those used in 5.2.1 are shown in Figure 5-13a. Given the ability to generate the unit cell, a thermochemical simulation equivalent to the one utilized in 5.2.1 can be executed at any given temperature and exposure to develop the deprotection profile as a function of time. This can in turn be related to the approximate fill fraction of the structure by applying a deprotection cutoff, representing the fill that occurs in a bulk resist after IL exposure and uniform baking with the same set of conditions.

Not all structures possessing deprotection above the cutoff leads to a structure of the predicted fill. Structures possessing either non-interconnected solid or empty phase will either fall apart upon development (non-connected solid phase) or will not have a path for the developer (non-connected empty phase) and will remain fully solid. This is equally applicable to both positive tone and negative tone resist systems. It should be noted, however, that in the case of local structures negative tone resists (such as those produced by FLaSk in 5.4), 2D connectivity of the empty phase is sufficient as there will always be sufficient access to a boundary of the structure for solvent diffusion. In the general 3D case, however, there is need to develop a robust method to determine where during a bake process the phases of the cutoff structure are co-continuous. This was done by finding all connected points in either the solid or empty phase and checking if any region within the cell is in contact with all six walls; if this is the case for both the filled and empty phase, this is a co-continuous stucture. The results of this script is to give bounds of the plot of fill versus deprotection (shown in Figure 5-13b), which for the parameters in Table 5-1 for a positive tone resist starts at an average deprotection fraction of 0.39 corresponding to a fill of 0.36 and ends at a deprotection of 0.51 corresponding to a fill of 0.66. While a relatively small range of fills, when translated to something like refractive index, even for a polymer (n=1.5) this can represent a range of n=1.2-1.35, which is sufficient for defining a core and a cladding of a waveguide, for example. For other sorts of properties (impedance, density, etc.) or even for semiconductors' refraction, this range is even of greater significance.

Returning to the deprotection function, much as with the thermal profile, it is not practical to define a time-deprotection function for every temperature for a given exposure. In this case, it is possible to define an analytic model for the deprotection. One necessary feature of the model used is that it must allow for *history-independent* determination of the temperature, deprotection and time uniquely given either of the other two parameters. The crux of the simulation comes down to the following problem – given a single (superwavelength) point in space that has been pattern by a (subwavelength) IL exposure followed by a series of (discretized) PEBs at various temperatures, what is the current deprotection at that point? If we

take that the problem is history-independent, it becomes an iterative problem and can be solved. In other words, if the reduced problem of the deprotection after the first bake and the second bake can be solved, then the "first bake" can be taken to be made up of many bakes (essentially an *n* and *n+1* solution). It can easily be seen that this could only be the case if the start and end points of the reaction were the same for every set of baking parameters. For a two component chemical reaction, such as the acid catalyzed deprotection of a CAR, this is only true if the proportion of reaction components stays roughly the same for all temperature bakes, or, more specifically, that the rate of acid loss is much slower than the rate of deprotection. For the purposes of this experiment, it was convenient to assume that the start and end point of the experiment were 0 and 1 reaction completion respectively, irrelevant of the thermal history.

To check the validity of this assumption, simulations were conducted for a range of temperatures between 298 and 573 K and several empirical models were tried to fit the average deprotection of the final cell. The final relation that was utilized was a two stage fit. The first was a one parameter exponential fit of deprotection reaction completion:

$$D(t,T) = 1 - e^{-r(T)t} \qquad \textbf{Eq. 5-11}$$

This is roughly consistent with any thermally activated process with *r(T)* as a rate constant. As the second part of the fit, the *r* is taken to have a form of:

$$r(T) = Ae^{qT^a} \qquad \textbf{Eq. 5-12}$$

Where A, q, and a are fitting parameters. The values of the parameters were fit as A=8.76e-6 s^{-1}, q=3.39e-5 K^{-a} and a=2.13 (close enough to 2 to be suggestive of a double activation process), and fits using Eq. 5-11 and Eq. 5-12 for the simulated deprotections are shown in Figure 5-14. It can be seen that the models do a relatively good job at producing the simulated result, which is a very useful result as it indicates that the desired iterative method can be used as described above. This now gives the ability to determine the unknown value given two of the values of the deprotection, bake time, and bake temperature. For the purposes of further discussion, these functions will be referred to as $D(t,T)$, $\tau(d,T)$, and $\theta(d,t)$.

Solver methodology

Equipped with a decoupled ability to study both the thermal process of FLaSk and the chemical evolution of the exposed resist, a methodology for the specific simulation can be developed. The starting point for any coarse-grain solution is a target structure. With given target fill, the first consideration is what portions (if any) are, in fact, appropriate for FLaSk. There are two obvious sorts of regions that cannot be patterned by FLaSk: regions with fill higher than the maximum and regions with fill lower than

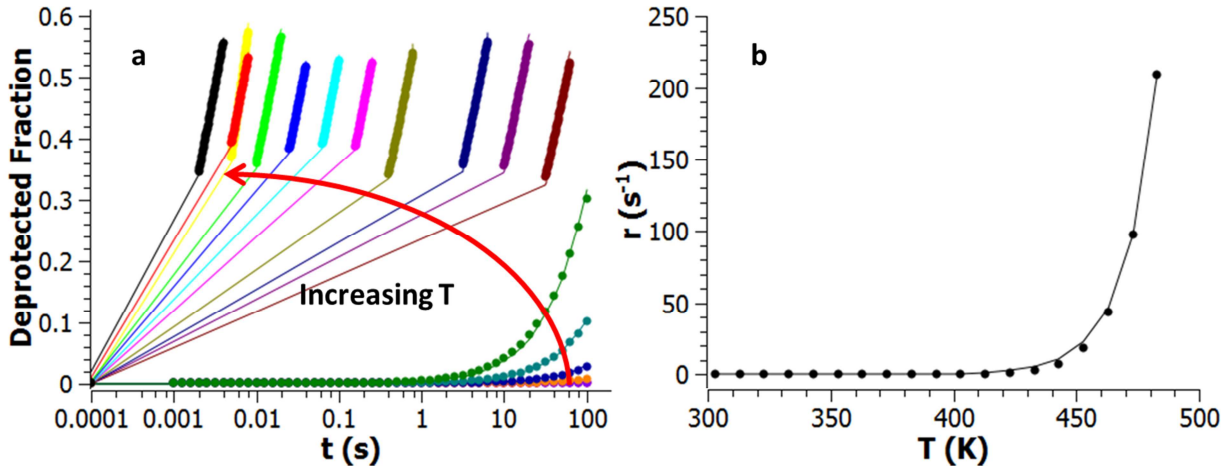

Figure 5-14: Attempt to find a history independent analytical model for FLaSk-CAP baking. (a) Semilog plot of the average deprotection extracted from simulated isothermal bakes fit to the single parameter model described by Eq. 5-11. (b) Results for the parameter *r* from the meta-analysis in (a) fit to Eq. 5-12.

the minimum. These areas require the use of 3DDW (as opposed to FLaSk) to reach their target fill, with the key difference between the two varieties of regions being that if the fill is greater than the maximum, the value of the fill from the FLaSk step can be completely ignored, as the 3DDW will be used to reach the target fill. In contrast, if the target fill is less than the minimum, the FLaSk must leave the fill less than the minimum or result in some structuring. Based on this initial consideration, it is possible to rule out certain target structures which end up requiring more 3DDW correction than patterning the same target fill simply by 3DDW would require.

Assuming this test is passed, the next step is to determine appropriate mesh sizes for the simulation. One beneficial choice for the computational load of the simulation is to separate the simulation into two meshes: one for the deprotection and one for the patterning. The reason for this is the relative resolutions – to capture the physics of the patterning, the distance between points within a FLaSk line must be, as discussed in 5.2.2, less than the effective point size divided by the write speed. Similarly, to obtain full control of the fill in 3D, the line-to-line separation must be smaller than the effective size of the spot to not have fill oscillations due to troughs between heated regions. In general, this amounts to ~500 nm in plane and ~5 μm out of plane. On the other hand, the necessary resolution of the mesh is proportional to the rate in change of the pattern. For example, to obtain a completely uniform pattern over a rectangle, it may be sufficient to determine that the fill at the nine points consisting of the corners and centers of each face, side, and of the object possess that fill value since values can be expected to vary smoothly in between two points if the intensity is not allowed to abruptly drop off in between probed points (which can be easily enforced). As a result, for gradually varying fill maps, mesh sizes on the micron scale can be expected to provide the same quality intensity fits as finer meshes. Thus, by uncoupling the meshes, each step of the calculation is reduced from an n^2 number of calculations to $n_1 n_2$, where the two mesh sizes (n_1 and n_2) can now be vastly different.

Another reason for the two mesh being decoupled is that the patterning mesh represents an actual experiment and thus should not extend into regions that possess fill, but will not, in actuality, be a part of

the laser path. Nevertheless, it is often important to know what is occurring *outside* of the patterned region. As an example, if there are requirements for the smoothness between the transition of the patterned region to its unpatterned surroundings, which can be accomplished by including a boundary of zero fill around the patterned region in the fill mesh. This is an unneeded consideration for instances where the boundary is the substrate, superstrate or a region that will be fully exposed by 3DDW or flood exposure, but does define an important guideline that the patterning mesh must always be contained within the bounds defined by the fill mesh. The other situation where decoupling of the meshes can represent the physical situation is where patterning occurs in a way incommensurate from the space occupied by the resist. For example, a 15 μm thick photoresist (naturally divided into either a 3 μm or 5 μm mesh) could be approached through patterning by one high power patterning layer (likely centrally located depending on the sub/superstrate), two patterning layers spaced by 6 μm, three layers spaced by 4 μm, etc. Even patterning meshes with split layers or grids (a portion of the *xy* patterning at one height and the balance at another) could be envisioned, though designing a simple strategy for identifying scenarios where these would be advantageous may be a difficult problem in its own right.

From these grids, the simulation can proceed via the scheme illustrated in Figure 5-11. More specifically, (1) the target fill map (*Ft-map*, capital letter referring to *large* mesh) is translated into a target deprotection using the fill-to-deprotection spline from Figure 5-13b, with values above and below the fill range being replaced with some safety (5-10%) factor above or below the deprotections corresponding to maximum and minimum fills to allow for some target. This map (*Dt-map*), will serve as the ideal-to-be-achieved; however, the *Ft-map*, being the final desired deliverable, will serve as the comparison for error. From the *Dt-map*, a splined map is generated (*dt-map*) that is the size of the smaller patterning mesh for direct comparison. This map also guarantees that variations in the writing intensity will occur smoothly, minimizing deviations from the desired structure in unpatterned regions. (2) A rough guess for the patterning intensity (*i-map*) is made by assuming that each point in *dt-map* was generated by the corresponding point in the *i-map* and not affected by the surrounding points, but for a time that is

much greater (5-10x) the initial patterning speed (*i.e.* exposure time), which is taken to be a constant for the whole pattern, as varying the speed is more difficult than varying the power. This is a very naïve assumption, but generates a map with the proper trends of a fitted intensity map (hot in high fill areas, cold in low fill areas). (3) From the *i-map* deprotection is calculated at every point in the fill mesh to generate the comparison deprotection map (*D-map*). This is done by considering each point in the *i-map* in turn and using the τ function to determine the starting point for each "bake" and the D function with a new time of the determined time with an additional exposure time added on or:

$$d_{new} = D(\tau(d_{old}, T) + t_{exp}, T) \qquad \textbf{Eq. 5-13}$$

With $d_{\text{old,new}}$ representing the deprotections in the n and $n+1$ step of the history dependent bake. One important observation to make is that, while iterative and constantly heading towards the final point of complete reaction, the order in which the "baking" is applied can change the result. For example, the deprotection, as with many other chemical reactions, occurs most dramatically at deprotection values near zero. For this reason, the low temperature or distant bakes that may have some effect at the *start* of the reaction are likely to have little to no effect near its completion, though they may be useful for fine tuning. Fortunately, the nature of the real experiment informs the order in which the bakes should be considered – namely, in the order in which they occur in the experiment (*i.e.* the order of patterning). For example, indexing through the *i-map* in the following manner ($[x_1,y_1,z_1]$, $[x_2,y_1,z_1]$, …,$[x_i,y_1,z_1]$, …, $[x_1,y_2,z_1]$, …, $[x_i,y_j,z_1]$, …, $[x_i,y_j,z_k]$) is equivalent to patterning in z-layers of x-lines. This example of indexing through the *i-map* also brings up another method for the reduction of computational load, namely, only considering points proximate enough to have some significant effect, which can be determined as a function of temperature and, for more advanced consideration, the current value of the deprotection. For example, if the current deprotection is already greater than the maximum deprotection for a fill of 1, then further bakes need not be considered. (4) The *D-map* is converted by the deprotection-to-fill function into a fitted fill map (*F-map*) which is compared to *Ft-map* to calculate an RMS error. As mentioned earlier, certain values out of the FLaSk-achievable fill bounds are not considered for the purpose of determining

the error. Finally, (5) a new *i-map* is determined from the difference between a *d-map* splined from *D-map* and *dt-map* and steps (3-5) are looped until (6) the simulation ends and delivers its best guess at the *i-map* to arrive at an *F-map* closest to *Ft-map*. The details of how (5) is performed and the conditions for which (6) occurs will now be discussed in detail.

When adjusting the *i-map*, it is obvious that any change should trend with the error in the *dt-map*. In essence, if the region is under-baked, the intensity should be increased, while if it is over-baked, the intensity should be decreased. If the FLaSk spot size were infinitesimally small, changes to the *i-map* proportional to the differences in the two *d-map*s, would rapidly lead to a unique, exact solution (however, the points in between would have no structuring whatsoever). This could be approached in a method analogous to a molecular statics solver, such as:

$$\Delta i = q \cdot ln\left(\frac{d}{d_t}\right) \qquad \textbf{Eq. 5-14}$$

Where q is an empirical solver parameter that defines the size of the correction step such as to not overshoot the solution. Use of a logithmic adjustment is motivated simply by the exponential relation between baking temperature and the resulting deprotection. Within this framework, if a maximum intensity is given, the exposure time (here a global constant as the write speed is harder to modulate than the intensity) may be increased until a solution is found. Similarly, if the intensity called for by Eq. 5-14 is ever negative, it may be set back to zero (as in this simplified situation, it is impossible for zero exposure to be too great).

Of course, the thermal spot possesses finite size and thus, changes to a single point's intensity leads to changes in the surrounding map. This may be corrected for in several ways. As an example, the first correction that was approached follows from recognizing, as before, that the intensity cannot be less than zero. As a result, should a point still be over-baked after reducing the intensity at that point to zero, it is necessary to cool surrounding points, which can be done simply by applying the change from Eq. 5-14 to the surrounding points instead of to the zeroed region. Such a change can propagate through the map

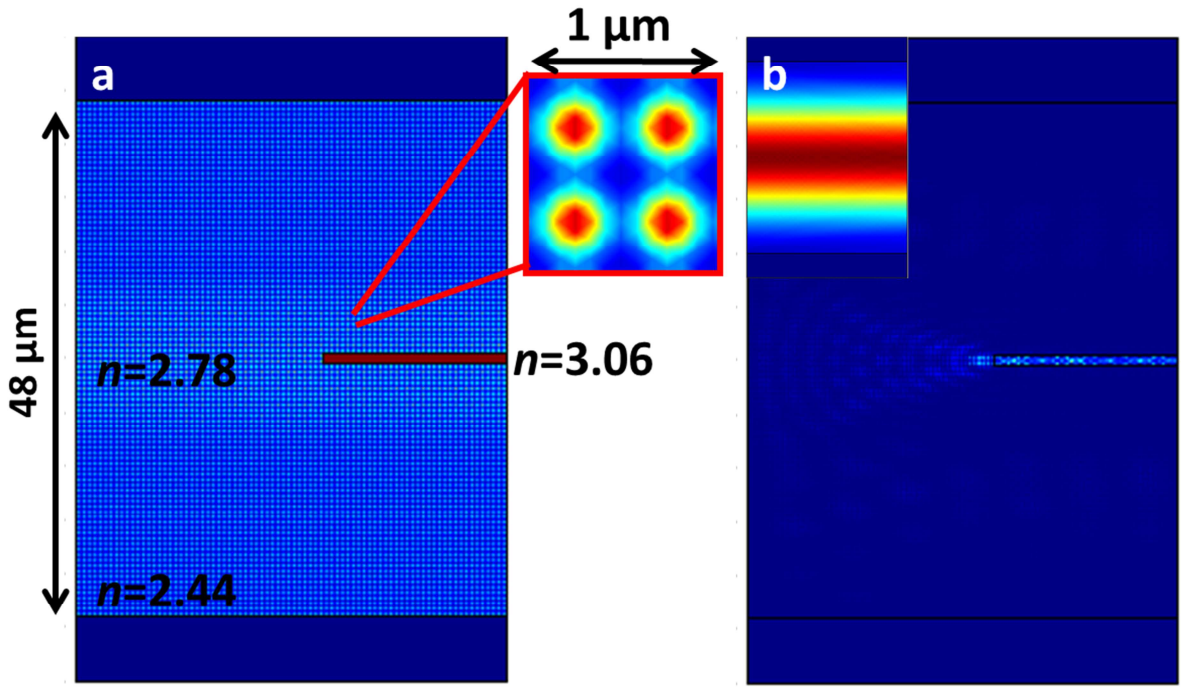

Figure 5-15: 2D EM simulations of a Si GRIN slab with a solid waveguide embedded in it. (a) Index map of the structure, possessing a gradual decrease in index from the center to the edge that is defined by a subwavelength (500 nm) periodic fill pattern. A waveguide of fully solid material is embedded inside of the slab. (b) Electromagnetic simulation of a 1.55 µm wavelength Gaussian beam (inset) propagating through the structure from (a). The GRIN structure creates a periodic array of focal points (not shown) the first of which is coupled into and then trapped within the waveguide with low insertion loss.

resulting, potentially, in a map of all zeros, at w hich point the exposure time can be reduced. A similar method can be approached for every temperature change, since raising the temperature in a poorly fit region will require lowering of the temperatures in an adjacent well fit region. There are several factors to consider in deciding how much to change the temperature. For example, small changes to temperature will mean different things depending on the absolute value of temperature due to a combination of the exponential nature of the baking kinetics (kinetics rapidly increasing with temperature) and the asymptotic nature of the deprotection during bake (changes matter more at low values of deprotection which correspond to lower temperature bakes).

Utilization of Coarse Solver to Fit a Target Structure

The power of both the simulation method and the technique itself is its ability to pattern any given target structure. One area where FLaSk-CAP could find applications is gradient index (GRIN) optics (acoustics), wherein the propagation of light (sound) is manipulated by the utilization of a smoothly varying index (impedance) map. For example, Figure 5-15a shows a 2D simulation of a power-law index distribution[194] within a slab of material generated by a periodic (a=500 nm) index variation of a patterned silicon (n_{max}=3.06) of various fill fractions. The governing equations of this pattern are:

$$n(x,y) = \begin{cases} n_{core}\sqrt{1-2\Delta\rho^{\alpha}} & \rho \le 1 \\ n_{core}\sqrt{1-2\Delta} & \rho > 1 \end{cases} \qquad \textbf{Eq. 5-15}$$

Where $\Delta = (n_{core}^2 - n_{clad}^2)/2n_{core}^2$, $\rho = 2y/rW$, n_{core} and n_{clad} are the maximum and minimum index representing the core and the cladding, r represents the fraction of the waveguide width (W) where the power-law and α represents the sharpness of that transition (α=∞ is a step distribution). Here, n_{core} and n_{clad} were selected as having the indexes corresponding to 0.9 and 1.1 the maximum and minimum fill obtainable by the simulated resist respectively.

When superwavelength light, such as the ubiquitous and technologically relevant 1.55 μm, passes through the slab, it is converted into a periodic array of focal points with period dependent on the specific parameters of the distribution. The advantage of such a distribution in microphotonics is that a waveguide can be positioned at one of these focal points, leading to low loss coupling (Figure 5-15b). This is a promising target structure for FLaSk-CAP as both the gradient structure and the waveguide may be patterned by the integrated DW process. Figure 5-16a-c show the results of conducting the fitting process discussed above on silicon-based (positive tone) 48X15X12 μm GRIN slab handled as being patterned in the middle (4 μm<z<16 μm) of a 25 μm resist film. The fitted cell was extended beyond the structure in two directions (nominally, y and z) to ensure that the termination to unstructured medium could be accomplished, but not in the third (x) direction, which is the direction of propagation. Ostensibly, this direction would terminate in a support or other structure only after being generated at the proper length

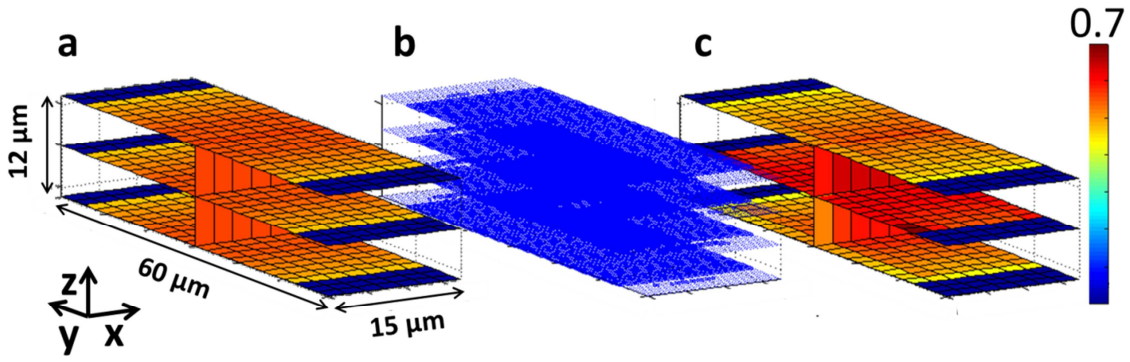

Figure 5-16: Coarse grain fitting of a GRIN structure. (a) The target fill map. (b) The best fit intensity map visualized as dots with radii proportional to the laser intensity. It can be seen that the intensity is simulated on a much finer mesh than the fills. While it is difficult to get intuition about the exact values, it can be seen that the structure of the intensity mimics the target fill. (c) the fitted fill from the simulation. While it follows the general trends of the structure, it clearly struggles to have a uniform *z* profile, which may not be a bad feature for a truly 3D slab device with GRIN in both non-propagating directions.

and therefore, requirements on its patterning may be relaxed. The downside of this is that edge effects will dilute the determination of the accuracy of fitting, which could be corrected by approaching progressively larger and larger length cells. To mimic a typical writing process, the simulated pattern grid was done in three rastered layers. The exposure grid is shown in Figure 5-16b. Despite the unoptimized nature of the solver (beyond the scope of this thesis), a relatively high nearness of fit (average ~15% error for all portions of the structure using a 5 ms per point bake or 100 µm/s) for such a complex process was obtained for these complex structures in around a day with a conventional lab server. This represents a solution volume that is three orders of magnitude greater than the forward-only solution showed in Figure 5-8 at comparable solution time. It should be noted that a *z*-uniform structure is the worst target for FLaSk-CAP, and a profile with a tapered *z* fill would be easier to fit, and possibly create the GRIN effect in both non-propagating directions. Though possibly not as effective as the target slab, it is likely that these resultant structures would similarly result in wavefront focusing and could then be coupled into a 3DDW patterned waveguide.

5.3. *Materials for FLaSk-CAP*

The benefits of FLaSk-CAP in terms of speed of patterning come at the cost of complexity of the technique. Beyond exploration of the patterning parameters, conventional resists are likely not suited for FLaSk annealing for one reason or another. As a large part of this research, the materials for the FLaSk-CAP process were explored, including the resist itself and additives for FLaSk absorption and photoinitiation.

5.3.1. **Resist materials selection**

Being the largest volume fraction component and also accounting for the properties of the final structure, the properties of the resist are critical for the performance of FLaSk. All of the results reported are done with doped SU-8, which was selected due to several desirable qualities that has led to it being the ubiquitous CAR choice for thick film 3D lithography. The most important quality of SU-8 is the fact that it is a small molecule resist with a low melting temperature. This allows for it to be easily spun and processed as a semiflexible film with low stresses and also leads to a high density of functional epoxy groups (eight per molecule). This is not an ideal resist for FLaSk-CAP, however, it is good enough to provide some very important experimental demonstrations. As a result, the use of an optimized resist will likely lead to even more impressive results enabling the realization of the predicted performance from the simulations discussed in 5.2. The greatest drawback of SU-8 as a resist material for FLaSk-CAP is shrinkage.

By the nature of their patterning mechanisms, photoresists almost always undergo some volume change. For example, SU-8 can shrink as much as 40% during patterning.[195] This effect was originally attributed to volume shrinkage during crosslinking, but has lately been revealed as a result of the dissolution of uncrosslinked monomer present in the structure due to the necessity for near-insolubility-threshold patterning caused by maximum 3D IL contrast.[196] Positive tone CAR photoresists, while not

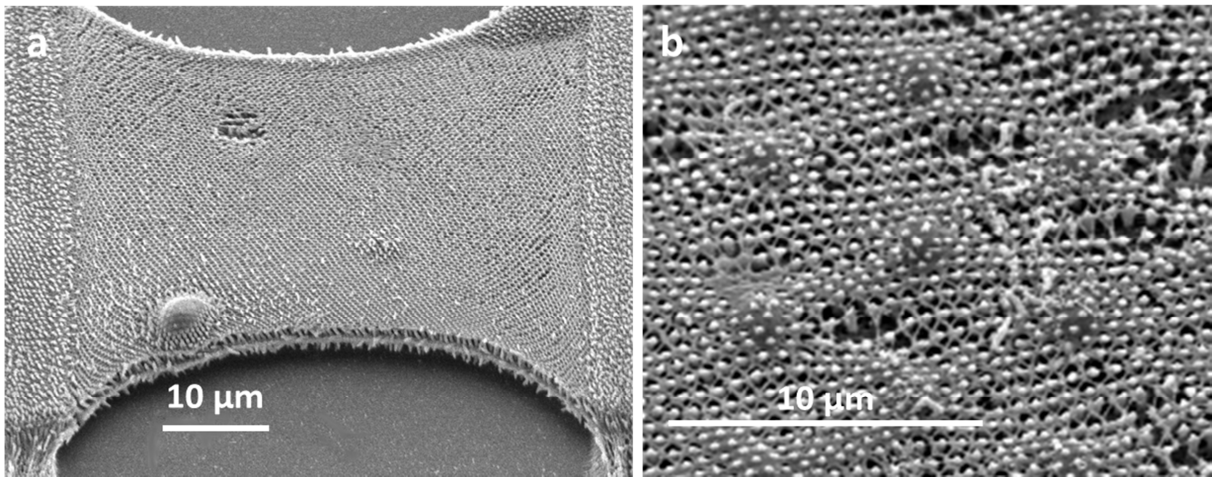

Figure 5-17: Images of shrinkage effects in SU-8 for both large slab structures (a), as can be seen by the macroscopic bowing and around defects (b), where the solid 3DDW point defects cause anisotropic deformation of the surrounding structure.

largely pursued for 3DIL, also undergo shrinkage for a different reason, in that most involve the evolution of some volatile protecting group removed by the PAG.

In broad area IL, the effects of shrinkage are constrained by both the substrate and the surrounding film, leading to *Z* only distortion.[195] It is easy to see why the issue of shrinkage is a much larger issue in a localized patterning process; in FLaSk-CAP, not only is the shrinkage in all three dimensions (lacking the benefit of a confining film), but the ability to tune the baking (thus simultaneously tuning the under-crosslinked resist fraction) leads to non-uniform spatial shrinkage (Figure 5-17a). The latter is made worse by the incorporation of 3DDW defects, which are generally highly exposed and shrink much less (Figure 5-17b). In the case of broad area, one strategy that has been approached for the mitigation of this effect is to incorporate prebias in the pattern itself.[197] It is further clear, because of the spatial non-uniformity in even the single dose case shown in Figure 5-17a, how this would not be an appropriate strategy as different areas shrink to different extents. The second strategy that has been approached for mitigation of shrinkage is by design of the resist, either by utilizing a larger molecular weight polymer[198] or, in the case of SU-8, by removing the fraction of less sensitive, short oligomers.[196] For 3DDW, the incorporation of inorganic colloids or precursors, also an effective means for increasing the mechanical

properties of SU-8,[199] has also been demonstrated as an effective way to lower shrinkage.[200] These are attractive methods for FLaSk-CAP; however, the benefits of an off-the-shelf resist at this stage of technique development are essential and these will have to be investigated in future work.

Another route to minimizing the shrinkage in FLaSk-CAP is to utilize a positive tone CAR. As mentioned above, shrinkage in 3D IL is constrained to *Z* direction by the surrounding film and substrate. If a locally patterned positive tone resist was used, it could be possible to restrain the resist additionally above by the use of an overly-thick resist layer above, provided that 3DDW paths for the development were provided. An additionally attractive aspect of positive tone patterning is the ability to perform "lost wax" inversion, such as has been done for IL structures by sol gel,[201] electrodeposition,[15, 63, 201, 202] low temperature chemical vapor deposition,[45, 203] or protected CVD by atomic layer deposition of alumina.[89, 119, 196, 203] In this way, a non-polymeric material with added functionality can take on the inverse structure of the polymer (now template). For example, inversion could be done with a higher index of refraction material to introduce 3D bandgaps.[203] After infiltration, the remaining CAR could be removed via a flood exposure. Unfortunately, positive tone resists have only been applied to 3DDW for 3D fabrication,[204, 205] and even then with relatively poor resolution inappropriate for 3DIL. This is contrary to the demonstrated performance of positive tone resists, which are ubiquitous in high resolution DUV lithography.[206] This is likely the result of deliberate lowering of the activation energy of the resist utilized to avoid the largest challenge facing use of positive tone resists to IL, which is the development and subsequent foaming of volatile agents produced during the deprotection of the positive tone resists. By lowering the energy, a lower PEB could be utilized leading to less violent evolution of the volatiles. I have subsequently shown that this can also be accomplished with the submicron resolution more typical of 3DDW with a more conventional ESCAP photoresist by increasing the 3DDW dose and lowering and lengthening the PEB temperature (7.2); however, this is of limited use in considering the rapid bake process of FLaSk-CAP.

The next logical step is to approach positive tone CARs that possess high boiling point volatile protection groups or no protection groups at all. The latter case is generally referred to as a mass-

persistant photoresist and is surprisingly uncommon. In fact, the only reference to mass persistent resists appears to be in the preliminary, unpublished research of Prof. Grant Wilson at University of Texas-Austin. This research was not pursued due to low resolutions; however, it may have been appropriate for FLaSk-CAP. The former case is in fact present in the current cutting edge of ultra-high resolution thin film resists based on adamantyl meth/acrylate random copolymers.[153, 207-209] The adamantyl protection groups possess sublimation temperatures around 200 ºC. Several adamantyl resists were synthesized or obtained for evaluation as possible FLaSk-CAP resists; however, as the name implies, they were found too rigid to survive as thick film resists. More specifically, cracks would either develop during preexposure baking or during development leading to catastrophic failure of the films. It is still possible that an adamantyl positive tone system will be possible for 3DIL and thereby FLaSk-CAP, but this will require considerable development to lower the rigidity of the copolymer while maintaining its other desirable properties.

5.3.2. **FLaSk dye materials selection**

As the main differentiation between conventional DW lithography and FLaSk is the presence of an absorbing dye or pigment, this component of the resist has not previously been a design consideration. It should be noted that it is possible to not employ an additional dopant and use the intrinsic thermal absorption of the resist. Due to high-intensity breakdown crosslinking,[60, 61] the use of a specific thermal absorption band is necessary.

Table 5-3: Some of the photoactive media explored and their reason for exclusion

Photoactive Media	Incompatibility
Bisimides	Transparency in the UV too low
Rhodamine, Coumarin	Absorption too near to DW wavelengths
Anthracenes	High photobleaching
Cyananines, Malachite, oxybutyl phthalocyanines	High thermochemical bleaching
Alexa, Squaraine	Too great a fluorescence quantum yield
Nitrates, Phthalocyanines	Low solubility in resist
Porpherines	Electron transfer with photoinitiator
Nanoparticles	Too large for uniform patterning

For example, SU-8 possesses absorption bands at 1.7, 2.4, and 2.9 μm.[60] At these wavelengths, resolution (especially in the *Z*) is quite low and further optics become more complicated. In future, these bands may be useful in any application where 3D patterning is not critical. Barring these bands, to implement proper materials selection of the photoabsorbing dye, a set of criteria must be developed. A table of some of the evaluated dyes and the reasons for their incompatibility are listed in Table 5-3. The critical issues are: absorption band position, electron transfer, solubility, and stability (optical, thermal, and chemical). Solubility is a critically important factor, but is understandable enough not to merit further specific discussion. Similarly simple, electron transfer is the equivalent of incorporating an additional visible photoinitiator. For example, 2,7,12,17-Tetra-*tert*-butyl-5,10,15,20-tetraaza-21*H*,23*H*-porphine, would satisfy all other requirements except that it transfers electrons to the photoinitiator as observed both by resulting crosslinking. This observation is consistent with the utilization of porphyrin in solar applications.[210]

Absorption band position

FLaSk-CAP is a hybrid lithographic strategy involving multiple exposure steps and methods (*i.e.* IL, FLaSk, and 3DDW). Since 3DDW generally involves nonlinear multiple photon activation of the same band as the IL, the absorption band positions of these two lithographic steps are generally non-interfering. These exposure regimes, however, do set limits on what colors can be used for the FLaSk excitation dye. Since the IL step generally requires UV or near UV exposure, this limits FLaSk to visible or IR light. The 3DDW in most cases is performed with NIR, the implications of using CW NIR for FLaSk will be

discussed below as this was utilized many of the FLaSk experiments. Combining these criteria, along with the desire for as high a resolution as possible, leads to visible light from red through green to be the best selection. To make matters more complicated, it was demonstrated that CW visible light of sufficient intensity could non-linearly activate UV photoinitiators directly by multiphoton absorption.[59] Even very high intensity (>1 TW/cm^2) NIR CW light can cause direct dielectric breakdown.[60, 61] Because of this, there is a limit to the intensity that can be employed for FLaSk at any given wavelength, but especially for energies in the green and above, ostensibly due to the massive absorption of most UV photoinitiators at ~200 nm.

The one advantage to this is that green light can be instead utilized for the IL exposure, thus avoiding UV bleaching that most materials undergo. This additionally allows for overdoping of an MPL initiator. This is advantageous as it reduces the threshold for 3DDW, which can be especially high in the absence of a PEB, and lowers the chances of LID already enhanced by the presence of additional additives. The most frequently utilized 3DDW initiator here is ITX, selected for its high two photon cross-section[211] and low chemical bleaching. In the cases where green IL was performed, HNu 470 (Spectra Group Ltd.) was utilized as the photoinitiator. HNu 470 is a deliberately bleaching initiator compound with the aim to allow for uniform exposure through high thickness resists. This was not viewed as a problem, but the bleaching agents in the HNu 470 may interact with heat-producing dyes and may therefore need to be investigated and possibly removed in future.

Using the same band for both 3DDW and FLaSk is an attractive option due to the possibility of using the same laser for both steps (as is possible with the RegA Ti:Sapphire system used for many of the experiments discussed here), as it trivializes considerations such as power modulation and beam coincidence. There are some drawbacks to this selection. Most obviously, it diminishes the depth uniformity of 3DDW since the beam intensity will decay through the thickness in the typical linear manner, though this is minimized already as a part of the tolerances for the FLaSk heating. The next disadvantage is bleaching of the FLaSk dye. While there is always some change in the optical properties

after 3DDW, when the same band is used the dye at the focal point is exposed to massive doses of absorbed light and is almost always completely degraded. This is not a problem for non-functional supports, but defects such as waveguides or corrections to the density need to not change the properties of subsequently written surrounding lattice, correctable by doing 3DDW after the FLaSk (desirable anyway when different bands are used). There are other differences that occur from doing the 3DDW before or after, as should be expected from performing 3DDW with and without PEB. The last consideration was whether or not heating would be caused by the pulse laser during 3DDW. This issue was raised by initial results which indicated a high line edge roughness (LER) on 3DDW lines due to the appearance of IL structuring. It was hypothesized, however, that dye heating was likely not the source of this LIR due to the fact that the intensity for 3DDW (5-20 mW) was much less than the typical FLaSk intensity (30-120 mW) combined with an expected reduction on optical heating from pulsed lasers.[212] This problem had a different source (likely bleaching) and was greatly reduced by modifying the IL parameters as will be discussed in 5.4.4.

Bleaching

The term "bleaching" is used here in the most general sense, namely, any change in the thermal absorption of the net resist system (dye-initiator-polymer) upon exposure to some stimulus. This is distinct from a change in the total absorption as bleaching pathways can involve elimination of fluorescent pathways in the excitation of a dye. As a result, while the fluorescence would be bleached, the *thermal* absorption would actually increase as a greater percentage of the absorbed light would dissipate via thermal means. Further, bleaching may involve a redistribution of the absorption spectrum, such that a given wavelength's absorption may change more significantly then other regions. There are three distinct ways that bleaching can occur during the FLaSk-CAP process: optical (photobleaching), thermal, and chemical. Any or all of these may occur to different extents in a given compound with a different final effect on the patterning.

Photobleaching is fairly ubiquitous and can be described as electrical excitation of the photoactive molecule causing transformation of the compound into a degraded state rather than generating a photon or phonon.[213] In general, the greater the absorption and absorbed intensity at a given wavelength, the greater the chance for photobleaching. The effects of photobleaching on FLaSK-CAP depend on which component undergoes bleaching. If, for example, the dye that is being utilized as the thermal source undergoes bleaching during the IL exposure, the overall effect can be expected to be relatively minimal. The reason for this being that the FLaSk heating spot is ideally superwavelength with respect to the IL structuring, and as a result, the bleached pattern would potentially act as an effective weighted medium, with the fine heating structure blurred by thermal conductivity effects. On the other hand, if the photoinitiator incorporated for 3DDW undergoes photobleaching, the result will be much more undesirable. This is, in fact, the case for the ITX utilized as a UV sensitizer strongly bleaches under UV/blue exposure. Because of this, when ITX is exposed to UV-IL, a latent pattern of bleached initiator is formed in an analogous, but inverse, manner as the latent photoacid image that is produced by the desired IL mechanism in the PAG. During the 3DDW process, this inverted IL image will prevent the excitation of those regions of the polymer at the same threshold dose as the unexposed regions, and, in contrast to the thermal effects, this direct exposure process has no blurring mechanism. The result is that the patterned lines can be expected to possess some inverse bias. At the same time, in the case of ITX, the IL process also appears to release heat locally due to absorption and decomposition from the excitation source, causing a counter driving of the reaction in the bleached region. The net result was that when the FLaSk-CAP films were patterned with blue or UV IL, the 3DDW structures would possess similar structuring as the FLaSk written lines (as will be shown in Figure 5-27), though with a mostly solid structure meaning that this could not be viewed as a higher resolution alternative to FLaSk patterning. While it may seem that this is merely the effect of the overlapping doses of the 3DDW and the IL generating their union in the final structure (as is the conventional wisdom regarding preexposure in 3DDW),[214] this is likely not the case due to the threshold for 3DDW *without* a post bake being much higher than that with, such that the IL exposure is only a small fraction of the dose needed. Supporting

this reasoning is the fact that the patterning roughness in the 3DDW lines could be prevented by using IL-excitation that did not bleach the ITX (Figure 5-18). In such cases, as will be discussed in 5.4.2, the line width of 3DDW lines was actually observed to *reduce*, consistent with IL bleaching excitation with only limited heat release.

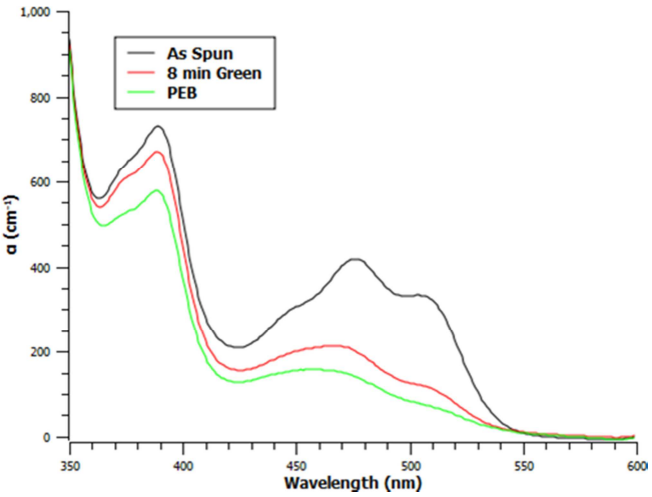

Figure 5-18: Absorption plots from UV-Vis analysis of the standard photoinitiator setup (0.5 wt% ITX, 0.25 wt% HNu 470, and 2.5% OPPI) employed for later FLaSk-CAP experiments before exposure (black), after 8 minutes green flood exposure (red), and PEB (green). While the total absorption in the UV (due mainly to the ITX) lowers, it is most likely due to bleaching of the HNu signal (predominantly in green and blue). As a result, it is not expected that the MPL absorption (much higher for the ITX than the HNu) is affected.

Thermal bleaching, also quite common, is the alteration of the absorptive properties of the resist under thermal excitation. Fortunately, this was not observed to be a large problem for systems employed in this study, as the only dye investigated which possessed considerable thermal bleaching was identified during preexposure bake and was therefore removed from consideration; however, the expected effects of a thermally bleaching dye could be expected to initiate the so called "hot line" effect that also occurs for chemical bleaching and was discussed in 5.2. More specifically, if the tail of the thermal profile bleaches subsequent direct thermal exposures, the result will be that the first line patterned in a raster will always be the hottest/most reacted.

Chemical bleaching is where some chemical reaction results in the change in absorption of the dye. The first way that this can occur is simply by introduction into solution. This was observed for oxidizing metal phthalocyanines (Pc), such as copper (Cu)Pc and iron Pc, which changed color gradually in solution over the span of a few days to weeks. While this was intractable for the long time use, solutions for any

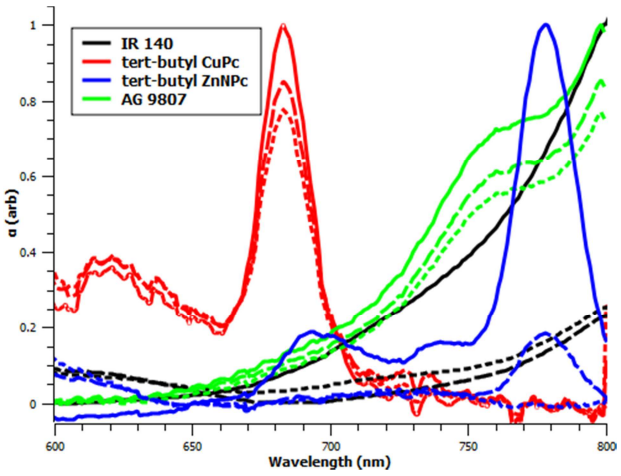

Figure 5-19: Normalized absorption plots for resists utilized (chronologically) before exposure (solid), after exposure (long dash) and after PEB (short dash): IR 140 (black, abandoned for reactivity), tert-butyl CuPc (red, solubility issues), tert-butyl ZnNPc (blue, bleaching issues), and AG 9807 (green).

given single use can be relatively stable. More relevant to the FLaSk-CAP process is reactions that occur after exposure. To a large extent, these were driven by the introduction of a strong acid into the system by the PAG on exposure. For example, any stabilized Pc containing oxygen bound functional groups (such as the highly soluable oxybutyl-Pcs) underwent large changes in their absorption spectrum upon excitation as that functional group is apparently attacked by the acid. This is particularly problematic for FLaSk-CAP patterning as the acid bleaching, much as acid crosslinking, is a kinetic process, leading to a similar "hot line" effect as a thermal bleaching compound. Unlike thermal bleaching, however, compounds that undergo post-exposure chemical bleaching are much more numerous. Furthermore, compounds that do not undergo chemical bleaching often do not do so because their solubility is low.

Having identified the possible routes to bleaching, an ideal resist, barring one which undergoes no bleaching at all, is one that instead undergoes minimal bleaching at the FLaSk wavelength and, further, undergoes the largest part of its bleaching during IL exposure (photobleaching). Plots of absorption before and after exposure and after baking normalized by the largest absorption in the plot are shown for the resists utilized in Figure 5-19. The better performing resists are Pc based, but possess different metal functional groups and solubilizing functional groups. The best performing systems (*e.g.* Cu) unfortunately are often the least soluable, preventing their use. One advantage to all Pc systems, though, was the fact that they possess exceedingly high photoactivities, requiring only sub-tenth weight percent doping. In this

way, even when chemical bleaching occurred, it could be expected not to greatly leach the photoacids. As dye selection was ongoing, several systems were employed with varying efficacy.

5.4. *Experimental realization of FLaSk-CAP*

5.4.1. **Experimental parameters**

In the development of FLaSk-CAP, being a completely new technique, it was necessary to develop both the materials and processing as new observations about the system behavior were made. As a result, various combinations of beam, dye, and photoinitiator parameters were utilized.

Sample preparation

In all cases, samples were prepared in a three-step process and utilized SU-8 (MicroChem Corp.) as a resist material. The first step consisted of spinning a layer of as-received SU-8 5-15 μm thick and then flood crosslinked through the usual process with a UV lamp and hotplate. The purpose of this layer was to act doubly act as an adhesion layer and also as a thermal spacer to diminish the effects discussed in 5.2.2. Then the FLaSk-CAP resist was spun on to obtain desired thickness (generally 10 μm) and pre-exposure baked for 5-30 mins. Finally, a PDMS phase mask was placed into contact with the resist surface (or in the case of tert-butyl CuPc, an additional PS sacrificial mask as described in 2.3.4, to prevent surface aggregation) and heated to 95 ºC for ~30 sec to affect capillarity-induced nanoimprint. Once the sample was brought to room temperature and the mask removed, the surface-imprinted sample was ready for processing. This was accomplished by first performing the IL exposure and then performing FLaSk-CAP in the following order for a given pattern: (1) 3DDW supports, (2) FLaSk, and (3) 3DDW defects. The reasoning for this was that since 3DDW was universally observed to bleach the dyes utilized for FLaSk, 3DDW features ideally should be patterned as the last step; however, the 3DDW supports also benefitted from the additional PEB, thus lowering the chances that the samples would detach during development. Samples were moved to the development step within ~1 hr after initiation of IL exposure to limit additional room temperature crosslinking. Sample development was done by immersion in PGMEA for 20-30 min, followed by immediate dipping in isopropyl alcohol (IPA) to rinse the PGMEA and

development biproducts. IPA doubly serves to rinse to act as a lower surface tension solvent to limit the capillarity induced collapse of the written structures. An additional solvent exchange is sometimes employed to further limit capillarity effects.[215, 216] Here, dipping in hexamethyldisilazane (HMDS) was used to replace the IPA with an even lower surface tension solvent before drying with compressed air, as previously utilized in MPL post-processing.[216]

PMIL Masks and Exposure Sources

The PMIL utilized for FLaSk went through three major stages during the course of this research. The first system utilized was laser L-355, which was a pulse laser with nominal power of 300-400 mW where the dose could be controlled by the number for 10 Hz pulses allowed through the shutter. This system was abandoned for several reasons, the largest being the practical one of the long term instability of the laser itself. The replacement UV sources utilized were two high intensity (300-500 mW) LED lamps, one at 365 nm and one at 405 nm. Here dose was controlled by exposure time. These had the added benefit of being unpolarized, thus leading to no field-direction dependent effects.

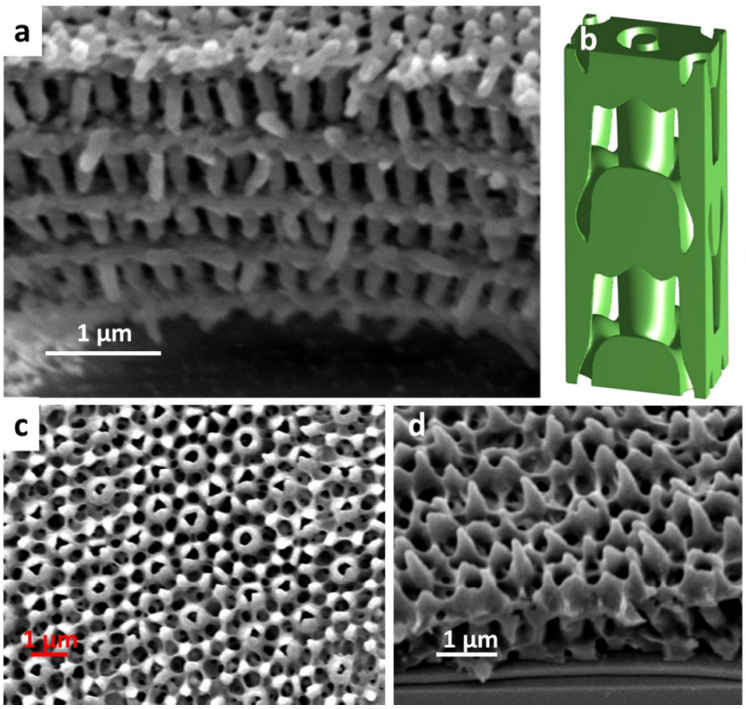

Figure 5-20: Employed PMIL structures. (a) Side view of p6mm IL structure produced with a UV exposure through the 600 nm imprint along with the simulated EM distribution (b, courtesy of Lin Jia). (c) Top down and side view (d) of (quasi-)quasicrystalline IL structure produced with green light through a quasicrystalline imprint.

For these UV systems the photomask imprint that was utilized was a triangular lattice of 250 nm tall pillars with 120 nm radius and 600 nm pitch (referred to as the p6mm pattern due to its symmetry). Images of the simulated structures produced from this mask along with the resulting experimental structures from large area IL using are shown in Figure 5-20a,b. The geometry of the IL structures consisted of tetragonal arrangements of (approximately) layers of pillars and layers of spheres. Due to the Talbot effect (Eq. 5-10), the spacing of the layers and thereby the height of the pillars varied, shortening from a height of ~1.4 µm to ~1 µm as the wavelength of the light approached the mask periodicity.

Eventually, UV sources were abandoned for FLaSk-CAP due to bleaching effects in favor of green ones. The increase of wavelength brings with it an unavoidable reduction in resolution. This is not necessarily an insoluable problem as dyes that do not bleach in (at least) long-wave UV excitation exist; however, the additional optimization, in light of the already large number of necessary materials

properties outlined in 5.3, is highly undesirable in the short term. For green excitation laser C-532 was utilized with a power level of ~2.4 $W \cdot cm^{-2}$. Once again, dose was controlled by exposure time. The circular polarization of this source had a somewhat similar effect as the unpolarized LED lamp sources, and further the high intensity allowed for lower initiator doping leading to higher exposure uniformity.

At this stage of development it was found that the p6mm mask described above possessed too close a packing of features when exposed at 532 nm, such that FLaSk-CAP always led to fully densified structures lacking in solvent paths for development. For this reason, a different mask had to be used. To both allow for larger solvent access and also to demonstrate some of the full potential of FLaSk-CAP to create otherwise impractical hierarchical architectures, a quasicrystalline mask was employed possessing 10-fold symmetry, a minimum feature-to-feature spacing of ~1.3 μm, and an imprint height of ~500 nm. Large area IL of this pattern is shown in Figure 5-20c,d. It should be noted that as the Talbot effect applies to this structure as well, it is only strictly quasiperiodic in 2D.

Initiators and Dyes Utilized

The first generation of experiments performed utilized the UV absorption of intrinsic SU-8 to perform both the IL and 3DDW step. For the latter, however, very high 3DDW doses (~30 mW) were necessary for definition of supports for the FLaSk written structures, greatly increasing the chance of LID. To alleviate this, ITX was added as a photoinitator, but it generally had to be overdoped due to UV bleaching. A problem that was later removed by switching to green excitation. To enable green excitation at reasonable doses, HNu 470, often with additional OPPI (Spectra Group Ltd.) PAG in a 1:10 ratio was added to resists.

In the first generation of experiments, NIR absorption was introduced by addition of 5,5′-Dichloro-11-diphenylamino-3,3′-diethyl-10,12-ethylenethiatricarbocyanine perchlorate (IR-140) dye (Exciton). This dye was selected for its relative compatibility with SU-8, being both soluble in cyclopentanone (the carrier solvent of the SU-8 2000 series) and shelf-stable with the photochemicals. In addition, IR-140,

despite being a laser dye, has a relatively low quantum yield (<10%[217]), and thus a relatively high thermal absorption. That being said, IR 140 suffered from massive chemical bleaching, such that it had to be overdoped significantly to maintain necessary absorption during the FLaSk exposures for anything but the first line. Despite this, many of the initial demonstrations of the capabilities of FLaSk-CAP were done with this dye system, and, in fact, it turns out that the speed of the technique was enhanced by using a bleaching dye, though this is probably not an exploitable feature. Later experiments utilized a series of metal phthalocyanine dyes, first tert-butyl CuPc (low bleaching, low solubility) with red excitation, then tert-butyl Zn napthalocyanine (NPc) (high solubility, medium bleaching), and finally AG 9807 (Adam Gates CO., high solubility, low bleaching), a proprietary linear polyPc dye for laser safety goggles. Absorption plots for these dyes can be found in Figure 5-19.

5.4.2. **FLaSk-CAP patterning threshold**

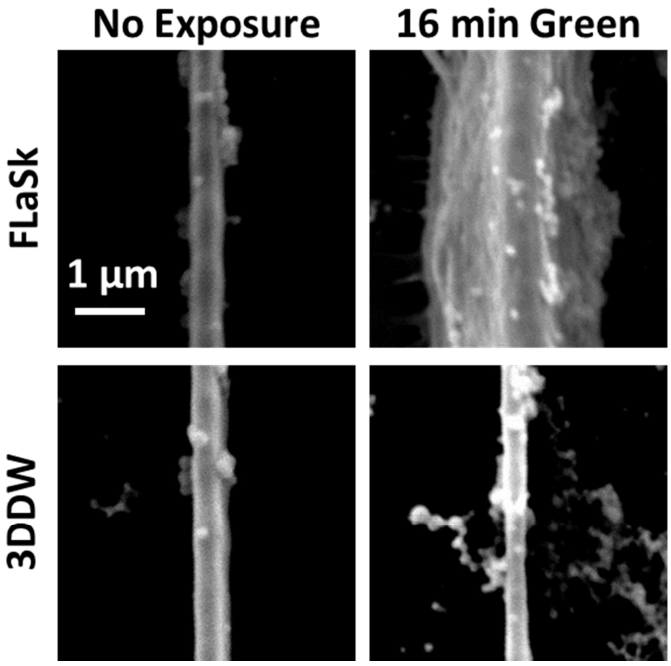

Figure 5-21: Lines written by FLaSk (105 mW) and 3DDW (10 mW) at 100 µm/s with and without 16 minutes of flood green exposure. The FLaSk line can be observed to largely expand after exposure indicating the FLaSk-CAP process, but the core of the solid line still persists due to direct breakdown.

The first important step (logically if not chronologically) in demonstrating the feasibility of FLaSk is to prove that it is in fact possible to thermally crosslink pre-exposed photoresist by utilizing writing parameters that do not crosslink *un*exposed resist. The reasoning for this is that all PAGs are susceptible to purely thermal activation, and, as the temperatures utilized in FLaSk are elevated from the standpoint of conventional PEB, it is possible that any observed structuring was purely by thermal effects or even by non-linear 3DDW of the resist by multiple absorption of the FLaSk excitation light.[59] There is already precedent for this not being the case from earlier LSA baking studies;[153] however, the timescales involved in LSA are shorter than those in 3D FLaSk. To test the mechanism, line arrays written at 100 µm/sec in samples of a green FLaSk resist (0.5 wt% ITX, 0.45 wt% HNu 470, 0.034 wt% tert-butyl ZnNPc) were patterned into resist

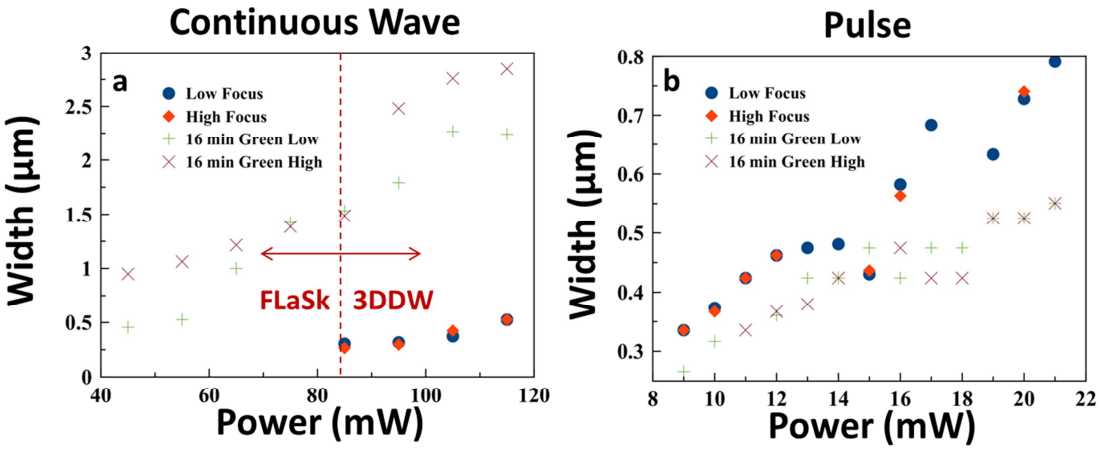

Figure 5-22: Line widths of lines patterned by FLaSk (a, CW) and 3DDW (b, pulse) before and after green exposure for two focuses in the resist 3 µm above the substrate (low) and 8 µm above the substrate (high). For the FLaSk lines, direct write is possible over a threshold (marked with the dashed line, where FLaSk-CAP will not be able to give open structures), but below that threshold, FLaSk-CAP is possible. For the 3DDW, the line width decreases slightly with exposure, but is relatively unaffected.

with and without prior green flood exposure (Figure 5-21, with analysis in Figure 5-22). This was done for both pulse and CW IR light with laser L-780P-O_1.3-AOM and L-780CW-O_1.3-AOM to simultaneously also observe the effects of the flood exposure on the lines written by non-linear 3DDW using a different absorption band (*i.e.* the crosstalk due to sharing a PAG). Finally, to elucidate the importance of focus on the effective resist thermal properties as discussed in 5.2.2, the arrays were patterned at two different focuses (3 and 8 µm above the 10 µm film's substrate). From these results, it can be clearly seen that the CW exposure alone can be sufficient (here at doses >80 mW) to initiate direct crosslinking; however, with green excitation, the threshold for pattern formation drops simultaneously as the line width also significantly (2-3x) increases. At the same time the overall shape of the lines changes from a DW ellipsoidal voxel to a broader, rougher profile similar to those predicted in the radial simulations shown in Figure 5-5c. In comparing the two focuses it can also be seen that, with preexposure, there is a general trend for a wider structure at the higher focus; however, the differences are not very

large near the onset of the DW crossover, which is actually also consistent with the prediction of an insulating air top interface (leading to a persistence of the tail of the exposure near the surface) with the differences being more clear in the actual images rather than the line width (projected) data.

While it is certain that the predicted FLaSk mechanism is occurring for the exposed sample both above and below the DW threshold, it is somewhat unclear what the mechanism of the DW lines is. The line width did not depend on the focal position, which should (in the least) have some effect on the temperature at the focal point, suggesting a non-thermal mechanism. Further, the line width is subwavelength, more consistent with a non-linear 3DDW process. On the other hand, these intensities should be well below the amount of light necessary to initiate direct breakdown, suggesting that it could potentially be some sort of ion transfer mechanism such as was observed with porphyrin-based (structurally related to Pc) dyes. Supporting a thermal mechanism, however, is the step increase in the width of lines with exposure upon crossing the DW threshold. This indicates a step increase in the amount of thermal energy present while writing the line, such as would be released during the simultaneous exothermic activation of the PAG groups in the resist (roughly 5 wt% in SU-8).

In examining the 3DDW results from the pulsed laser system, it can be seen that, as expected, there is not significant dependence on the focal position in the film. There is some change in the line width with green exposure; however, it favors smaller lines. This is consistent with the interpretation that the bleaching effect on the combined ITX-Hnu 470 initiator is greater than whatever effect the presence of some activated photoacids in the resist due to the massive localized energy necessary to perform 3DDW without a PEB.

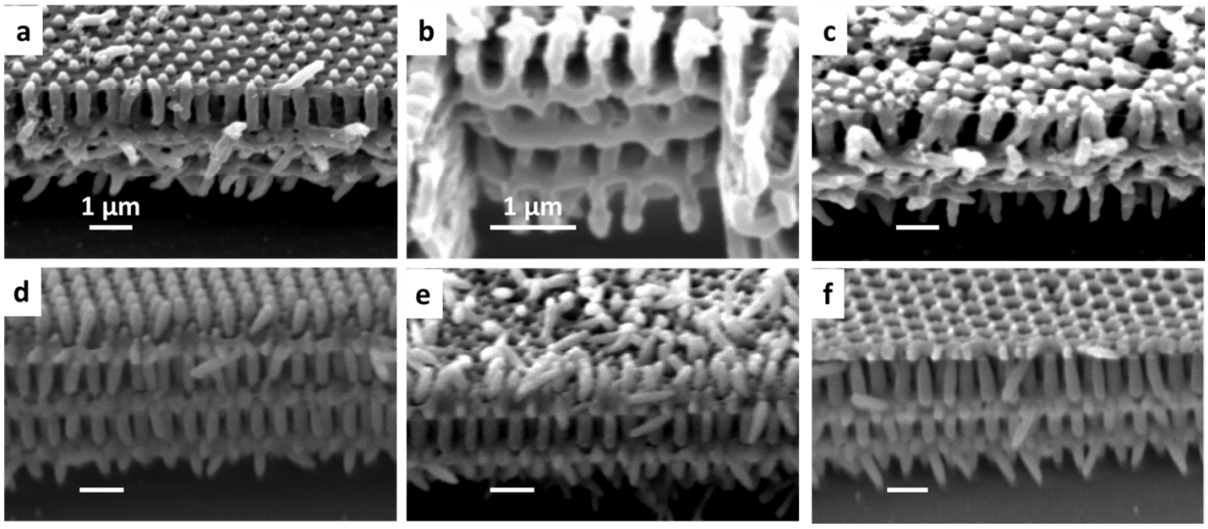

Figure 5-23: UV FLaSk-CAP blocks patterned at 100 µm/s in two different doped resist formulations: one based on IR 140 ((a). 65 mW, (b). 55 mW, and (c). 45 mW) and one based on tert-butyl ZnPc ((d). 90 mW, (e). 75 mW, and (f). 60 mW). Cylinder size can be seen to reduce with lower power and the structure persists into the bulk (as observed by FIB, (b)). Structuring in the Zn resist, with lesser bleaching is observed to be a higher quality.

5.4.3. **Patterning hierarchical structures with FLaSk-CAP**

The main advantage of the FLaSk technique is the local heirarchical patterning of 3D structures from IL prepatterns. As a test pattern, 10 µm blocks written with a 500 nm raster were utilized to ensure that the crosslinked regions from consecutive exposures would overlap. Figure 5-23 shows blocks written at center focus for various powers with the p6mm mask for two resist systems: 0.11 wt% IR 140 (patterned with L-780CW-O_1.3-ND) and 0.025 wt% tert-butyl ZnNPc, 0.125 wt% ITX (patterned with L-780CW-O_1.3-AOM). Both these sets of structures are supported on the edges by 3DDW supports which extend through the thickness of the resist. Progression from disconnected or collapsing structures to solid 3D ones can be observed as FLaSk power is increased. Structural evolution occurred both in the height of the structure, with the lower power structures not including the bottom layer, and the diameter of the rods, progressing from ~240 to ~300 nm. This indicates both a lowering in the spatial extent of crosslinking and also the duration of the effective bake and final structure size. SEM imaging of side views and FIB

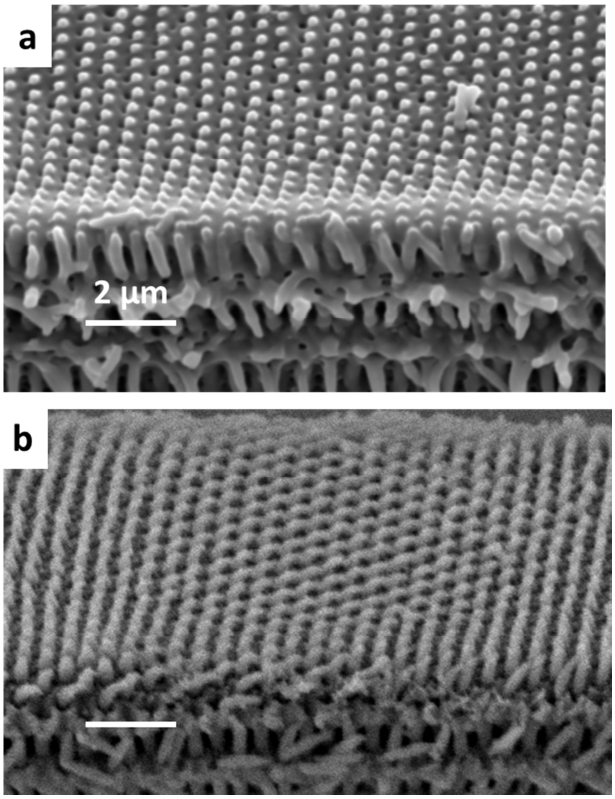

Figure 5-24: Hot line effect. Bleaching of photoabsorber causes a large ridge on the first line pass. IR 140 (a) is strongly bleaching and thus has a large hot line ridge, while tert-butyl CuPd (b) has very little bleaching and only shows a thermal expansion ridge.

cross-sections indicate that the 3D structure extends into the bulk and is the pattern prescribed by the phase mask.

One unfortunate feature is that the base of the pattern is distorted. This is due to considerable shrinkage of the FLaSk blocks – the blocks are patterned to be 10 μm in width, but, the actual sizes are closer to 7 μm. At the junction between the 3DDW and the FLaSk tapers out to a ~9.5 μm, which is more appropriate for solid SU-8 shrinkage. This amounts to a ~30% shrinkage in the unpinned direction, consistent with the ~8-50% volume shrinkage that has been reported in structured SU-8 from combined crosslinking and capillarity effects.[68, 197, 218] Shrinkage out of the plane of the sample is not as severe, because of the planar-like nature of this particular IL distribution.

Another notable feature of the FLaSk blocks is the higher fill fraction of the first side wall, as can be seen by the high contrast ridges on the top side of the blocks in Figure 5-24. This is the "hot line" effect from the bleaching of the FLaSk dye. It can be observed to be much worse for the IR 140 structures and can be minimized by approaching even less bleaching dyes, such as tert-butyl CuPc (0.05 wt%, 0.125 wt% ITX, patterned with L-660CW-O_1.3-O). It does not, however, completely go away due to the "hot ridge" effect, which leads to the first line always possessing some extra height. This is due to thermal expansion during patterning,[196] where the first line expands as it simultaneously crosslinks. Similar to the hot line effect, the hot ridge doesn't occur as strongly in subsequent lines, partially crosslinked by the tails of the thermal profile. A proposed solution to this is to globally simulate the heating tail by applying a pre-FLaSk bake step, and it was observed that bakes of up to 313 K for 1 minute could occur without structuring. This could potentially also lower the amount of heating that need be done by the FLaSk step and should be readily integrable into simulations.

Another interesting comparison between IR 140 and other dyes is the extent to which IR 140 patterns contain more layers, with the Zn dye structures going to a single pillar layer at lower powers. This likely has to do with the simultaneous large bleaching during writing, where the lower layers are artificially heated by the unbleached dye before the full intensity can reach the focal point. This can actually be viewed as a beneficial effect in a patterning technique where the patterning advantage is the ability to write multiple structures in a single line and resolution is not always the target. It is not, however, easily controlled and

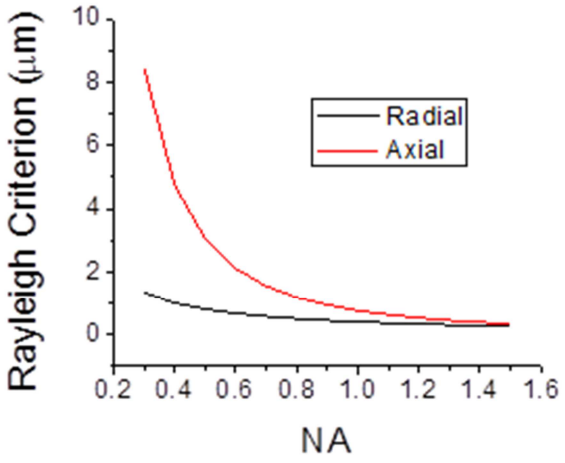

Figure 5-25: Ralyiegh criterion for various numerical apertures of 660 nm light for the radial (black) and axial (red) spot size.

could also be achieved by lowering the NA, which expands the axial spot size at a much faster rate than the radial (Figure 5-25). One last observation is the fact that structures are observed more often to not contain the bottom layer rather than the top. This is consistent with the thermal simulations from 5.2.2 and could potentially be corrected by also doping the adhesion/thermal buffer layer. From the standpoint of optical/acoustic devices, this may be an advantage as it results in slab structures isolated from the substrate, thus minimizing coupling of guided modes. If these structures were made by a layer-by-layer technique, the fabrication of such slabs would require an additional undercut that somehow avoided the supports.

As mentioned above, quasicrystalline patterns were also utilized. It is important to note that while the above tetragonal structures possess some patterning advantage over 3DDW, their structures could be easily reproduced in key features by using a two exposure repeat unit tiled over space (one single exposure for the pillar and one lower power single exposure to simulate the middle layer by crosslinking the pillar-to-pillar gap). In contrast, the quasicrystalline pattern above (Figure 5-20b) represents a massive step up in complexity – possessing a non-tileable pattern with many sub-repeat channels and features. This is not an academic advantage either as quasicrystalline patterns have been demonstrated to possess, for example, highly desirable phononic and photonic properties.[219-221] While this structure is not strictly a 3D quasicrystal, it is a quasicrystal in any 2D plane, and true 3D quasicrystals can be fabricated by MBIL.[222, 223] Figure 5-26 shows quasicrystalline blocks patterned in resist (0.5 wt% ITX, 0.45 wt% HNu 470, 0.034 wt% tert-butyl ZnNPc, patterned with laser L-780CW-O_1.3-AOM) exposed with green light for 6 minutes. It can be seen that the same ability to tune the extent and fill of the structures can be applied to the quasicrystalline pattern.

5.4.4. **Integrated FLaSk-CAP and 3DDW**

In discussing the combination of FLaSk-CAP and 3DDW, the first obvious structure to consider is the aforementioned supports. Due to the substrate-avoidance demonstrated by FLaSk-CAP patterning, the

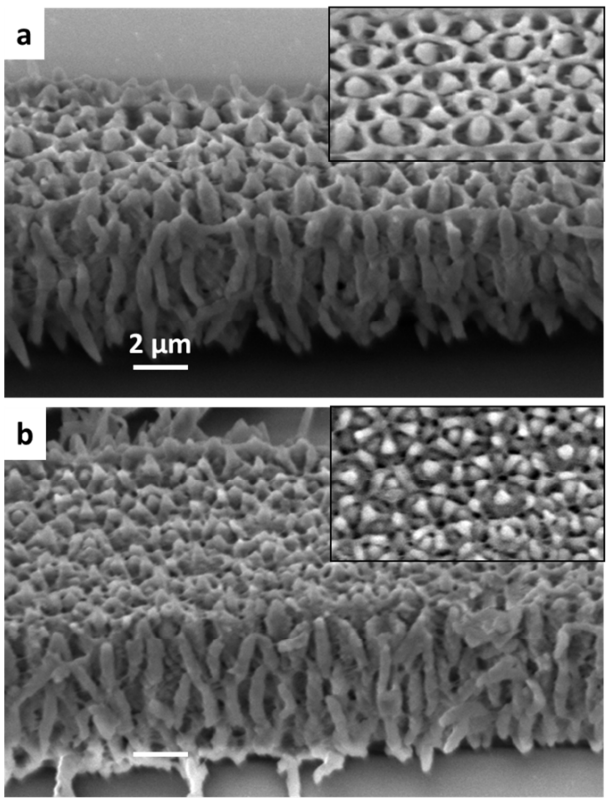

Figure 5-26: Side and top (inset) quasicrystalline IL blocks with 6 min green exposure patterned at 60 mW (a) and 70 mW (b) in two layers. Though apparently closed, the collapse of the top pattern suggests that this occurred during development.

ability to generate a solid anchor for slab structures is essential and easily patternable by the incorporation of 3DDW into the FLaSk system. Moving beyond supports, the next logical structure to consider is defects (such as would be used as waveguides or cavities), both inside and outside of the FLaSk pattern. The patterning of line defects inside of a FLaSk pattern is relatively trivial other than the already discussed (5.3.1) issues of variable shrinkage. In considering defects outside of the FLaSk patterned region, it is important to consider the effects of the prepatterning on the 3DDW lines in terms of LER. As can be seen in Figure 5-27, 3DDW lines written with preexposure can end up showing some of the 3D motif of the IL. This is highly undesirable as roughness can lead to, for example, lossy waveguides. Addressing this on the top of the sample is trivial and can be done by using a SL to remove the imprint pattern.

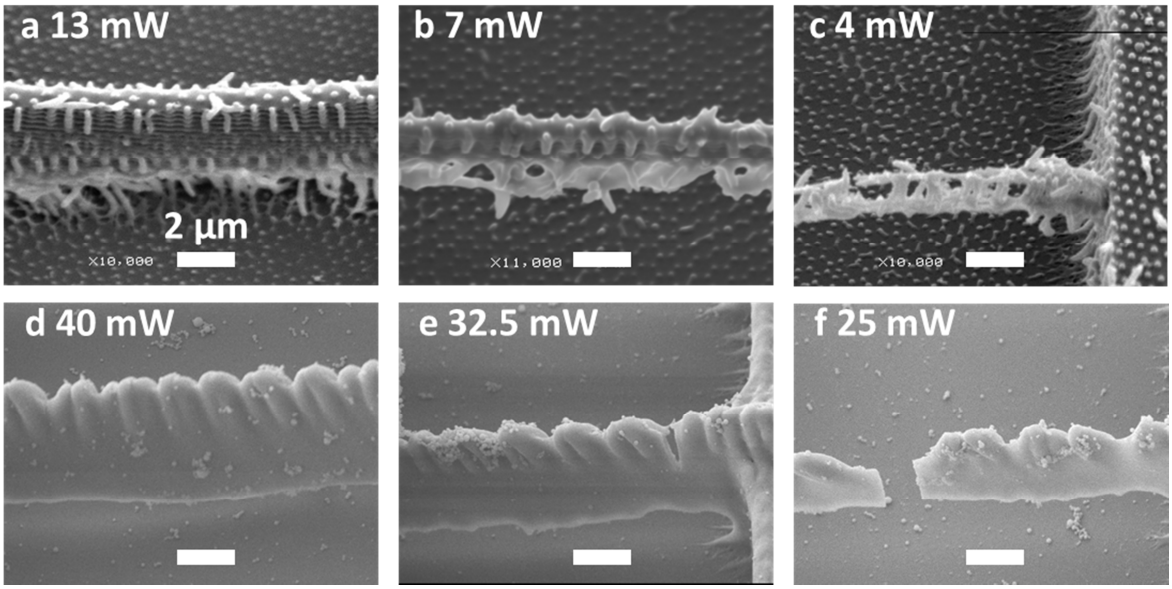

Figure 5-27: Isolated lines written in UV exposed IPL resist (a-c) and green exposed AG 9807 resist (d-f) at 100 µm/s and the powers listed. The IL structuring can be seen in the IPL lines due to the heat generated during UV bleaching, while only the top imprint structure of can be seen in the green lines.

Addressing it in the body and sides line itself requires switching wavelength of the IL exposure as mentioned in 5.3.2. Figure Figure 5-27 shows lines written in the IR 140 resist described above and lines written in green (0.5 wt% ITX, 0.25 wt% HNu 470, 2.5 wt% OPPI, 0.025 wt% AG 9807) resist. The lines written in IR 140 clearly displays the motif of the IL with a solid core of the high intensity 3D writing. In fact, as the writing intensity decreases, the solid portion of the core is much lower than the "roughness" of the motif. In contrast, the 3DDW lines written after green exposure show little to none of the quasicrystalline motif beyond the surface imprint. As discussed, were bleaching the main aspect causing the patterning, the inverse pattern would be expected. To the contrary, the UV patterned sample shows the pattern itself (along with substrate patterning of a hexagonal dot motif), suggesting that the UV bleaching heats the sample while also bleaching it. In the case of the green, while bleaching still occurs, it does so more gradually with a lower overall absorption.

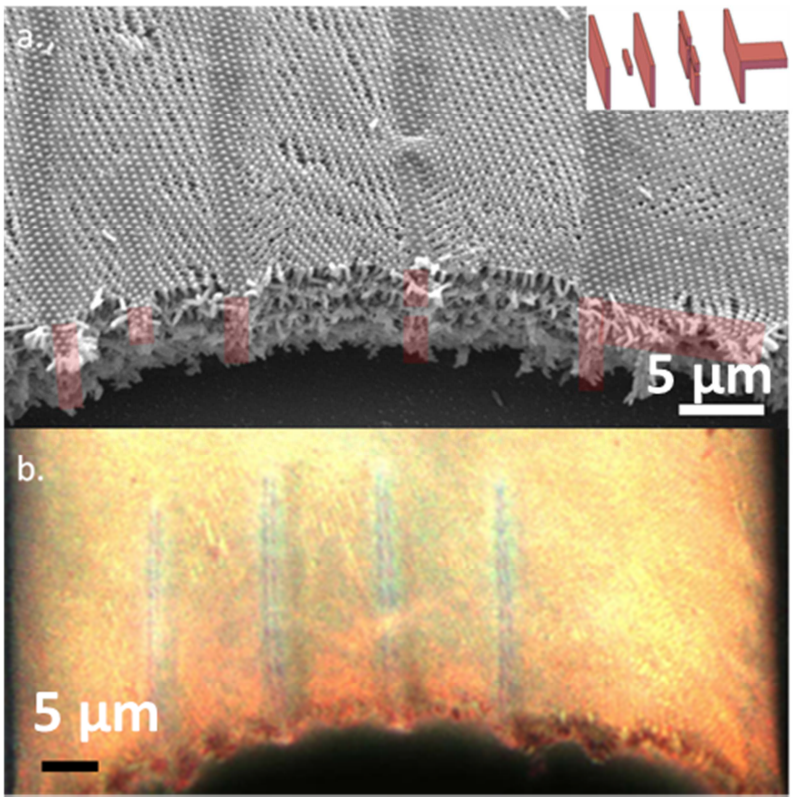

Figure 5-28: (a) 3DDW logo defect patterned in an ~8 µm suspended FLaSk block (3DDW supports out of field of view) drawn in a ~14 µm resist layer. FLaSk structure consists of four repeats of the IL prepattern written at 1 mm/s with a power of 65 mW. Defect is written both horizontally and vertically in the structure (3D schematic shown in inset and vertical features highlighted in red for ease of reader). (b) Contrast corrected polarized microscope image of sample described in (a). 3DDW features that extend through the thickness of the sample fully suppress the scattering from the nanostructured IL block, while features that do not fully extend are barely distinguishable.

5.4.5. **Advanced patterning**

Many of the key features of the combined FLaSk and 3DDW technique are illustrated by the sample in Figure 5-28, where a logo-shaped 3DDW defect has been written in a ~8 µm suspended FLaSk structure patterned in a thicker (~14 µm) IR 140 resist layer. The 3DDW logo-structure is patterned such that the design is both visible from above and from the side, with some components only extending part way through the FLaSk slab, thus creating a truly 3D defect inside a 3D suspended structure in a single

resist process. Shrinkage of the FLaSk structure at or around the 3DDW features can be seen to be suppressed; nevertheless, the overall strain is enough to deform both sets of structures. This sample both demonstrates the potential to achieve it and the challenges that need be overcome in order to do so. FLaSk process allows for tuning of the filling fraction of the structure in 3D, up to, with integrated 3DDW, completely solid, which is not present in any of the previously mentioned combined techniques. 3DDW alone has the capacity to accomplish this patterning in one process; however, it is critical to consider the scalability of such an approach. The FLaSk pattern shown in Figure 5-28 was drawn in a series of 10 μm by 100 μm blocks of 21 FLaSk lines each at a speed of 1 mm/s (faster than is usually employed in piezo-based 3DDW), resulting in a patterning time of ~12 sec per block. For comparison, if we define the structure as four layers of single-shot pillars with single-shot spacers in a 10 μm by 100 μm array, this amounts to 28,900 individual exposures. This would only allow ~0.4 ms per shot, including computation, transit, shutter time and position stabilization (which is already on the order of 4-10 ms on a typical piezo

stage), to keep the same total time. Considering that a typical expo sure time for 3DDW ranges from ms to s, unoptimized FLaSk has already passed the limit of 3DDW patterning rate. This does not consider the fixed time cost of the IL exposure, which is increasingly small with patterning of more features. While the gain in efficiency is only linear with size and depends on the "tall" patterning of IR 140, the proportion of enhancement can be increased by either increasing the write speed or reducing the radial or axial resolution of the FLaSk to fit the application via simple PSF manipulation of the focal spot. On the former point, the current piezo system and software utilized are optimized for nanoscale positioning necessary for 3DDW of a comparable structure, and its speed is thusly limited by the required stage accuracy of these structures. The fact that the nanoscopic features are patterned in a separate step allows for relaxation of the stage stabilization and a utilization of lower accuracy techniques such as the galvano stages discussed above capable of cm/s patterning. For manipulation of the PSF, other than the obvious method of changing wavelength or numerical aperture (Figure 5-25), the most appropriate manipulation technique

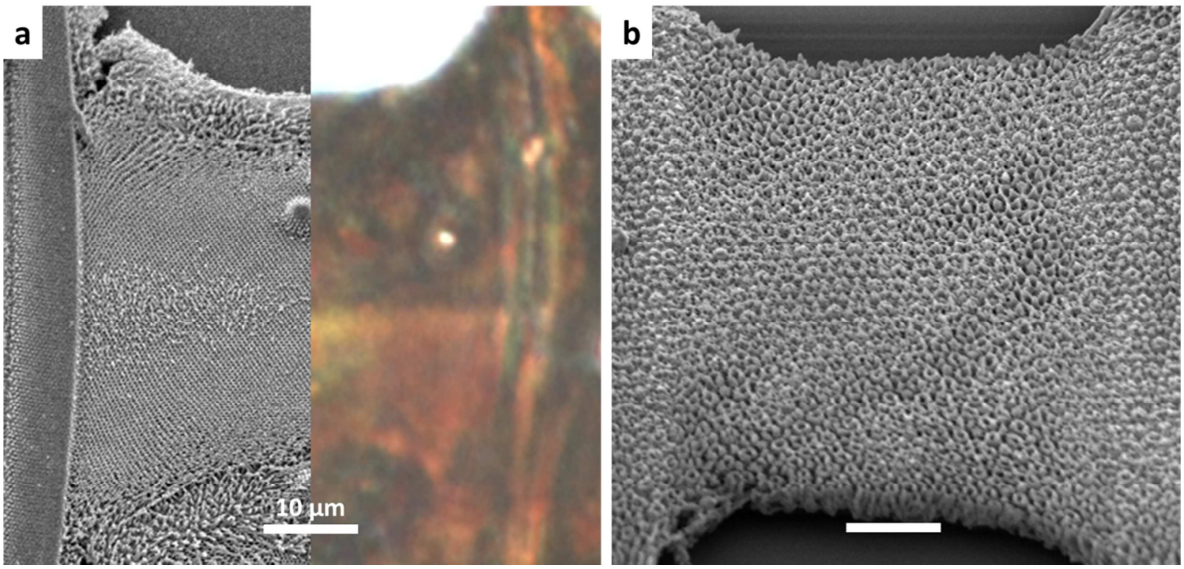

Figure 5-29: Gradient blocks patterned with amplitude modulation. (a) SEM (left) and contrast corrected optical microscope image (right) of tert- butyl CuPd resist gradient block patterned from 42 mW to 82 mW of red exposure and back to 42 mW. Gradient fill may be seen in both images as structure and scattering level. (b) Quasicrystalline gradient block patterned from 38 mW to 70 mW to 38 mW with IR CW light.

is the use of intensity and phase modulation optics before the objective to create non-Gaussian focal distributions. This has been used to increas e focal point resolution or alter the relative axial and radial resolution.[224] In addition, for generation of deactivation beams for STED microscopy, optics for unusual shapes, such as toroid and distributions without central intensity, have been developed.[225, 226] Use of, for example, a torus optic (a commercially available phase plate described in Figure 2-7), could increase the effective lateral spot size by a factor of ~1.5 while not significantly affecting the axial. Finally, it is important to note that the increase in efficiency is dependent also on the IL pattern: the demonstrated phase mask possessed a periodicity of ~1.7λ and a layer-to-layer spacing of ~3λ, by no means the limit of IL resolution. Any reduction of these parameters or the IL wavelength will also lead to gains in efficiency.

The only patterning aspect not demonstrated by this pattern is the ability to write gradient fills, the realization of which is where FLaSk-CAP could truly become a highly competitive fabrication tool for transformation optics and acoustics as discussed in 5.2.5. Figure 5-29a shows a gradient block patterned

in the tert-butyl CuPc resist described above going from a 42 to 82 to 42 mW intensity linearly in 0.5 mW steps. It can be seen in the optical scattering that the fill varies from highly scattering to completely filled. The flaws of the current FLaSk-CAP process can also be seen in the shrinkage, and the issues of tert-butyl CuPc specifically can be seen in the relatively large number of LID events. Also in Figure 5-29b is a gradient quasicrystalline block patterned from 38 to 78 with the tert-buty ZnNPc showing no LID events and a similar variation in density. While the shrinkage issue still needs to be overcome (probably by selection of resist polymer) this sample demonstrates the eventual ability for the inverse solution of transformation optic/acoustic structures possessing continuously varying fills.

5.5. *Conclusions*

Through a combination of PnP IL and FLaSk annealing we have demonstrated an efficient local and rapid modification of a periodic structure. Additionally, a simulation platform for the testing and predictive design of FLaSk fabrication was developed. The strength of the FLaSk technique, especially in combination with MPL 3DDW, arises from its flexibility – though we have demonstrated fabrication using a single PnP phase mask, the family of periodic and quasicrystalline structures possible by either PMIL or MBIL is unlimited and can be tuned for the application. Further, since FLaSk can select the IL region which is fixed, stitched phase masks of multiple designs can be utilized to pattern multiple structure morphologies in a single IL-FLaSk step by avoiding the regions of overlap in the holographic patterns (on the order of the thickness of the resist depending on the wavelength and periodicity used). The eventual result should be device fabrication by nearly arbitrary spatial definition of various periodic elements of controllable filling fraction with 3DDW-defined supports, defects, and interconnects. Beyond CARs, the FLaSk technique is likely applicable to other systems, as thermal annealing is a driving force for many processes (such as those already discussed in Chapters 3 and 4). Future studies in FLaSk patterning of thermal-absorption-doped photoresists will focus on the continued optimization of the materials and process selection to improve the overall quality and capability of the technique and bring together the predictions of coarse-grained simulations and experiments to effectively solve the inverse

patterning problem. As the process develops, there is significant potential for a combined IL-3DDW-FLaSk approach to become a readily scalable technique for patterning of future photonic, phononic, and mechanical devices.

6. Outlook and Future Directions

As stated in the introduction to this thesis, the notion of combinations of local and global lithographic techniques were deemed an area ripe for research. In the above sections, I have introduced several hybrid DW lithographic methods for the rapid production of complex architectures. In accessing predefined large area patterns (be it by deliberate lithography or self-assembly processing), the speed of patterning for a given structure is enhanced at the cost of some portion of control. The degree to which the current embodiments of these techniques is limited by the associated large area method have not yet reached their fundamental limits, if only by the virtue that the parameter space of each is relatively unexplored. The following section will begin by highlighting the accomplishments demonstrated by each technique and then addressing the limitations and potential directions for future investigation.

6.1. *FPnP*

As demonstrated, FPnP is a robust method for creating stand-up structures, such as those that were applied to SRRs. The structures can be tuned by both optical and resist parameters. There are several key drawbacks to the method. One such example is that it is difficult to make the W-resonator on a transparent substrate. The W-resonator needs to be attached to a conductive base to complete the structure, and therefore cannot be patterned without either a conductive substrate or integrated consecutive DW (Figure 6-1). The base could be provided by transparent conductor, such as ITO; however, the low conduction of transparent conductions would diminish the efficiency. A more fundamental drawback is the resolution of the demonstrated FPnP, a combination of the numerical apertures used, the resolvancy of the grating, and the wavelength. While there are ways of addressing these issues, the necessity for non-linear excitation to achieve contrast enhancement may make it difficult to push the resonance of FPnP optical structures towards near-IR or

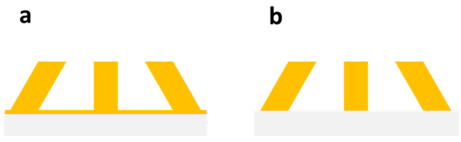

Figure 6-1: Sketch of FPnP pattern on (a) a gold coated and (b) a transparent substrate. On the transparent surface, the loop of the resonator is broken.

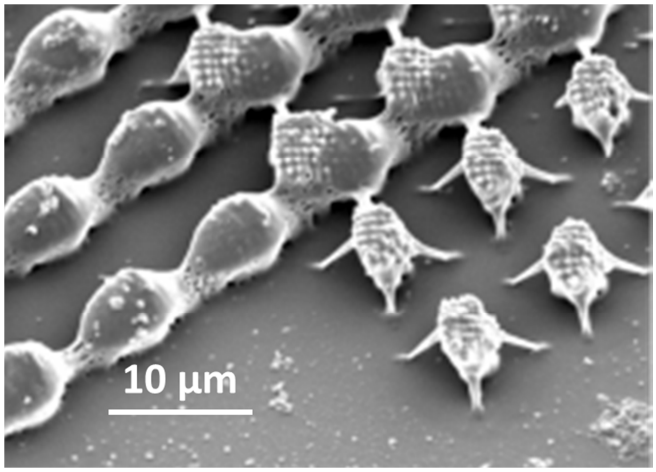

Figure 6-2: Multiple imprint (p2mm then p4mm) FPnP attempt showing overbaking (p2mm) and film crushing (p4mm).

visible response. The correct strategy, therefore, may be to identify different application areas where the speed of the technique is advantageous over its limitations in both the size and variety of structures that can be fabricated. It is possible that the channels shown in Figure 2-7c may in fact be a more interesting method because FPnP is an exceedingly fast method to pattern micron scale channels with only *xy* control. These could be applied to, for example, microfluidics, though an inability to turn the channel may make application difficult. In order to improve the capabilities of the technique, two possible methods to increase the flexibility would be the demonstration of multiple cycles of mask imprint, exposure, and mask clearing or the extension into lower wavelength patterning.

6.1.1. **Multiple imprint patterning**

Three methods of patterning multiple structures have so far been introduced that are applicable to FPnP: (1) multiple patterning by changing optical parameters (2.3.2, Figure 2-5), (2) multiple patterning by clearing the mask and utilizing 3DDW (2.3.5), and (3) multiple patterning by adjacent masks (5.2.4). With FPnP, however, there is the added potential of utilizing multiple masks in the same region by clearing the initial mask and reimprinting with a different mask. This has been attempted several times with very limited success (Figure 6-2). The main difficulties are the necessity of heating, which progresses the crosslinking of the first patterned CAR layer, and pressure, which can actually be observed to deform the first patterned structure (neither a surprise). Both issues should be addressable by the use of an orthogonal SL as described in 2.3.4. The latter could be addressed by using a low melting point SL that could even be orthogonally removed and reapplied with a very volatile solvent (such as the cyclohexane

already being employed). The former problem would further necessitate that the SL be selected such that its softening temperature be lower than the activation threshold for the CAR. For example, SU-8 can only be exposed to temperatures around 40 ºC for ~1 min before undergoing crosslinking, but other resists, such as positive tone ones,[205] can have activation energies that require bakes at ~130 ºC (see 7.2), and therefore could be resistant to multiple mask applications and removals. Incidentally, such resists, being generally utilized for DUV, could also potentially allow for non-linear patterning with deep blue or UV sources, simultaneously increasing the overall patterning capability. Increasing resolution will, however, come at the cost of increasing the difficulty of accomplishing registered pattering (discussed in 2.3.3), as optical validation will become increasingly difficult. Methods such as alignment by Moiré fringe diffraction (as has been used for nanoimprint alignment)[227] could be approached, and would also be useful for other registered defect and combined patterning methods, such as FLaSk-CAP.

6.2. *FLaSk dewetting*

Dewetting of polymer thin films as a positive tone process through FLaSk heating of the substrate is a relatively new technique and has only really begun to show its potential for development-free positive tone patterning of 1D or (barring overlap) 2D structures. As currently presented, it exists in two distinct forms: (1) patterning of isolated trench-ridge lines near the optical limit and (2) patterning of subwavelength lines by overlapping the exposures. Before entering a discussion of improving this technique for patterning, it is important to note that, even more so than the other discussed methods, there is a large opportunity for studying the fundamental materials physics that is occurring, especially with regards to the seeminly linear behavior adopted in regime (2), where there appears to be a large interplay between the wetting properties of the polymer melt and the patterning parameters.

Considering patterning, while capability (2) is more exotic, capability (1) should not be diminished; submicron 2D DW in a method that requires no developer step and only uses inexpensive, commodity polymers, free space optics, and visible (sub-Watt) lasers and could be a potentially competitive process,

especially for industrial scale fabrication tools where price is a critical concern. Ironically, the presence of the overlap effects that allow for (2) is the major limitation of this technique: patterning any feature wider than a single line or crossing another feature will be complicated by the overlap effects. This could potentially be addressed by changing the focus, which proved to be an effective way to alter spotsize in Chapter 4 and programming intricate focus, spot-shape, power, position paths to make desired features, not unlike how 3D laser printers currently operate. This is a problem of optimization and software that could be approached in the future; however, one way to at least limit these effects is to increase the resolution of patterning. This could be accomplished via the usual methods of increasing the NA or decreasing the wavelength, but, the efficacy of such a strategy would be limited by the coupled thermal effects. Moreover, any increase in NA lowers the scalability by lowering the working distance and field of view. Instead, it would be desirable to increase the resolution by limiting the thermal spread, which is possible, as seen in Chapter 4 by the incorporation of a volatile solvent to carry away heat. Another possible manipulation is the thermal or etching properties of the utilized polymer. Finally, it would be desirable to be able to use this positive tone process for liftoff rather than just etching.

6.2.1. **Incorporation of solvent**

The effects of including solvent within the polymer film in Chapter 4 were shown to limit the extent of thermal excitation, thereby increasing thermal gradients for enhanced patterning. The same logic should also apply to the application of FLaSk to dewetting. In fact, the dewetting lines that did appear in the solvent exposed PS-PDMS BCP possessed resolutions often much greater (~200-600 nm) than those observed in the single PS-only lines after PS removal and conversion to SiO_x (Figure 6-3a). Were these samples not further structured by the BCP microdomains (which is why we are generally interested in them), they would make excellent etch masks for the dewetted line. It is important to note that PS-PDMS on untreated substrates often showed a tendency to undergo Rayleigh-like instabilities in dewetting (Figure 6-3b), so it would have to be tested if the PS-brush layer may also have some contribution to

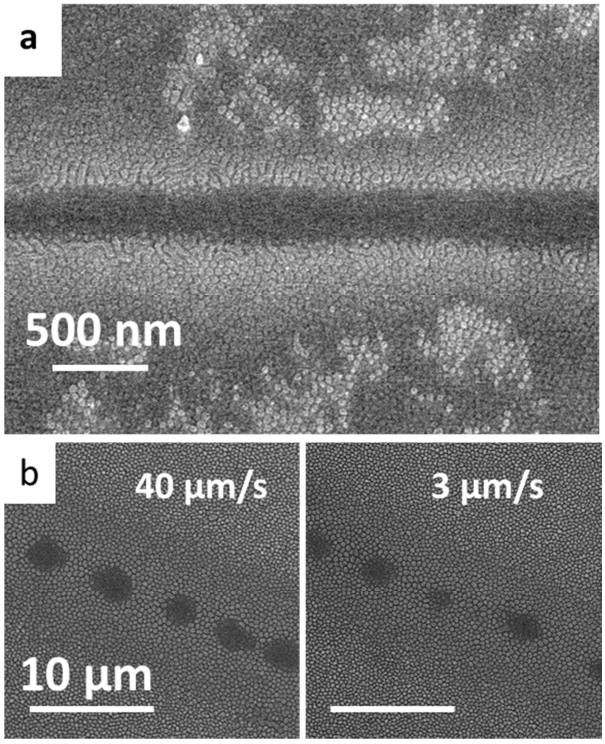

Figure 6-3: (a) Dewetting line in solvent swollen PS-PDMS BCP after plasma etching. Line resolution appears to be enhanced (~250 nm) compared to unsolvated PS patterns. (b) Rayleigh-like instability in PS-PDMS dewetting on untreated GaAs surface for two write speeds. Dewetted dot periodicity appears independent of write speed.

changing the dewetting properties, which would make reasonable sense as the mobility on an unfavorable substrate may be higher since there is already a drive to dewet.

6.2.2. **Polymer selection**

The selection of polymer could have a potentially large effect on the final pattern generated by FLaSk dewetting. By increasing glass transition, for example, sensitivity to fluctuation and resolution should be diminished as a smaller portion of the exposed area would be mobile. Figure 6-4a shows a high resolution grating patterned in polyvinyl pyrrolidone (PVP), another commodity polymer possessing a higher T_g (~180 ºC) that is also water soluble. It can be seen that the pattern quality is much improved. Performance of both capabilities (1) and (2) with a target application of pattern transfer are also limited by the selectivity of PS (or PVP) to etch (setting a bound on the maximum aspect ratio). While PS or PVP are commodity polymers, it may be feasible to utilize slightly more designer systems while still not reaching the complexity and expense of a photoresist, which incorporate photoinitiators and demand UV isolation and/or cooled storage. For example, silicon containing polymers (and even small molecules) convert to SiO_x hard masks upon ion exposure, making them good candidates for dewetting resists.

6.2.3. **Bilayer resists**

Currently, the sidewall profile of FLaSk dewetting lines is wider at the top than the bottom (shown schematically in Figure 6-4b) and relatively sharp for both the isolated features and the overlapped features, a beneficial trait for etching; however, many patterning processes involve the deposition of metals by using a bilayer resist process wherein the top layer has a lower etch sensitivity than the bottom resulting in an overhanging profile (shown schematically in Figure 6-4b)[228, 229] beneficial for liftoff. Imagining a method to create such a profile based on a thermal mechachism is not as straightforward – even by utilizing materials with differing thermal properties (such as T_g), they will likely be mixed or undergo macrophase seperation during dewetting in the melt state. One possibility is to use a high (>200 ºC) T_g polymer as an underlayer. In this way, when the polymer dewets, it can act as a mask for a wet etch undercut in an orthogonal solvent. An example pair of polymers would be a low MW polystyrene (T_g=50~60 ºC) spun out of cyclohexane on a layer of polymethacrylicacid (PMAA, T_g=~150 ºC), which is base soluable. To add additional control, the bottom layer could even consist of a protected PMAA based CAR.

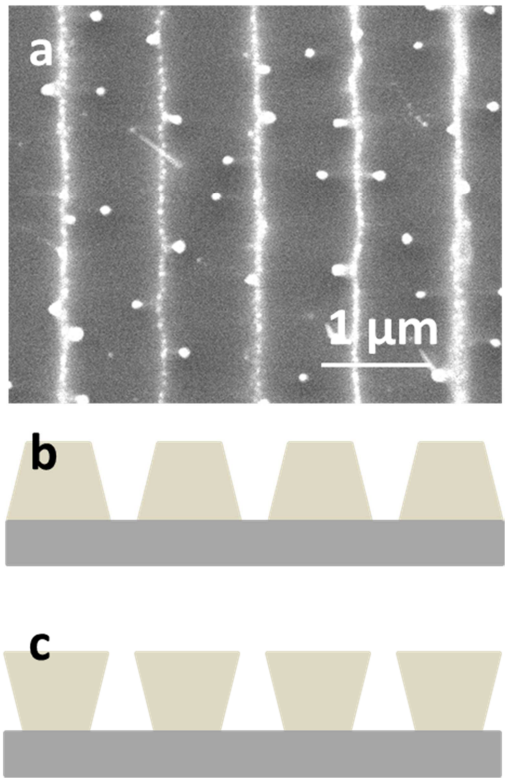

Figure 6-4: Transferred grating patterned at a 800 nm periodicity at 260 mW, 100 µm/s in 64 nm of PVP. (b) Schematic of the morphology of lines obtained by dewetting, generally incompatible with liftoff which requires overhanging features as shown in (c).

6.3. *FLaSk zone anneal of BCP*

FLaSk zone annealing of BCP has recently become a proven process for orienting and aligning BCP. What has been established so far is that for a BCP system strongly segregated enough to undergo a FLaSk

spike without crossing its ODT, the moving gradient of the 2D substrate hotspot can serve to both zone anneal the BCP from a metastable phase to the equilibrium microdomain shap separation and also align the microdomains (predominantly) along the write direction (or more generally along any large thermal gradient) even for highly *curved* paths. The size of the annealed line can be controlled by focusing within the sample. Limitations of this technique appear to be the effects of the boundary gradients, which cause outward canting of the edges of the patterned lines and the fact that once the polymer has formed the equilibrium morphology, subsequent passes do not appear to increase the order (though order may be increased beyond the single line limit by reaching the cylindrical morphology through multiple, lower temperature passes. It should be noted that for patterns where multiple passes were attempted, the power was not changed in between passes. Considering the ARC properties of the BCP, the temperature of subsequent passes is reduced. The current setup does not allow this to be simply done, so incorporation of an AOM (or similar) to the high power source could vastly increase the capabilities for patterning. To push forward FLaSk zone annealing as a common patterning process, optimization of the various process parameters are necessary. It should be pointed out that, even barring application of this technique to patterning, there is considerable novelty in the concept of incorporating solvent vapor in a DW process alone. This is analogous to the use of sprayed fluid coolant in conventional machining, but in a process that possesses nanoscale resolution.

6.3.1. **Parameter tuning**

Polymer materials

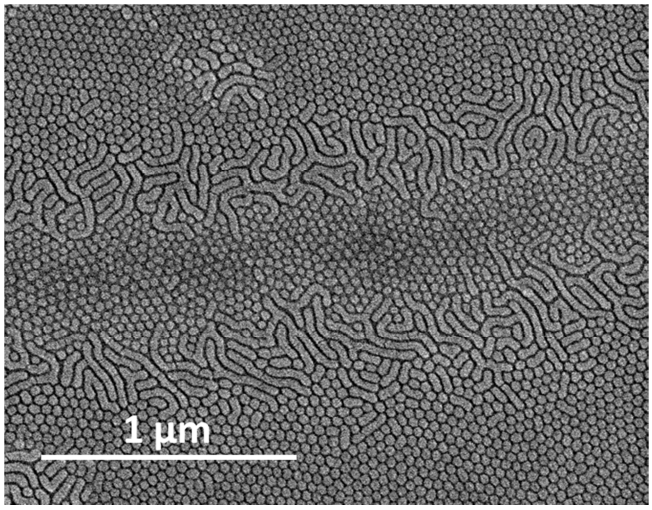

Figure 6-5: Portion of a circular line written with increased solvent at 640 mW, 100 µm/s focused 6.5 µm below the substrate. Spheres are observed at the center of the line with a lower power than used for other lines where spheres were observed (generally the high power limit of patterning) and cylinders are not observed.

PS-PDMS has the benefits of being able to be placed into a metastable state in spin coating and the ease of removing the PS for observation; however, its strong segregation makes diffusion past the intermaterial dividing surface difficult. Weaker segregating BCP have been utilized for cold zone studies in the past, such as similar molecular weight PS-PMMA.[130, 133, 175] The weaker segregated system still possesses the ability to be reordered by the directional thermal anneal. Another method to increase the mobility is to employ lower molecular weight or terblock polymers, which in turn have lower energetic barriers to reorganization. Finally, a crosslinkable[173] or controllably removabele BCP could be employed to lock the highly aligned center of the FLaSk line.

Solvent tuning

The important role of solvent in FLaSk zone annealing is more likely be to cool the system than for the mobility that is added. A natural next step for improving this effect is to increase the amount of solvent added to the system. This was shown, at least in preliminary studies, to result in a decrease in the observed order and result in a central pattern of the original spherical micelles or vertically aligned cylinders (Figure 6-5). These results merit further investigation; though two possible mechanisms are expansion driven alignment as predicted for certain zone anneal configurations[176] or directional evaporation induced vertical cylindrical alignment.[136] Another strategy is to approach solvents with different thermal properties. For example, solvents with higher boiling point (such as PGMEA) might be

expected to continue to cool the surrounding polymer to even higher temperatures and for a longer fraction of the annealing process. On the other hand, solvent vapor pressures above a sample in general are highly sensitive systems to air flow, temperature, etc. and require a high level of environmental control to produce reproducible results. Also, the interaction with the polymer may change from solvent to solvent. To move beyond solvents, solid-state evaporative (a.k.a. "sublimative") cooling may be approached, such as by using thin films of amorphous small molecule compounds with low sublimation temperatures such as benzoic acid.[135] In this way, the cooling can be controlled by the top film thickness, with the downside of adjacent and multipass lines being difficult to process as, unlike the solvent, the small molecule will not reabsorb into the polymer layer as it would be difficult to provide a replenishing vapor without continuous deposition. For isolated, single pass; however, this should make the most controllable and repeatable set of cooling parameters.

Laser parameters

The system utilized for FLaSk zone annealing of BCP, while collimated and spatially filtered, was not the most stable arrangement utilized in these studies as the Verdi laser utilized was being operated well below its full, most stable power. Beyond this and the already mentioned lack of an AOM or other computer controlled power modulation on the Verdi laser path, which could greatly improve the number of experiments possible and the rate of their execution, there are other routes to improving the optical parameters for FLaSk zone annealing. The most obvious example, as briefly discussed, is by changing the PSF of the laser excitation in such a way to create an asymmetric thermal gradient that eliminates the outward canting and improve the ordering along the write direction. It should be noted that to maintain path independent tracking, the spot manipulation would have to be implemented such that the short axis of the anisotropic spot was aligned parallel to the write direction, thus ensuring the same annealing behavior in all directions of writing.

6.4. *FLaSk-CAP*

As demonstrated, FLaSk of IL exposed CARs has shown the ability to pattern gradient-fill structures with controllable defects by consecutive integrated 3DDW. Through dye optimization, the smoothness of the 3DDW was also improved. In addition, a framework for coarse and fine-grain simulations has been established that could potentially lead to inverse design of large scale GRIN structures for optical applications. There remain considerable addition issues, particularly with thermal expansion and, more critically, sample shrinkage. Regardless, achieving the quality necessary for the target application of microphotonics will be challenging. For example, registration with the IL structures may be difficult, even though assisted by markers such as the surface nanoimprint fringes. Thus it is desirable to find other potential application areas. For example, structures with hierarchically controlled nanopillars[230] or 3D porosity have been shown to initiate drop dewetting and coalescence.[231] By utilizing FLaSk-CAP, the porosity (or for 2D high aspect ratio IL) could be patterned with a continuous gradient in surface energy leading to highly controlled 2D surface energy maps and droplet paths.

6.4.1. **Thermal expansion and shrinkage reduction**

Thermal expansion reduction could be approached, as mentioned by incorporating a preexposure bake, with bakes of SU-8 up to 313 K for 1 minute not leading to crosslinking on development. Shrinkage, on the other hand, is a much larger issue and most likely will necessitate resist system development, particularly with regards to positive tone resists, such as the previously developed mass persistent systems. Critical point CO_2 drying could also be approached as an alternative to solvent evaporation, where liquid CO_2 infiltrates the structure and is then removed by lowering the pressure at increased temperature.[232] This leads to capillary force-free drying.

6.4.2. **Parameter extraction**

The chemical models for FLaSk-CAP have all relied on tabulated chemical parameters which can be sparse in terms of their availability and may or may not apply to the rather extreme kinetic descriptions described by FLaSk. It would be much more useful to extract the parameters directly from the FLaSk-

CAP DW in some way. To approach this, the following derivation was done starting with the generalized chemical parameters and making various assumptions. The overall strategy was to simplify the expressions as much as possible and group coupled parameters into empirical constants. The starting point was to take the generalized deprotection equations discussed in 5.2.1, assume they are of first order and then substitute and simplify:

$$\dot{M} = -kM^p H^q \qquad \textbf{Eq. 6-1}$$

$$\dot{M} = -kMH_0(1 - e^{-CE}) \qquad \textbf{Eq. 6-2}$$

$$\dot{M} = -Ae^{-R/T(t)}H_0(1 - e^{-CE})M \qquad \textbf{Eq. 6-3}$$

$$\frac{dM}{M} = -AH_0(1 - e^{-CE})e^{-R/T(t)}dt \qquad \textbf{Eq. 6-4}$$

This last equation leaves four parameters, the initial acid concentration H_0, the kinetic prefactor A, the kinetic rate constant R and one grouped exposure sensitivity constant C, whose effect depends only on exposure dose. In such an extraction, flood exposure could be used to make C spatially constant. The next step was to attempt to integrate this function to solve for the deprotected fraction M/M_0. What makes this more complicated than the usual case is that the temperature is a function of time, so Eq. 6-4 will have to be solved as the definite numerical integral for each specific case. The next assumption introduced was that, while the peak temperature varies with time, the spatial temperature distribution remains constant and just goes through a temporal Gaussian weighting, which is supported by simulation (Figure 5-12). This form of this distribution consists of a profile increase per optical flux $G(r,z)$ (determined from fine grain simulation), the exposure intensity I, the temporal width w, and optical losses to the sample φ. Also included is the cutoff c, which is defined as the deprotection fraction where the sample becomes insoluable in the developer:

$$\ln\left(\frac{M_f}{M_0}\right) = -AH_0(1 - e^{-CE})\int_0^{t_f} e^{-R/(T_0 + \varphi IG(r,z)e^{-\frac{t^2}{w}})}\,\mathrm{dt} \qquad \textbf{Eq. 6-5}$$

$$\ln c = \ln\left(\frac{M_f}{M_0}\right) = -AH_0(1 - e^{-CE})\int_0^{t_f} e^{-R/(T_0 + \varphi IG(r,z)e^{-\frac{t^2}{w}})}\,\mathrm{dt} \qquad \textbf{Eq. 6-6}$$

$$-\frac{\ln c}{AH_0} = (1 - e^{-CE})\int_0^{t_f} e^{-R/(T_0 + \varphi IG(r,z)e^{-\frac{t^2}{w}})}\,\mathrm{dt} \qquad \textbf{Eq. 6-7}$$

$$\mathrm{N} = (1 - e^{-CE}) \int_0^{t_f} e^{-R/(T_0 + \varphi I \cdot G(r_c, z_c) e^{-\frac{t^2}{w}})} \, \mathrm{dt} \qquad \textbf{Eq. 6-8}$$

In the last expression, $G(r_c,z_c)$ is the point in the z_c slice where the calculated deprotection distribution is widest radially (r_c, z_c). In this form, the top-down line width from experimental data can be utilized along with the flood and FLaSk exposure doses and write speed (here represented by w) to fit for individual and grouped parameters: C (dependent on E), R, φ (dependent on I), N (containing information on the cutoff, rate coefficient, and acid concentration). As two of four of these parameters depend on independent variables, their effect can be easily isolated, leaving only two invariant empirical constants. Of these, N represents the greatest loss of general information as it groups three separate resist parameters; however, the fact that they are grouped means that it should be possible to group them in the actual fine-grain chemical simulations by reframing the equations. Thus, if the assumptions made were valid, it should be feasible to extract the relevant materials properties for FLaSk inverse solution via analysis of large batches of data from flood exposures, such as shown in Figure 5-22.

6.5. *Summary of accomplishments*

The various directions for future investigation underscore the significance of the capabilities demonstrated in this research. Chapter 2 introduced focused proximity field nanopatterning (FPnP), a novel combination of laser direct write (DW) and imprint lithography that allowed for the predefinition of stand-up resonators in a ~1 min imprint process that could then be communicated into the resist in sub-second single shot exposures. To develop this process, it was further necessary to introduce the use of an orthogonal sacrificial layer for multiple patterning and cross-section control as an ancillary technique that has many potential applications. Chapters 3-5 introduced the concept of focused laser spike (FLaSk) annealing, the use of highly focused light to introduce rapid spikes in temperature additionally possessing exceedingly sharp spatial and temporal thermal gradients for DW patterning. Specifically, in Chapter 3, FLaSk was used to perform thermocapillary-driven dewetting of sub-diffraction limit lines (0.6-1 μm widths) in a polymer thin film that could be transferred to the underlying substrate without the need for a development step. Here the effective pattern multiplication or formation of a hierarchical structure

manifested in the behavior of these lines as they approached one another – entering a self-assembly regime of sub-100 nm feature gratings that was apparently a property of the film rather than the patterning parameters. In this way, rather than achieving pattern multiplication of the written lines, the revealed latent motif acted as a sort of exchange rate – converting many, low resolution DW steps into fewer, high resolution features. Chapter 4 considered the dewetting phenomenon at the pre-dewetting boundary, where the massive thermocapillary stresses that lead to dewetting are present within the film, yet insufficient to initiate complete dewetting. By replacing the unstructured homopolymer film with a highly segregating block copolymer (here PS-PDMS) trapped in a metastable state, this stress field can be utilized to initiate ordering and alignment along the write direction (indicating the importance of the temporal thermal gradient). The efficacy and thereby processing window of alignment was further expanded by the novel incorporation of solvent vapor above the patterned sample. While this complicated the understanding of the annealing process, it allowed for a demonstrated order up to 33° FWHM of the Fourier transform through a combination of mobility, evaporative cooling, and surface energy ("solvocapillary") mechanisms. The limits of this alignment have certainly not yet been reached, with write speeds up to 1 cm/s and curvatures up to 0.20 cm^{-1} displaying write tracking. While the timescales of this technique leave some defects, it is currently the most rapid technique (anneal times are on the tens of millisecond scale) for initiating designer in-plane anisotropy and phase-connectivity on the sub-microscale (300-3000 nm line widths), tunable by the focus of the laser. Finally, Chapter 5 realized FLaSk as a full 3D patterning technique, by utilizing dye-doped chemically amplified photoresist films containing latent 3D structures defined by phase mask interference lithography. Using this technique, both the positioning and fill of these 3D structures could be controlled by millisecond scale DW bake to define either continuous or gradient index structures, either connected or disconnected from the substrate, with submotifs of highly-ordered periodic or quasiperiodic submicron lattices. These could potentially find applications in 3D phoXonics or other applications where there is a value to controllable porosity, such as wetting and catalysis. In addition, it was shown that the results of this patterning method could be

approached by highly parallelizable inverse solutions by using coarse-grain simulations informed by fine-grain finite element method simulations.

While the patterning quality of these techniques continues to improved, they each represent a shift in the burden of high resolution patterning from the DW to the large area technique. For example, the methods of Chapters 3 and 4 utilize objectives with NA=0.4 to define sub-100 nm features, while the methods of Chapters 2 and 5 use 780 nm light to define structures with 100 nm components. Furthermore, lasers utilized for FLaSk techniques (Chapters 3-5) were continuous wave as opposed to expensive femtosecond pulsed lasers, and Chapter 3 even utilized commodity polymers (PS), which cost a fraction of the price of either the designer resists of Chapters 2 and 5 or the expertly synthesized block copolymer of Chapter 3. All said, these developments relax requirements on laser parameters such as stage precision, spot size, and stability as well as materials for a net result of highly scalable techniques that could potentially compete with commercial systems. Beyond this, due to integration onto a DW stage, high resolution DW patterning can be integrated into any of these techniques to further enhance both the capabilities of the hybrid technique and the scalability of the DW. Most importantly, all of these techniques have just begun to explore their individual parameter spaces, leaving open the possibility for even greater demonstrations of more rapid, higher quality patterning of functional or precursor materials for metamaterials devices possessing a combination of unique structural and materials behaviors.

7. Appendixes

7.1. *Testing decomposition during FLaSk*

Considering the high temperature of the 2D FLaSk process, it is natural to be concerned that decomposition may occur in the polymer. This is further enforced by the observed decomposition of PDMS at the highest exposure doses (Figure 4-5). For PS, there is previously established models for the decomposition paths. One of the more accurate models approximates the decomposition as a two-step process of transformation into oligomers and then evaporation.[233] The kinetic model established in this work was:

$$\frac{dPS}{dt} = -k_1 e^{\frac{-E_1}{RT}} PS^{n_1} - k_2 e^{\frac{-E_2}{RT}} PS^{n_2} \qquad \textbf{Eq. 7-1}$$

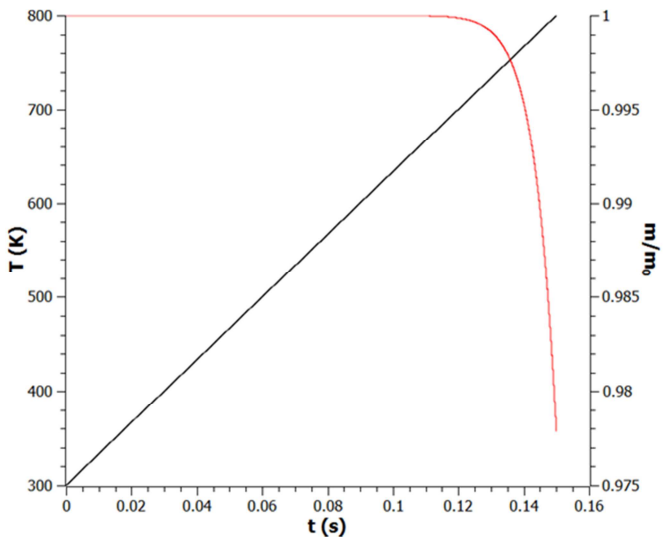

Figure 7-1: Simulation of 0.15 s, 800 K bake (black) of polystyrene. Despite the high temperature, <2% of the normalized PS mass (red) is expected to decompose.

Where the kinetic parameters utilized are listed in Table 7-1. To test the decomposition during FLaSk, the mass loss of PS monomer was simulated for a high temperature (800 K) and slower (150 ms) anneal (Figure 7-1). This simulation revealed that even after this anneal only 2% of the PS would be expected to be removed.

Table 7-1: Decomposition parameters for PS

Parameter	Value
n_1	0.51
k_1	6.85e14 s^{-1}
E_1	220.3 $kJ \cdot mol^{-1}$
n_2	1.02
k_2	6.12e17 s^{-1}
E_2	276.6 $kJ \cdot mol^{-1}$

7.2. *Use of positive tone resist for high resolution 3DDW*

As discussed in 5.3, the use of a positive tone CAR resist for 3D fabrication is highly attractive due to the beneficial shrinkage and inversion properties. To date the only reported 3D fabrication in literature is micron resolution 3DDW[204, 205] and more recently (in a dissertation) IL down to a period of 760 nm.[234] These studies all utilized tetrahydropyranylmethacrylate (THPMA) based positive toned resist. This was selected due to its low activation energy allowing for low temperature PEB and avoiding the foaming of volatiles that is deleterious for 3D fabrication. This comes with a drawback of room temperature reaction progression. Ideally, a more ubiquitous, higher energy system would be usable. To investigate this, the

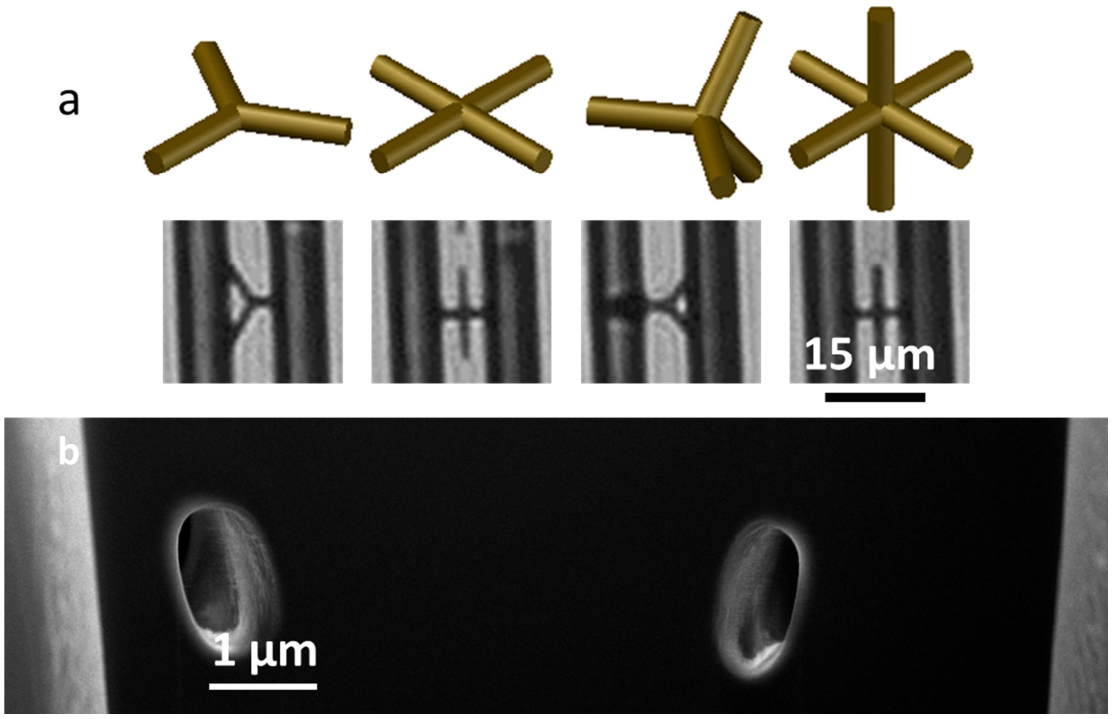

Figure 7-2: ESCAP resist structures. (a) Optical microscope images of several 3D structures made dot wise in ESCAP resist with longer bake. (b) High resolution FIB cross-section of a three branch structure revealing sub-micron structuring.

highly utilized ESCAP[235] photoresist, which is a random copolymer of hydroxystyrene and tertbutylacrylate, was synthesized. This resist generally requires an unusually high (~130 ºC) PEB. It was found that by utilizing lower bakes still higher than the THPMA or SU-8 systems (~120 ºC) for longer times (3 min) could also accomplish the deprotection and led to much higher resolution structures (down to ~700 nm), shown in Figure 7-2.

7.3. *Shock wave mitigation by open phononic systems*

The desire to mitigate and manipulate shock waves incident on a structure is natural from the standpoint of protective materials, both at the macroscale for applications such as soldier protection and also at the microscale for device shielding. It is unsurprising for this reason that there has been a significant amount of research over the past few decades on the propagation of shock in composite protective media. For the most part, these have been focused on layers[236, 237] (or chains[238]) of materials on the mm scale impacted by either rapidly moving projectiles[237, 238] or blast waves.[236] While these studies have revealed a significant importance of interfaces and resonance behaviors in increasing shock wave mitigation, they have not provided an optimized design for a periodic shock wave mitigator. What we have attempted to do is approach this problem from the standpoint of phononics. Phononic crystals (the acoustic analog to photonic crystals) are metamaterials possessing periodic (or quasiperiodic) variations in acoustic impedance leading to unusual acoustic dispersion and the opening of forbidden propagation bands. Phononics have become an increasingly active area of research[239-242] due to the potential applications such as acoustic cloaking or even thermal isolation.

When a linear pulse interacts with an ideal phononic crystal, the various frequency components that it is made up of each are forced to travel through the metamaterials, at the group velocity particular to its k. Non-propagating components (frequencies in the bandgap) are therefore completely reflected. As a result, the pulse upon exiting is neither a pulse spatially, as various frequency components have been removed, (reflection) nor temporally, as portions of the energy (moving slower through the crystal) have been lagged behind the main front (dispersion), but rather will possess multiple high intensity peaks and long ringing tails. As a peak width of a pulse in real and frequency space are inversely related, the efficacy of a phononic crystal in interacting with an incident pulse is highly dependent on the width of that pulse. In essence, broad pulses will possess most of their energy near ω=0 and therefore will require very large period structures to have any effect while narrow pulses, with a broad frequency spectrum, will need a periodicity targeted such that the particular distribution of bands covers a maximal quantity of the energy

as higher order peaks usually display similar *absolute* peak widths and thus rapidly diminish in effect. As a result, if the goal was to best mitigate an incident linear pulse, undoubtedly, the correct solution would be a stack of multiple periodicities or a quasicrystalline system such as the broad spectrumed Fibonacci structures.[221] These however, have not been actively approached as shock mitigation strategies. One possible reason is that shock waves are *not* linear pulses and therefore could potentially behave completely differently when interacting with phononic crystals, though from the prior results, it would seem that the resonant behavior of periodic systems does have some effect. This leaves the open question as to whether the best phononic structure for dissipating a linear pulse would be nearly as effective at dissipating a shock. The other reason it may be difficult to approach the systematic evaluation of phononic structures for shock is the way in which shocks are induced and measured. For example, the impactor method due to its dynamic complexity, does not produce a non-linear pulse analog in terms of sharpness of the induced wave. Waves induced by triggering exterior explosions outside of multilayered composites also possess the difficulty of front-face reflection of the wave and thus diminished signal. It is for this reason that we approached shock of open 2D structures as a method to utilize low-reflection unit layers to systematically study.

7.3.1. **Simulations of linear pulse interaction**

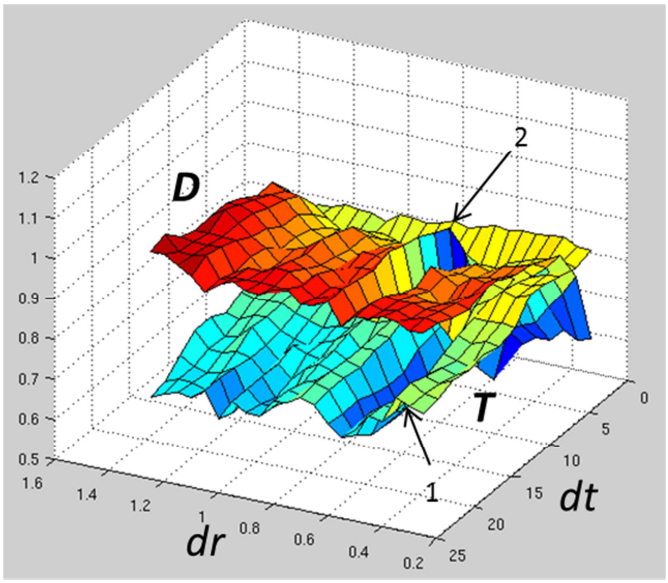

Figure 7-3: Plots of transmission (*T*, bottom) and dispersion (*D*, top) for a four layer phononic barrier for different linear pulse (*dt*, related to pulse width) and structural (*dr*, related to layer-to-layer spacing). It can be seen that there is a trough of minimal transmission (1) and dispersion (2), that are close but not coincident.

To generate a frame of comparison for the shock mitigation, FEM modeling of the interactions of a linear pulse with a model phononic system of blocks was performed. The unit cell (lattice parameter, a) of this structure was a line of infinitely tall close-packed, square cross-sectioned $a/3$ by $a/3$ blocks with each third block removed to generate a permeable wall. These blocks were treated as perfectly hard with impedance $Z=\infty$, which is a reasonable assumption for solid-liquid interactions where the impedance mismatch is high and therefore most of the amplitude will travel in the liquid phase. To capture the possible behaviors, a system of four repeats was setup and two unitless parameters (dr and dt) were varied: the spacing between layers ($b=a\cdot dr$) and the temporal width of the peak ($\sigma=a/(c_L\cdot dt)$, where c_L is the speed of sound in the medium). For each value of the parameters considered, both the total amplitude transmission

and the broadening (the standard deviation in time over which the amplitude is experienced normalized by the original width) are plotted in Figure 7-3. In the transmission plot there is a definite region of highest efficiency represented by a trough that occurs at dr=0.55 and dt>5. This maximal reflection coincides with a minimal dispersion trough, though dispersion also trends upward with shorter pulses. It can be seen, however, that there is a region of high dispersion near as the layer spacing increases with the expected highest dispersion/reflectivity pairing occurring around dr=0.55 and dt=17. While systematic study of shock on these open structures remains for future work, some preliminary experiments using 3DDW structures with incident single laser pulse induced shocks within a fluid medium have been conducted Figure 7-4. The results have shown that it is possible to obtain high reflection and dispersion from these mostly open structures.

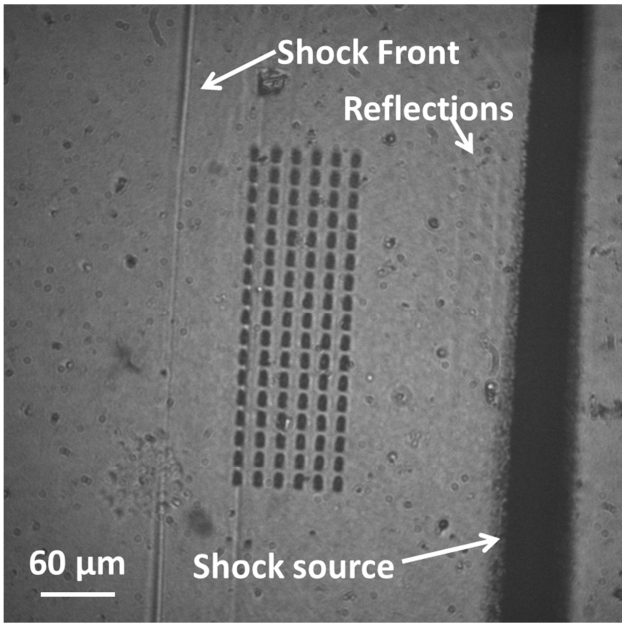

Figure 7-4: Optical snapshot of laser shock experiment on a six layer 3DDW open phononic structure with the shock source and front along with the reflections labeled. The shock front contrast comes from a densification of the fluid due to the nonlinear wave. It can be seen that the portion of the shock that passes through the structure is greatly dispersed leaving almost none of the original densification (*i.e.* a linear pulse).

7.4. *Dye bleaching for parity time symmetric structures*

In most cases, measurements (in the quantum sense) of observable quantities can be related to decomposing the system being measured into the eigenbasis of some Hermetian operator weighted by its eigenvalues. By virtue of the Hermetianess, the results are real valued. There are clear common exceptions to this, for example, gain or loss media. In these exceptions, materials have the potential to break time reversal symmetry – in essence, a low level of light put backwards through a lossy system will not come out as a bright source on the other side. Parity time (PT-)symmetric materials are a slightly more complex exception to this rule wherein non-Hermitian operators possess *real* eigenvalues. In this case, counter-intuitive behaviors can occur, such as, in the case of light, one way mirroring.[243, 244] The most striking version of this effect occurs in systems consisting of refractive index variations with real and imaginary (gain and loss) oscillation offset by a half-phase from one another. This effect has been predicted to display broadband perfect reflector/transmitter behavior when the amplitude of the real and imaginary variation are matched.[245] This has been demonstrated for a quasi-0D fiber coupled system[246] and, more recently, an analogous behavior for a lossy-only system has also been shown.[247] In this latter demonstration, while asymmetric, the overall performance was rather low and the fabrication method was very involved; therefore, there remains an opportunity for a paradigm development to make large PT responses a reality. Here, polymeric systems, with their flexible positioning, ease of doping, and compatibility with scalable fabrication techniques possess great potential as possible PT patterning media. As the effect may be demonstrated by only adjusting the imaginary component of the dielectric constant, gain dye doping and subsequent bleaching is one viable strategy.

There are numerous examples of laser dyes that provide robust, stable fluorescence to enable gain media. One of the key properties of these dyes are that they possess low photobleaching to allow for long device lifetime; however, as discussed in 5.3, many of these dyes are susceptible to *chemical* bleaching such as through reactions with acid. In the exploration of dye materials for FLaSk-CAP, several acid bleachable dyes have been identified (*e.g.* malachites, cyanines). This allows for a simple translation into

a photopatterning process by use of PAGs. As previously discussed, unlike the case with photoresist, the reactions with the dyes are not photocatalytic and consume the photoacid. This is a critically important feature for the design of a patterning process as the photoactivated spot will not continue to spread indefinitely with time and can remain high resolution. Further, by utilizing a DUV PAG, only exposure to short wave UV or very high intensity MPL will lead to the activation of the PAGs, which means that devices patterned in this way should be stable under room light or even intense gain pump exposure. One dye that has been identified as a particularly strong candidate for PT-symmetric patterning is Nile Red (9-diethylamino-5-benzo[α]phenoxazinone, Figure 7-5), which not only is susceptible to acid bleaching with complete fluorescence suppression, but also undergoes a shift in absorption spectrum upon bleaching. While not a unique behavior, Nile Red's shift places the absorption in the same region as the unbleached dye's emission (peak ~640 nm). This is significant for PT-symmetric materials as this one material can satisfy both the gain and loss requirement for the spatially varying complex index with a single patterning step (though bleachable-dye/absorbing-dye or bleachable-dye/Qdot systems would be not significantly more complex).

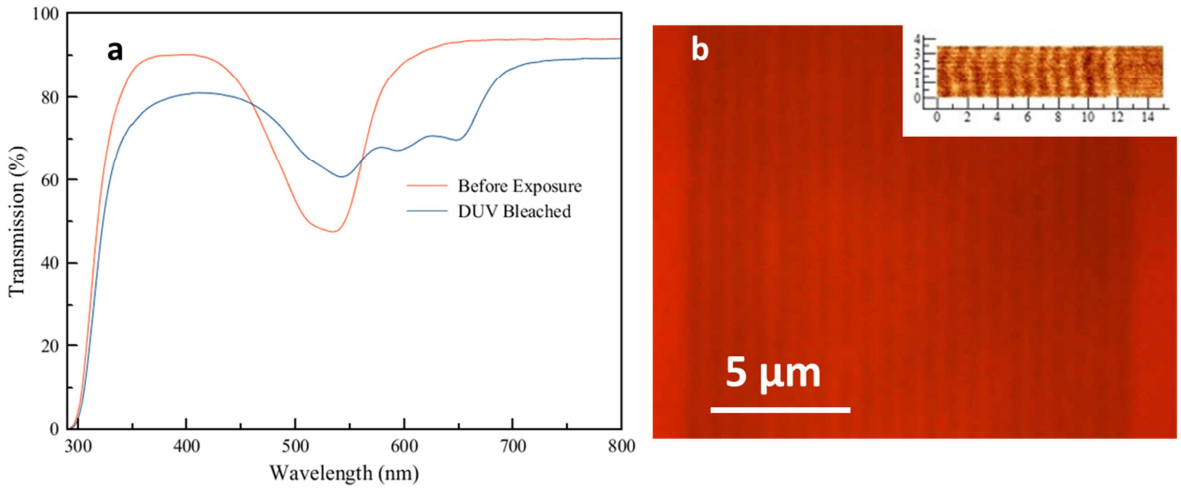

Figure 7-5: (a) UV-vis spectra displaying photoacid bleaching of Nile Red dye inside a polystyrene thin film containing a photoacid generator. Before exposure (blue trace) the dye's peak absorption is ~530 nm while its emission (not shown) peaks at ~640 nm. Upon exposure to a broadband short wavelength source, the emission is visibly observed to quench and the absorption redshifts and broadens (red trace). (b) Fluorescence microscopy of a periodic bleaching pattern written into the polystyrene film by DW. This image shows a PT-symmetric pattern made of 800 nm period lines arrays (illustrated by white lines). Dark contrast represents an acid bleached region from DLW exposure that does not fluoresce under the UV excitation. Each pattern in the larger set is written with a different intensity leading to various line widths. Also shown in inset is the NSOM AFM image of pattern fluorescence under green excitation where the dark contrast indicates bleached dye, revealing 400 nm features. Axes in microns.

Given this (or an analogous) material dispersed homogeneously within a polymer matrix, 3DDW can be utilized to introduce a PT-symmetry prepattern (lacking a pumped system). This has already been applied to create PT-symmetry within a polystyrene-Nile Red- Triphenylsulfonium triflate (90-5-5) system. Figure 7-5b shows a fluorescent microscope image one of a series of PT-symmetric line arrays patterned by DLW within the film. In this image, the dark contrast comes from the non-fluorescing (in fact absorbing), patterned regions. It is important to note that the image was conducted by UV excitation and no further evolution of the pattern was observed, indicating the stability of the system by not only the requirement for DUV but also the extremely low diffusivity of any generated acids within the glassy

polymer matrix at room temperature. Though non-optimized in terms of acid:dye ratio, this system would likely demonstrate PT-symmetry in the red with appropriate green pump intensity.

While a valuable demonstration of patterning capability, significant analysis development will be necessary in order to both observe higher resolution lattices (approaching the wavelength commensurate periodicity necessary for the greatest PT effects). To accomplish this, near-field scanning optical microscopy (NSOM) integrated AFM was utilized. In this technique, an AFM probe consisting of a hollow core optical fiber is used to scan the surface of a photoactive material and capture the near-field transmission or emission, thus enabling near AFM-scale resolution of optical phenomena. Figure 7-5c shows an array of Nile Red lines measured in transmission with NSOM. Here the contrast is switched, with the bright regions indicating bleached (less absorbing) polymer. What can be seen in these images is that the subwavelength resolution unique to nonlinear 3DDW is still possible in this acid-bleach writing mechanism, with observed resolution <400 nm.

While the PT effect has not yet been measured in this system, this is a matter of designing the appropriate experimental apparatus and should be possible in the near future.

7.5. *List of Abbreviations*

(F)PnP	(Focused) proximity-field nanopatterning
(MB/PM)IL	Multibeam/phasemask interference lithography
(N)Pc	(Na)phthalocyanine
(NS)OM	Near-field scanning optical microscopy
AOM	Acousto-optic modulator
BCP	Block copolymer
CA(P/R)	Chemically amplified (photo)resist
DW	Direct write
e-beam	Electron beam
EM	Electromagnetic
FEM	Finite element method
FIB	Focused ion beam
FLaSk	Focused laser spike
GRIN	Gradient index
HMDS	Hexamethyldisilazane
IPA	Isopropyl alcohol
LER	Line edge roughness
LID	Laser induced damage
LSA	Laser spike anneal
MPL	Multiphoton lithography
NA	Numerical aperture
ND	Neutral density
ODT	Order-disorder transition
PAG	Photoacid generator
PDMS	Polydimethylsiloxane
PEB	Post-exposure bake
PGMEA	Proplyene glycol monomethyl ether acetate
PMAA	Polymethylacrylic acid
PS	Polystyrene
PSF	Point spread function
PT	Parity time
PVP	Polyvinyl pyrrilodone
SEM	Scanning electron microscope
SL	Sacrificial layer
SRR	Split-ring resonator
STED	Stimulated emission depletion
THPMA	Tetrahydropyranylmethacrylate

8. References

1. Lemme, M. C.; Bell, D. C.; Williams, J. R.; Stern, L. A.; Baugher, B. W. H.; Jarillo-Herrero, P.; Marcus, C. M. *ACS Nano* **2009,** 3, (9), 2674-2676.

2. Maile, B.; nbsp; E; Henschel, W.; Kurz, H.; Rienks, B.; Polman, R.; Kaars, P. *Jpn. J. Appl. Phys.* **2000,** 39, (Part 1, No. 12B), 6836.

3. van Kouwen, L.; Botman, A.; Hagen, C. W. *Nano Lett.* **2009,** 9, (5), 2149-2152.

4. Randolph, S. J.; Fowlkes, J. D.; Rack, P. D. *Crit. Rev. Solid State Mater. Sci.* **2006,** 31, (3), 55 - 89.

5. Kazuo, F. *Science and Technology of Advanced Materials* **2008,** 9, (1), 014110.

6. Corbierre, M. K.; Beerens, J.; Lennox, R. B. *Chem. Mater.* **2005,** 17, (23), 5774-5779.

7. Stellacci, F.; Bauer, C. A.; Meyer-Friedrichsen, T.; Wenseleers, W.; Alain, V.; Kuebler, S. M.; Pond, S. J. K.; Zhang, Y.; Marder, S. R.; Perry, J. W. *Adv. Mater.* **2002,** 14, (3), 194-198.

8. Grigorescu, A. E.; Hagen, C. W. *Nanotechnology* **2009,** 20, (29), 292001.

9. Kudryashov, V.; Yuan, X. C.; Cheong, W. C.; Radhakrishnan, K. *Microelectron. Eng.* **2003,** 67-68, 306-311.

10. Zhao, X. M.; Xia, Y. N.; Whitesides, G. M. *Adv Mater* **1996,** 8, (10), 837-&.

11. Lin, S. Y.; Fleming, J. G.; Hetherington, D. L.; Smith, B. K.; Biswas, R.; Ho, K. M.; Sigalas, M. M.; Zubrzycki, W.; Kurtz, S. R.; Bur, J. *Nature* **1998,** 394, (6690), 251-253.

12. Qi, M.; Lidorikis, E.; Rakich, P. T.; Johnson, S. G.; Joannopoulos, J. D.; Ippen, E. P.; Smith, H. I. *Nature* **2004,** 429, (6991), 538-542.

13. Lee, J.-H.; Kim, C. H.; Ho, K. M.; Constant, K. *Adv Mater* **2005,** 17, (20), 2481-+.

14. Aoki, K.; Miyazaki, H. T.; Hirayama, H.; Inoshita, K.; Baba, T.; Sakoda, K.; Shinya, N.; Aoyagi, Y. *Nature Materials* **2003,** 2, (2), 117-121.

15. Lee, J.-H.; Kim, Y. S.; Constant, K.; Ho, K. M. *Adv. Mater.* **2007,** 19, (6), 791-+.

16. Robbie, K.; Brett, M. J. *J Vac Sci Technol A* **1997,** 15, (3), 1460-1465.

17. Robbie, K.; Brett, M. J.; Lakhtakia, A. *Nature* **1996,** 384, (6610), 616-616.

18. Ye, D. X.; Yang, Z. P.; Chang, A. S. P.; Bur, J.; Lin, S. Y.; Lu, T. M.; Wang, R. Z.; John, S. *J. Phys. D: Appl. Phys.* **2007,** 40, (9), 2624.

19. Malac, M.; Egerton, R. F.; Brett, M. J.; Dick, B. *Journal of Vacuum Science and Technology B* **1999,** 17, (6), 2671-2674.

20. Takahashi, S.; Suzuki, K.; Okano, M.; Imada, M.; Nakamori, T.; Ota, Y.; Ishizaki, K.; Noda, S. *Nature Materials* **2009,** 8, (9), 721-725.

21. Cheng, C. C.; Scherer, A. *Journal of Vacuum Science and Technology B* **1995,** 13, (6), 2696-2700.

22. Tang, L.; Yoshie, T. *Journal of Vacuum Science and Technology B* **2010,** 28, (2), 301-303.

23. Jacobsen, A. J.; Barvosa-Carter, W.; Nutt, S. *Adv Mater* **2007,** 19, (22), 3892-+.

24. Jacobsen, A. J.; Barvosa-Carter, W.; Nutt, S. *Acta Mater.* **2008,** 56, (6), 1209-1218.

25. Schaedler, T. A.; Jacobsen, A. J.; Torrents, A.; Sorensen, A. E.; Lian, J.; Greer, J. R.; Valdevit, L.; Carter, W. B. *Science* **2011,** 334, (6058), 962-965.

26. Campbell, M.; Sharp, D. N.; Harrison, M. T.; Denning, R. G.; Turberfield, A. J. *Nature* **2000,** 404, (6773), 53-56.

27. Maldovan, M.; Thomas, E. L., *Periodic Materials and Interference Lithography*. Wiley-VCH: Weinheim, 2009.

28. Gorishnyy, T.; Jang, J. H.; Koh, C.; Thomas, E. L. *Appl Phys Lett* **2007,** 91, (12), 121915.

29. Jang, J. H.; Ullal, C. K.; Gorishnyy, T.; Tsukruk, V. V.; Thomas, E. L. *Nano Letters* **2006,** 6, (4), 740-743.

30. Lee, J.-H.; Wang, L. F.; Kooi, S.; Boyce, M. C.; Thomas, E. L. *Nano Letters* **2010,** 10, (7), 2592-2597.

31. Yang, S.; Megens, M.; Aizenberg, J.; Wiltzius, P.; Chaikin, P. M.; Russel, W. B. *Chem. Mater.* **2002,** 14, (7), 2831-2833.

32. Chen, Y. C.; Geddes, J. B.; Iii; Lee, J. T.; Braun, P. V.; Wiltzius, P. *Appl. Phys. Lett.* **2007,** 91, (24), 241103-3.

33. Jeon, S.; Park, J.-U.; Cirelli, R.; Yang, S.; Heitzman, C. E.; Braun, P. V.; Kenis, P. J. A.; Rogers, J. A. *Proc. Natl. Acad. Sci. U.S.A.* **2004,** 101, (34), 12428-12433.

34. Shir, D.; Liao, H. W.; Jeon, S.; Xiao, D.; Johnson, H. T.; Bogart, G. R.; Bogart, K. H. A.; Rogers, J. A. *Nano Lett.* **2008,** 8, (8), 2236-2244.

35. Jeon, S.; Shir, D. J.; Nam, Y. S.; Nidetz, R.; Highland, M.; Cahill, D. G.; Rogers, J. A.; Su, M. F.; El-Kady, I. F.; Christodoulou, C. G.; Bogart, G. R. *Opt. Express* **2007,** 15, (10), 6358-6366.

36. Chang, C. H.; Tian, L.; Hesse, W. R.; Gao, H.; Choi, H. J.; Kim, J. G.; Siddiqui, M.; Barbastathis, G. *Nano Lett.* **2011**, 2533–2537.

37. Di, X.; Kevin, P. C.; Ahmad, H.; Yuankun, L. *Conference on Lasers and Electro-Optics* **2010**, CFF3.

38. Jang, J. H.; Dendukuri, D.; Hatton, T. A.; Thomas, Edwin L.; Doyle, Patrick S. *Angewandte Chemie International Edition* **2007,** 46, (47), 9027-9031.

39. George, M. C.; Nelson, E. C.; Rogers , J. A.; Bruan, P. V. *Angewandte Chemie International Edition* **2009,** 48, (1), 144-148.

40. Lin, Y.; Rivera, D.; Chen, K. P. *Optics Express* **2006,** 14, (2), 887-892.

41. Jia, L.; Thomas, E. L. *Small* **2011,** 7, (21), 2981-2989.

42. Auzelyte, V.; Dais, C.; Farquet, P.; Grutzmacher, D.; Heyderman, L. J.; Luo, F.; Olliges, S.; Padeste, C.; Sahoo, P. K.; Thomson, T.; Turchanin, A.; David, C.; Solak, H. H. *Journal of Micro/Nanolithography, MEMS and MOEMS* **2009,** 8, (2), 021204-10.

43. Lee, J. H.; Singer, J. P.; Thomas, E. L. *Adv Mater* **2012,** 24, (36), 4782-810.

44. Duoss, E. B.; Twardowski, M.; Lewis, J. A. *Adv. Mater.* **2007,** 19, (21), 3485-3489.

45. Gratson, G. M.; García-Santamaría, F.; Lousse, V.; Xu, M.; Fan, S.; Lewis, J. A.; Braun, P. V. *Adv. Mater.* **2006,** 18, (4), 461-465.

46. Lorang, D. J.; Tanaka, D.; Spadaccini, C. M.; Rose, K. A.; Cherepy, N. J.; Lewis, J. A. *Adv. Mater.* **2011,** 23, (43), 5055-5058.

47. Ahn, B. Y.; Lorang, D. J.; Lewis, J. A. *Nanoscale* **2011,** 3, (7), 2700-2702.

48. Ahn, B. Y.; Shoji, D.; Hansen, C. J.; Hong, E.; Dunand, D. C.; Lewis, J. A. *Adv. Mater.* **2010,** 22, (20), 2251-2254.

49. Wu, W.; DeConinck, A.; Lewis, J. A. *Adv. Mater.* **2011,** 23, (24), H178-H183.

50. LaFratta, C. N.; Fourkas, J. T.; Baldacchini, T.; Farrer, R. A. *Angew. Chem. Int. Ed.* **2007,** 46, 6238-6258.

51. Haske, W.; Chen, V. W.; Hales, J. M.; Dong, W.; Barlow, S.; Marder, S. R.; Perry, J. W. *Opt. Express* **2007,** 15, (6), 3426-3436.

52. Sun, C.; Fang, N.; Wu, D. M.; Zhang, X. *Sensors and Actuators A Physical* **2005,** 121, (1), 113-120.

53. Xia, C.; Lee, H.; Fang, N. *J. Micromech. Microeng.* **2010,** 20, (8), 085030.

54. Maruo, S.; Ikuta, K. *Appl. Phys. Lett.* **2000,** 76, (19), 2656-2658.

55. Fischer, J.; von Freymann, G.; Wegener, M. *Adv. Mater.* **2010,** 22, (32), 3578-3582.

56. Farsari, M.; Filippidis, G.; Fotakis, C. *Optics Letters* **2005,** 30, (23), 3180-3182.

57. Deubel, M.; von Freymann, G.; Wegener, M.; Pereira, S.; Busch, K.; Soukoulis, C. M. *Nat. Mat.* **2004,** 3, (7), 444-447.

58. Ma, M.; Titievsky, K.; Thomas, E. L.; Rutledge, G. C. *Nano Lett.* **2009,** 9, (4), 1678-1683.

59. Thiel, M.; Fischer, J.; von Freymann, G.; Wegener, M. *Appl. Phys. Lett.* **2010,** 97, (22), 221102-3.

60. Seet, K. K.; Juodkazis, S.; Jarutis, V.; Misawa, H. *Appl. Phys. Lett.* **2006,** 89, (2), 024106-3.

61. Malinauskas, M.; Zukauskas, A.; Biekauskaite, G.; Gadonas, R.; Juodkazis, S. *Opt. Express* **2010,** 18, (10), 10209-10221.

62. Scott, T. F.; Kowalski, B. A.; Sullivan, A. C.; Bowman, C. N.; McLeod, R. R. *Science* **2009,** 324, (5929), 913-917.

63. Gansel, J. K.; Thiel, M.; Rill, M. S.; Decker, M.; Bade, K.; Saile, V.; von Freymann, G.; Linden, S.; Wegener, M. *Science* **2009,** 325, 1513.

64. Bückmann, T.; Stenger, N.; Kadic, M.; Kaschke, J.; Frölich, A.; Kennerknecht, T.; Eberl, C.; Thiel, M.; Wegener, M. *Adv Mater* **2012**, DOI: 10.1002/adma.201200584.

65. Kadic, M.; Bückmann, T.; Stenger, N.; Thiel, M.; Wegener, M. *Appl Phys Lett* **2012,** 100, 191901.

66. Li, L.; Gattass, R. R.; Gershgoren, E.; Hwang, H.; Fourkas, J. T. *Science* **2009,** 324, (5929), 910-913.

67. Sun, H. B.; Kawata, S., Two-photon photopolymerization and 3D lithographic microfabrication. In *Nmr - 3d Analysis - Photopolymerization*, Springer-Verlag Berlin: Berlin, 2004; Vol. 170, pp 169-273.

68. Teh, W. H.; Durig, U.; Drechsler, U.; Smith, C. G.; Guntherodt, H. J. *J. Appl. Phys.* **2005,** 97, (5), 054907-11.

69. Witzgall, G.; Vrijen, R.; Yablonovitch, E.; Doan, V.; Schwartz, B. J. *Opt. Lett.* **1998,** 23, (22), 1745-1747.

70. Yao-Yu, C.; Nobuyuki, T.; Takuo, T.; Xuan-Ming, D.; Satoshi, K. *Small* **2009,** 5, (10), 1144-1148.

71. Maruo, S.; Saeki, T. *Opt. Express* **2008,** 16, (2), 1174-1179.

72. Baldacchini, T.; Pons, A.-C.; Pons, J.; LaFratta, C.; Fourkas, J.; Sun, Y.; Naughton, M. *Opt. Express* **2005,** 13, (4), 1275-1280.

73. Shobha, S.; Edward, P. F.; Xavier, V.; Mark, T. S.; Paras, N. P. *Adv. Mater.* **2010,** 9999, (9999), NA.

74. Tanaka, T. *Journal of Laser Micro/Nanoengineering* **2008,** 3, (3), 5.

75. Formanek, F.; Takeyasu, N.; Tanaka, T.; Chiyoda, K.; Ishikawa, A.; Kawata, S. *Opt. Express* **2006,** 14, (2), 800-809.

76. Gansel, J. K.; Thiel, M.; Rill, M. S.; Decker, M.; Bade, K.; Saile, V.; von Freymann, G.; Linden, S.; Wegener, M. *Science* **2009,** 325, (5947), 1513-5.

77. Shukla, S.; Vidal, X.; Furlani, E. P.; Swihart, M. T.; Kim, K.-T.; Yoon, Y.-K.; Urbas, A.; Prasad, P. N. *ACS Nano* **2011,** 5, (3), 1947-1957.

78. Baldacchini, T.; Pons, A.-C.; Pons, J.; LaFratta, C.; Fourkas, J.; Sun, Y.; Naughton, M. *Optics Express* **2005,** 13, (4), 1275-1280.

79. Xu, B.-B.; Xia, H.; Niu, L.-G.; Zhang, Y.-L.; Sun, K.; Chen, Q.-D.; Xu, Y.; Lv, Z.-Q.; Li, Z.-H.; Misawa, H.; Sun, H.-B. *Small* **2010,** 6, (16), 1762-1766.

80. Park, S. H.; Lim, T. W.; Yang, D.-Y.; Kim, R. H.; Lee, K.-S. *Macromolecular Research* **2006,** 14, (5), 5.

81. Tan, D.; Li, Y.; Qi, F.; Yang, H.; Gong, Q.; Dong, X.; Duan, X. *Appl. Phys. Lett.* **2007,** 90, (7), 071106-3.

82. Takada, K.; Sun, H.-B.; Kawata, S. *Micromachining Technology for Micro-Optics and Nano-Optics IV* **2006,** 6110, 61100A-7.

83. Formanek, F.; Takeyasu, N.; Tanaka, T.; Chiyoda, K.; Ishikawa, A.; Kawata, S. *Plasmonics: Nanoimaging, Nanofabrication, and their Applications II* **2006,** 6324, 63240T-6.

84. Ye, Y.-H.; LeBlanc, F.; Hache, A.; Truong, V.-V. *Appl. Phys. Lett.* **2001,** 78, (1), 52-54.

85. S. B. Juhl; Chan, E. P.; Ha, Y. H.; Maldovan, M.; Brunton, J.; Ward, V.; Dokland, T.; Kalmakoff, J.; Farmer, B.; Thomas, E. L.; Vaia, R. A. *Adv. Funct. Mater.* **2006,** 16, (8), 1086-1094.

86. Hayward, R. C.; Saville, D. A.; Aksay, I. A. *Nature* **2000,** 404, (6773), 56-59.

87. Harris, N.; et al. *Nanotechnology* **2007,** 18, (36), 365301.

88. Jianping, G.; Yongxing, H.; Yadong, Y. *Angew. Chem. Int. Ed.* **2007,** 46, (39), 7428-7431.

89. Rinne, S. A.; Garcia-Santamaria, F.; Braun, P. V. *Nat. Phot.* **2008,** 2, (1), 52-56.

90. Still, T.; Cheng, W.; Retsch, M.; Jonas, U.; Fytas, G. *J. Phys.: Condens. Matter* **2008,** 20, (40), 404203.

91. Thomas, E. L.; Gorishnyy, T.; Maldovan, M. *Nature Materials* **2006,** 5, (10), 773-774.

92. Yin, J.; Retsch, M.; Lee, J.-H.; Thomas, E. L.; Boyce, M. C. *Langmuir* **2011,** 27, (17), 10492-10500.

93. Talapin, D. V.; Shevchenko, E. V.; Bodnarchuk, M. I.; Ye, X.; Chen, J.; Murray, C. B. *Nature* **2009,** 461, (7266), 964-967.

94. Dong, A.; Chen, J.; Vora, P. M.; Kikkawa, J. M.; Murray, C. B. *Nature* **2010,** 466, (7305), 474-477.

95. Grego, S.; Jarvis, T. W.; Stoner, B. R.; Lewis, J. S. *Langmuir* **2005,** 21, (11), 4971-4975.

96. Auyeung, E.; Cutler, J. I.; Macfarlane, R. J.; Jones, M. R.; Wu, J. S.; Liu, G.; Zhang, K.; Osberg, K. D.; Mirkin, C. A. *Nat Nanotechnol* **2012,** 7, (1), 24-28.

97. Macfarlane, R. J.; Lee, B.; Jones, M. R.; Harris, N.; Schatz, G. C.; Mirkin, C. A. *Science* **2011,** 334, (6053), 204-208.

98. Jones, M. R.; Macfarlane, R. J.; Lee, B.; Zhang, J. A.; Young, K. L.; Senesi, A. J.; Mirkin, C. A. *Nature Materials* **2010,** 9, (11), 913-917.

99. Bates, F. S.; Fredrickson, G. H. *Physics Today* **1999,** 52, (2), 32-38.

100. Urbas, A. M.; Maldovan, M.; DeRege, P.; Thomas, E. L. *Adv. Mater.* **2002,** 14, (24), 1850-1853.

101. Park, C.; Yoon, J.; Thomas, E. L. *Polymer* **2003,** 44, (22), 6725-6760.

102. Mavroudis, A.; Avgeropoulos, A.; Hadjichristidis, N.; Thomas, E. L.; Lohse, D. J. *Chem. Mater.* **2003,** 15, (10), 1976-1983.

103. Bates, F. S.; Fredrickson, G. H. *Annu. Rev. Phys. Chem.* **1990,** 41, (1), 525-557.

104. Chiang, Y. W.; Ho, R. M.; Thomas, E. L.; Burger, C.; Hsiao, B. S. *Adv. Funct. Mater.* **2009,** 19, (3), 448-459.

105. Zheng, W.; Wang, Z.-G. *Macromolecules* **1995,** 28, (21), 7215-7223.

106. Bockstaller, M.; Kolb, R.; Thomas, E. L. *Adv. Mater.* **2001,** 13, (23), 1783-1786.

107. Bockstaller, M.; Mickiewicz, R. A.; Thomas, E. L. *Adv Mater* **2005,** 17, (11), 1331-1349.

108. Kang, Y.; Walish, J. J.; Gorishnyy, T.; Thomas, E. L. *Nature Materials* **2007,** 6, (12), 957-960.

109. Urbas, A. M.; Thomas, E. L.; Kriegs, H.; Fytas, G.; Penciu, R. S.; Economou, L. N. *Phys. Rev. Lett.* **2003,** 90, (10), 108302.

110. Urbas, A.; Sharp, R.; Fink, Y.; Thomas, E. L.; Xenidou, M.; Fetters, L. J. *Adv. Mater.* **2000,** 12, (11), 812-814.

111. Haske, W.; Chen, V. W.; Hales, J. M.; Dong, W.; Barlow, S.; Marder, S. R.; Perry, J. W. *Optics Express* **2007,** 15, (6), 3426-3436.

112. Nelson, E. C.; Garcia-Santamaria, F.; Braun, P. V. *Adv. Funct. Mater.* **2008,** 18, (13), 1983-1989.

113. Staude, I.; Decker, M.; Ventura, M. J.; Jagadish, C.; Neshev, D. N.; Gu, M.; Kivshar, Y. S. *Adv Mater* **2013,** 25, (9), 1260-4.

114. Yang, J. K. W.; Jung, Y. S.; Chang, J. B.; Mickiewicz, R. A.; Alexander-Katz, A.; Ross, C. A.; Berggren, K. K. *Nature Nanotechnology* **2010,** 5, (4), 256-260.

115. J. Scrimgeour; D. N. Sharp; C. F. Blanford; O. M. Roche; R. G. Denning; Turberfield, A. J. *Adv. Mater.* **2006,** 18, (12), 1557-1560.

116. George, M. C.; Mohraz, A.; Piech, M.; Bell, N. S.; Lewis, J. A.; Braun, P. V. *Adv. Mater.* **2009,** 21, (1), 66-70.

117. Zarzar, L. D.; Kim, P.; Kolle, M.; Brinker, C. J.; Aizenberg, J.; Kaehr, B. *Angew. Chem. Int. Ed.* **2011,** 50, (40), 9356-9360.

118. S. A. Pruzinsky; Braun, P. V. *Adv. Funct. Mater.* **2005,** 15, (12), 1995-2004.

119. Ramanan, V.; Nelson, E.; Brzezinski, A.; Braun, P. V.; Wiltzius, P. *Appl. Phys. Lett.* **2008,** 92, (17), 173304-3.

120. Li, M.; Douki, K.; Goto, K.; Li, X.; Coenjarts, C.; Smilgies, D. M.; Ober, C. K. *Chem. Mater.* **2004,** 16, (20), 3800-3808.

121. Zhang, S.; Fan, W.; Minhas, B. K.; Frauenglass, A.; Malloy, K. J.; Brueck, S. R. J. *Phys. Rev. Lett.* **2005,** 94, (3), 037402.

122. Stoykovich, M. P.; Kang, H.; Daoulas, K. C.; Liu, G.; Liu, C.-C.; de Pablo, J. J.; Müller, M.; Nealey, P. F. *ACS Nano* **2007,** 1, (3), 168-175.

123. Edwards, E. W.; Montague, M. F.; Solak, H. H.; Hawker, C. J.; Nealey, P. F. *Adv. Mater.* **2004,** 16, (15), 1315-1319.

124. Son, J. G.; Chang, J.-B.; Berggren, K. K.; Ross, C. A. *Nano Lett.* **2011,** 11, (11), 5079-5084.

125. Ross, C. A.; Jung, Y. S.; Chuang, V. P.; Son, J. G.; Gotrik, K. W.; Mickiewicz, R. A.; Yang, J. K. W.; Chang, J. B.; Berggren, K. K.; Gwyther, J.; Manners, I. *Proceedings of SPIE* **2010,** 7637, 76370H-7.

126. Jung, Y. S.; Jung, W.; Ross, C. A. *Nano Lett.* **2008,** 8, (9), 2975-2981.

127. Osuji, C.; Ferreira, P. J.; Mao, G. P.; Ober, C. K.; Vander Sande, J. B.; Thomas, E. L. *Macromolecules* **2004,** 37, (26), 9903-9908.

128. Xu, T.; Zhu, Y. Q.; Gido, S. P.; Russell, T. P. *Macromolecules* **2004,** 37, (7), 2625-2629.

129. Angelescu, D. E.; Waller, J. H.; Adamson, D. H.; Deshpande, P.; Chou, S. Y.; Register, R. A.; Chaikin, P. M. *Adv Mater* **2004,** 16, (19), 1736-+.

130. Berry, B. C.; Bosse, A. W.; Douglas, J. F.; Jones, R. L.; Karim, A. *Nano Letters* **2007,** 7, (9), 2789-2794.

131. Hashimoto, T.; Bodycomb, J.; Funaki, Y.; Kimishima, K. *Macromolecules* **1999,** 32, (3), 952-954.

132. Angelescu, D. E.; Waller, J. H.; Adamson, D. H.; Register, R. A.; Chaikin, P. M. *Adv Mater* **2007,** 19, (18), 2687-+.

133. Singh, G.; Yager, K. G.; Berry, B.; Kim, H.-C.; Karim, A. *ACS Nano* **2012,** 6, (11), 10335-10342.

134. Seppala, J. E.; Lewis, R. L.; Epps, T. H. *ACS Nano* **2012**.

135. De Rosa, C.; Park, C.; Thomas, E. L.; Lotz, B. *Nature* **2000,** 405, (6785), 433-437.

136. Park, C.; De Rosa, C.; Thomas, E. L. *Macromolecules* **2001,** 34, (8), 2602-2606.

137. Cho, C. Y.; Moon, J. H. *Adv Mater* **2011,** 23, (26), 2971-5.

138. Ye, J.; Zentel, R.; Arpiainen, S.; Ahopelto, J.; Jonsson, F.; Romanov, S. G.; Sotomayor Torres, C. M. *Langmuir* **2006,** 22, (17), 7378-7383.

139. Hung, H.-J.; Yang, P.-C.; Liu, J.-H. *J. Appl. Polym. Sci.* **2008,** 109, (6), 3776-3785.

140. Jones, B. H.; Lodge, T. P. *ACS Nano* **2011**.

141. Arsenault, A. C.; Rider, D. A.; Tetreault, N.; Chen, J. I. L.; Coombs, N.; Ozin, G. A.; Manners, I. *J Am Chem Soc* **2005,** 127, (28), 9954-9955.

142. Bautista, G.; Romero, M. J.; Tapang, G.; Daria, V. R. *Opt. Commun.* **2009,** 282, (18), 3746-3750.

143. Fan, K. B.; Strikwerda, A. C.; Tao, H.; Averitt, R. D.; Zhang, X. In *3D STAND-UP METAMATERIALS WITH A PURELY MAGNETIC RESONANCE AT TERAHERTZ FREQUENCIES*, Mems 2010: 23rd Ieee Internat. Conf. on Micro Electro Mech. Sys., Tech. Dig., New York, 2010; Ieee: New York, 2010; pp 843-846.

144. Burckel, D. B.; Wendt, J. R.; Ten Eyck, G. A.; Ginn, J. C.; Ellis, A. R.; Brener, I.; Sinclair, M. B. *Adv. Mater.* **2010,** 22, (44), 5053-5057.

145. Cho, J. H.; Keung, M. D.; Verellen, N.; Lagae, L.; Moshchalkov, V. V.; Van Dorpe, P.; Gracias, D. H. *Small* **2011,** 7, (14), 1943-8.

146. Singer, J. P.; Kooi, S. E.; Thomas, E. L. *Nanoscale* **2011,** 3, (7), 2730-8.

147. Lee, J.-H.; Kim, C.-H.; Kim, Y.-S.; Ho, K.-M.; Constant, K.; Oh, C. H. *Appl. Phys. Lett.* **2006,** 88, (18), 181112.

148. Costas, M. S.; Thomas, K.; Jiangfeng, Z.; Maria, K.; Eleftherios, N. E. *phys. stat. sol. (b)* **2007,** 244, (4), 1181-1187.

149. Gat, A.; Gerzberg, L.; Gibbons, J. F.; Magee, T. J.; Peng, J.; Hong, J. D. *Appl. Phys. Lett.* **1978,** 33, (8), 775-778.

150. Chong, Y. F.; Gossmann, H. J. L.; Pey, K. L.; Thompson, M. O.; Wee, A. T. S.; Tung, C. H. *IEEE T. Electron Dev.* **2004,** 51, (5), 669-676.

151. Shima, A.; Hiraiwa, A. *Jpn. J. Appl. Phys.* **2006,** 45, (7), 5708.

152. Jaw-Luen, T.; Ming-An, T. *CLEO-PR 2007* **2007**, ThP_082.

153. Jung, B.; Sha, J.; Paredes, F.; Ober, C. K.; Thompson, M. O.; Chandhok, M.; Younkin, T. R. *Proc. of SPIE* **2010,** 7639, 76390L-9.

154. Trice, J.; Thomas, D.; Favazza, C.; Sureshkumar, R.; Kalyanaraman, R. *Physical Review B* **2007,** 75, (23), 235439.

155. Du, B.; Xie, F.; Wang, Y.; Yang, Z.; Tsui, O. K. C. *Langmuir* **2002,** 18, (22), 8510-8517.

156. Brochard, F. *Langmuir* **1989,** 5, (2), 432-438.

157. Ludviksson, V.; Lightfoot, E. N. *AlChE J.* **1971,** 17, (5), 1166-1173.

158. Darhuber, A. A.; Valentino, J. P.; Davis, J. M.; Troian, S. M.; Wagner, S. *Appl. Phys. Lett.* **2003,** 82, (4), 657-659.

159. McLeod, E.; Liu, Y.; Troian, S. M. *Phys. Rev. Lett.* **2011,** 106, (17), 175501.

160. Dietzel, M.; Troian, S. M. *J. Appl. Phys.* **2010,** 108, (7), 074308-17.

161. Jin, S. H.; Dunham, S. N.; Song, J.; Xie, X.; Kim, J.-h.; Lu, C.; Islam, A.; Du, F.; Kim, J.; Felts, J.; Li, Y.; Xiong, F.; Wahab, M. A.; Menon, M.; Cho, E.; Grosse, K. L.; Lee, D. J.; Chung, H. U.; Pop, E.; Alam, M. A.; King, W. P.; Huang, Y.; Rogers, J. A. *Nat Nano* **2013,** 8, (5), 347-355.

162. Dammel, R. R.; Norwood, R. A. **1996**, 754-769.

163. Rathsack, B. M.; Tabery, C. E.; Philbin, C. E.; Willson, C. G. In *Lithography Simulation of Sub-0.30 Micron Resist Features for Photomask Fabrication using I-line Optical Pattern Generators*, BACUS Symposium on Photomask Technology, 1999; SPIE: 1999.

164. Shanks, H. R.; Maycock, P. D.; Sidles, P. H.; Danielson, G. C. *Physical Review* **1963,** 130, (5), 1743-1748.

165. Jellison, J. G. E.; Modine, F. A. *Appl. Phys. Lett.* **1982,** 41, (2), 180-182.

166. Lo, H. W.; Compaan, A. *J. Appl. Phys.* **1980,** 51, (3), 1565-1568.

167. Mori, K.; Hasegawa, H.; Hashimoto, T. *Polymer* **1990,** 31, (12), 2368-2376.

168. Stoykovich, M. P.; Kang, H.; Daoulas, K.; Liu, G.; Liu, C. C.; de Pablo, J. J.; Muller, M.; Nealey, P. F. *ACS Nano* **2007,** 1, (3), 168-75.

169. Son, J. G.; Chang, J.-B.; Berggren, K. K.; Ross, C. A. *Nano Lett.* **2011**.

170. Ross, C. A.; Jung, Y. S.; Chuang, V. P.; Son, J. G.; Gotrik, K. W.; Mickiewicz, R. A.; Yang, J. K. W.; Chang, J. B.; Berggren, K. K.; Gwyther, J.; Manners, I. *Alternative Lithographic Technologies II* **2010,** 7637, 76370H-7.

171. Ruiz, R.; Ruiz, N.; Zhang, Y.; Sandstrom, R. L.; Black, C. T. *Adv. Mater.* **2007,** 19, (16), 2157-2162.

172. Cheng, J. Y.; Ross, C. A.; Thomas, E. L.; Smith, H. I.; Vancso, G. J. *Appl. Phys. Lett.* **2002,** 81, (19), 3657-3659.

173. Bosworth, J. K.; Black, C. T.; Ober, C. K. *ACS Nano* **2009,** 3, (7), 1761-1766.

174. Mita, K.; Tanaka, H.; Saijo, K.; Takenaka, M.; Hashimoto, T. *Macromolecules* **2007,** 40, (16), 5923-5933.

175. Yager, K. G.; Fredin, N. J.; Zhang, X.; Berry, B. C.; Karim, A.; Jones, R. L. *Soft Matter* **2010,** 6, (1), 92-99.

176. Singh, G.; Yager, K. G.; Smilgies, D.-M.; Kulkarni, M. M.; Bucknall, D. G.; Karim, A. *Macromolecules* **2012,** 45, (17), 7107-7117.

177. Singh, G.; Batra, S.; Zhang, R.; Yuan, H.; Yager, K. G.; Cakmak, M.; Berry, B.; Karim, A. *ACS Nano* **2013**.

178. Lee, J.-H.; Veysset, D.; Singer, J. P.; Retsch, M.; Saini, G.; Pezeril, T.; Nelson, K. A.; Thomas, E. L. *Nat Commun* **2012,** 3, 1164.

179. Gotrik, K. W.; Hannon, A. F.; Son, J. G.; Keller, B.; Alexander-Katz, A.; Ross, C. A. *ACS Nano* **2012**.

180. Fetters, L. J.; Lohse, D. J.; Richter, D.; Witten, T. A.; Zirkel, A. *Macromolecules* **1994,** 27, (17), 4639-4647.

181. Zhang, H.; Zhang, J.; Yang, Y.; Zhou, X. *The Journal of Chemical Physics* **1997,** 106, (2), 784-792.

182. Bosse, A. W.; Douglas, J. F.; Berry, B. C.; Jones, R. L.; Karim, A. *Phys. Rev. Lett.* **2007,** 99, (21), 216101.

183. Pujari, S.; Keaton, M. A.; Chaikin, P. M.; Register, R. A. *Soft Matter* **2012,** 8, (19), 5358-5363.

184. Angelescu, D. E.; Waller, J. H.; Adamson, D. H.; Deshpande, P.; Chou, S. Y.; Register, R. A.; Chaikin, P. M. *Adv. Mater.* **2004,** 16, (19), 1736-1740.

185. Pu, Z., Polymer Data Handbook. In Mark, J. E., Ed. Oxford Univ. Press: NY, 2009.

186. Jung-Dae, C.; Hyoung-Tae, J.; Young-Sik, P.; Jin-Who, H. *Macromol. Mater. Eng.* **2006,** 291, (9), 1155-1163.

187. Yoshihisa, S.; Atsushi, S.; Yoshiyuki, K.; Satoshi, M.; Nao, H.; William D, W. *J. Photopolym. Sci. Technol.* **2005,** 18, (1), 125-132.

188. Sensu, Y.; Sekiguchi, A.; Mori, S.; Honda, N. *Proc. of SPIE* **2005,** 5753, 1170-1185.

189. Li, T.-L. *J. Comput. Phys.* **2001,** 173, (1), 348-363.

190. Petersen, J. S.; Mack, C. A.; Thackeray, J. W.; Sinta, R. F.; Fedynyshyn, T. H.; Mori, J. M.; Byers, J. D.; Miller, D. A. *Spill Sci. Technol. Bull.* **1995,** 2438, 153-166.

191. Ferguson, R. A.; Hutchinson, J. M.; Spence, C. A.; Neureuther, A. R. *Journal of Vacuum Science & Technology B: Microelectronics and Nanometer Structures* **1990,** 8, (6), 1423-1427.

192. Svelto, O., *Principles of Lasers*. 5th ed.; Springer Science+Business Media LLC 2012: 2010.

193. Ullal, C. K.; Maldovan, M.; Thomas, E. L.; Chen, G.; Han, Y.-J.; Yang, S. *Appl. Phys. Lett.* **2004,** 84, (26), 5434-5436.

194. Yang, Y.; Liu, A. Q.; Chin, L. K.; Zhang, X. M.; Tsai, D. P.; Lin, C. L.; Lu, C.; Wang, G. P.; Zheludev, N. I. *Nat Commun* **2012,** 3, 651.

195. Zhu, X.; Xu, Y.; Yang, S. *Opt. Express* **2007,** 15, (25), 16546-16560.

196. Denning, R. G.; Blanford, C. F.; Urban, H.; Bharaj, H.; Sharp, D. N.; Turberfield, A. J. *Adv. Funct. Mater.* **2011,** 21, (9), 1593-1601.

197. Meisel, D. C.; Diem, M.; Deubel, M.; Pérez-Willard, F.; Linden, S.; Gerthsen, D.; Busch, K.; Wegener, M. *Adv. Mater.* **2006,** 18, (22), 2964-2968.

198. Hayek, A.; Xu, Y.; Okada, T.; Barlow, S.; Zhu, X.; Moon, J. H.; Marder, S. R.; Yang, S. *J. Mater. Chem.* **2008,** 18, (28), 3316-3318.

199. Jiguet, S.; Bertsch, A.; Judelewicz, M.; Hofmann, H.; Renaud, P. *Microelectron. Eng.* **2006,** 83, (10), 1966-1970.

200. Ovsianikov, A.; Viertl, J.; Chichkov, B.; Oubaha, M.; MacCraith, B.; Sakellari, I.; Giakoumaki, A.; Gray, D.; Vamvakaki, M.; Farsari, M.; Fotakis, C. *ACS Nano* **2008,** 2, (11), 2257-2262.

201. Xu, Y.; Zhu, X.; Dan, Y.; Moon, J. H.; Chen, V. W.; Johnson, A. T.; Perry, J. W.; Yang, S. *Chem. Mater.* **2008,** 20, (5), 1816-1823.

202. Braun, P. V.; Wiltzius, P. *Nature* **1999,** 402, (6762), 603-604.

203. García-Santamaría, F.; Xu, M.; Lousse, V.; Fan, S.; Braun, P. V.; Lewis, J. A. *Adv. Mater.* **2007,** 19, (12), 1567-1570.

204. Zhou, W.; Kuebler, S. M.; Braun, K. L.; Yu, T.; Cammack, J. K.; Ober, C. K.; Perry, J. W.; Marder, S. R. *Science* **2002,** 296, (5570), 1106-1109.

205. Yu, T.; Ober, C. K.; Kuebler, S. M.; Zhou, W.; Marder, S. R.; Perry, J. W. *Adv. Mater.* **2003,** 15, (6), 517-521.

206. Ito, H. *J. Photopolym. Sci. Technol.* **2008,** 21, (4), 475-491.

207. Ismailova, E.; Tiron, R.; Chochos, C. L.; Brochon, C.; Bandelier, P.; Perret, D.; Sourd, C.; Brault, C.; Serra, C. A.; Schlatter, G.; Hadziioannou, G. *Microelectron. Eng.* **2009,** 86, (4–6), 796-799.

208. Nozaki, K.; Yano, E. *FUJITSU Science and Technology Journal* **2002,** 38, (1), 3-12.

209. Takechi, S.; Takahashi, M.; Kotachi, A.; Nozaki, K.; Yano, E.; Hanyu, I. *J. Photopolym. Sci. Technol.* **1996,** 9, (3), 475-488.

210. Wasielewski, M. R. *Chem. Rev.* **1992,** 92, (3), 435-461.

211. Schafer, K. J.; Hales, J. M.; Balu, M.; Belfield, K. D.; Van Stryland, E. W.; Hagan, D. J. *Journal of Photochemistry and Photobiology A: Chemistry* **2004,** 162, (2–3), 497-502.

212. Meyer, J. R.; Kruer, M. R.; Bartoli, F. J. *J. Appl. Phys.* **1980,** 51, (10), 5513-5522.

213. Widengren, J.; Rigler, R. *Bioimaging* **1996,** 4, (3), 149-157.

214. Pan, E.-Y.; Pu, N.-W.; Tong, Y.-P.; Yau, H.-F. *Journal of Medical and Biological Engineering* **2003,** 23, (2).

215. Kondo, T.; Juodkazis, S.; Misawa, H. *Appl. Phys. A-Mater.* **2005,** 81, (8), 1583-1586.

216. LaFratta, C. N. Multiphoton Absorption Polymerization: Issues and Solutions. University of Maryland, College Park, 2006.

217. Mohanty, J.; Palit, D. K.; Mittal, J. P. *Proc. Ind. Nat. Sci. Acad. A* **2000,** 66, (2), 303-315.

218. Feng, R.; Farris, R. J. *J. Micromech. Microeng.* **2003,** 13, (1), 80.

219. Trabattoni, A.; Maini, L.; Benedek, G. *Opt. Express* **2012,** 20, (27), 28267-28272.

220. Ueda, K.; Dotera, T.; Gemma, T. *Physical Review B* **2007,** 75, (19), 11.

221. Steurer, W.; Sutter-Widmer, D. *J. Phys. D: Appl. Phys.* **2007,** 40, (13), R229-R247.

222. Bita, I.; Choi, T.; Walsh, M. E.; Smith, H. I.; Thomas, E. L. *Adv. Mater.* **2007,** 19, (10), 1403-1407.

223. Xu, J.; Ma, R.; Wang, X.; Tam, W. Y. *Opt. Express* **2007,** 15, (7), 4287-4295.

224. Neil, M. A. A.; Juskaitis, R.; Wilson, T.; Laczik, Z. J.; Sarafis, V. *Opt. Lett.* **2000,** 25, (4), 245-247.

225. Harke, B.; Keller, J.; Ullal, C. K.; Westphal, V.; Schönle, A.; Hell, S. W. *Opt. Express* **2008,** 16, (6), 4154-4162.

226. Klar, T. A.; Engel, E.; Hell, S. W. *Phys. Rev. E* **2001,** 64, (6), 066613.

227. Mühlberger, M.; Bergmair, I.; Schwinger, W.; Gmainer, M.; Schöftner, R.; Glinsner, T.; Hasenfuß, C.; Hingerl, K.; Vogler, M.; Schmidt, H.; Kley, E. B. *Microelectron. Eng.* **2007,** 84, (5-8), 925-927.

228. Ishii, T.; Tanaka, H.; Kuramochi, E.; Tamamura, T. *Jpn. J. Appl. Phys.* 37, (Copyright (C) 1998 Publication Board, Japanese Journal of Applied Physics), 7202.

229. Mårtensson, T.; Carlberg, P.; Borgström, M.; Montelius, L.; Seifert, W.; Samuelson, L. *Nano Lett.* **2004,** 4, (4), 699-702.

230. Yang, Y.-L.; Hsu, C.-C.; Chang, T.-L.; Kuo, L.-S.; Chen, P.-H. *Appl. Surf. Sci.* **2010,** 256, (11), 3683-3687.

231. He, M.; Zhang, Q.; Zeng, X.; Cui, D.; Chen, J.; Li, H.; Wang, J.; Song, Y. *Adv Mater* **2013,** 25, (16), 2291-5.

232. Bray, D. F.; Bagu, J.; Koegler, P. *Microsc. Res. Tech.* **1993,** 26, (6), 489-495.

233. Marcilla, A.; Beltrán, M. *Polym. Degrad. Stab.* **1995,** 50, (1), 117-124.

234. Chen, Y. C. FABRICATION AND CHARACTERIZATION OF THREE DIMENSIONAL PHOTONIC CRYSTALS GENERATED BY MULTIBEAM INTERFERENCE LITHOGRAPHY. University of Illinois Urbana-Champaigne, 2009.

235. Ito, H.; Breyta, G.; Hofer, D.; Sooriyakumaran, R.; Petrillo, K.; Seeger, D. *J. Photopolym. Sci. Technol.* **1994,** 7, (3), 433-447.

236. Petel, O. E.; Jetté, F. X.; Goroshin, S.; Frost, D. L.; Ouellet, S. *Shock Waves* **2011,** 21, (3), 215-224.

237. Zhuang, S.; Ravichandran, G.; Grady, D. E. *Journal of the Mechanics and Physics of Solids* **2003,** 51, (2), 245-265.

238. Molinari, A.; Daraio, C. *Phys. Rev. E* **2009,** 80, (5), 056602.

239. Gorishnyy, T. Hypersonic Phononic Crystals Massachusetts Institute of Technology, Cambridge, 2007.

240. Khelif, A.; Aoubiza, B.; Mohammadi, S.; Adibi, A.; Laude, V. *Phys. Rev. E* **2006,** 74, (4), 046610.

241. Miyashita, T. *Meas. Sci. Technol.* **2005,** 16, (5), R47-R63.

242. Yang, S.; Page, J. H.; Liu, Z.; Cowan, M. L.; Chan, C. T.; Sheng, P. *Phys. Rev. Lett.* **2004,** 93, (2), 024301.

243. Kalish, S.; Lin, Z.; Kottos, T. *Physical Review A* **2012,** 85, (5), 055802.

244. Ramezani, H.; Kottos, T.; El-Ganainy, R.; Christodoulides, D. N. *Physical Review A* **2010,** 82, (4), 043803.

245. Lin, Z.; Ramezani, H.; Eichelkraut, T.; Kottos, T.; Cao, H.; Christodoulides, D. N. *Phys. Rev. Lett.* **2011,** 106, (21), 213901.

246. Regensburger, A.; Bersch, C.; Miri, M.-A.; Onishchukov, G.; Christodoulides, D. N.; Peschel, U. *Nature* **2012,** 488, (7410), 167-171.

247. Feng, L.; Xu, Y.-L.; Fegadolli, W. S.; Lu, M.-H.; Oliveira, J. E. B.; Almeida, V. R.; Chen, Y.-F.; Scherer, A. *Nat Mater* **2013,** 12, (2), 108-113.